NIOBIUM-COBALT CO-DOPED BARIUM TITANATE DIELECTRIC CERAMICS FOR MULTILAYERED CERAMIC CAPACITORS

A THESIS SUBMITTED TO
THE GRADUATE SCHOOL OF NATURAL AND APPLIED SCIENCES
OF
MIDDLE EAST TECHNICAL UNIVERSITY

BY

BERKAY ÖZGÜR

IN PARTIAL FULFILLMENT OF THE REQUIREMENTS
FOR
THE DEGREE OF MASTER OF SCIENCE
IN
METALLURGICAL AND MATERIALS ENGINEERING

AUGUST 2022

Approval of the thesis:

Niobium-Cobalt co-doped Barium Titanate Dielectric Ceramics for Multilayered Ceramic Capacitors

submitted by **BERKAY ÖZGÜR** in partial fulfillment of the requirements for the degree of **Master of Science** i**n Metallurgical and Materials Engineering, Middle East Technical University** by,

Prof. Dr. Halil Kalıpçılar
Dean, Graduate School of **Natural and Applied Sciences** _____

Prof. Dr. Ali Kalkanlı
Head of the Department, **Metallurgical and Materials Engineering** _____

Prof. Dr. Abdullah Öztürk
Supervisor, **Metallurgical and Materials Engineering, METU** _____

Examining Committee Members:

Prof. Dr. Cihangir Duran
Metallurgical and Materials Eng, Ankara Yıldırım Beyazıt Uni _____

Prof. Dr. Abdullah Öztürk
Metallurgical and Materials Eng., METU _____

Assoc. Prof. Dr. Volkan Kalem
Metallurgical and Materials Eng., Konya Teknik Uni _____

Assoc. Prof. Dr. Batur Ercan
Metallurgical and Materials Eng., METU _____

Assist. Prof. Dr. Yusuf Keleştemur
Metallurgical and Materials Eng., METU _____

Date: 22.08.2022

I hereby declare that all information in this document has been obtained and presented in accordance with academic rules and ethical conduct. I also declare that, as required by these rules and conduct, I have fully cited and referenced all material and results that are not original to this work.

Name Last name : Özgür, Berkay

Signature :

ABSTRACT

Niobium-Cobalt co-doped Barium Titanate Dielectric Ceramics for Multilayered Ceramic Capacitors

Özgür, Berkay
Master of Science, Metallurgical and Materials Engineering
Supervisor : Prof. Dr. Abdullah Öztürk

July 2022, 93 pages

Niobium (Nb) and Cobalt (Co) co-doped barium titanate ($BaTiO_3$) ceramics were prepared to stabilize ferroelectric-tetragonal phase transformation of $BaTiO_3$. Preparation of ceramics started with mixing $BaTiO_3$, Nb_2O_5 and Co_3O_4 powders at predetermined concentrations varying from 1 to 3 at%. The mixing was done at wet conditions using distilled water with alumina balls at 50 rpm for 24 h in a ball mill. Then, the mixtures were compacted into 15 mm diameter and 3 mm thick disc shaped pellets by uniaxial pressing at 200 MPa. After that the discs were sintered at various temperatures ranging from 1250 to 1290 °C for various durations ranging from 30 to 120 min. Sintered pieces were characterized using XRD, SEM, EDS, and DSC characterization techniques. Electrical properties namely dielectric constant (ε_r), dielectric loss (tanδ) and ε_r versus temperature were measured. Experimental results revealed that the co-doping of $BaTiO_3$ with Nb and Co lead to broadening of ε_r peaks and temperature stability. A high ε_r of 3258 at 1 kHz was obtained at room temperature, along with +10% and -17% variation over temperature ranging between -30 and +150 ºC. Also, the dramatic change in crystal structure of $BaTiO_3$ at 10 and 121 ºC was suppressed.

Keywords: Dielectric Constant, Capacitance, Barium Titanate, Dielectric loss, Doping

ÖZ

Çok Katmanlı Seramik Kapasitörler için Niyobyum-Kobalt co-doped Baryum Titanat Dielektrik Seramikleri

Özgür, Berkay
Yüksek Lisans, Metalurji ve Malzeme Mühendisliği
Tez Yöneticisi: Prof. Dr. Abdullah Öztürk

Ağustos 2022, 93 sayfa

Niyobyum (Nb) ve Kobalt (Co) katkılı baryum titanat ($BaTiO_3$) seramikleri, $BaTiO_3$'ün ferroelektrik-tetragonal faz dönüşümünü stabilize etmek için hazırlandı. $BaTiO_3$, Nb_2O_5 ve Co_3O_4 tozlarının önceden belirlenmiş konsantrasyonlarda 1 ila 3 atom yüzdesi arasında karıştırılmasıyla seramiklerin hazırlanmasına başlandı. Karıştırma, yitria ile stabilize edilmiş zirkonya ile damıtılmış su kullanılarak ıslak koşullarda bilyalı değirmende 24 saat boyunca 50 rpm'de yapıldı. Daha sonra karışımlar, 200 MPa'da tek eksenli presleme ile 15 mm çapında ve 3 mm kalınlığında disk şeklinde peletler halinde preslendi. Bundan sonra diskler 1250 °C ila 1290 °C arasında değişen sıcaklıklarda 30 dakika ila 2 saat arasında değişen çeşitli sürelerde sinterlendi. Sinterlenmiş parçalar XRD, SEM, EDS ve DSC karakterizasyon teknikleri kullanılarak karakterize edildi. Elektriksel özellikler, yani dielektrik sabiti (ε_r), dielektrik kaybı (tanδ) ve ε_r'nin sıcaklığa bağlı değişimi, empedans analiz yöntemi kullanılarak ölçüldü. Deneysel sonuçlar, $BaTiO_3$'ın Nb ve Co ile birlikte katkılanmasının, ε_r piklerini ve sıcaklık stabilitesini genişlettiğini ortaya koydu. Oda sıcaklığında 1 kHz'de 3258'lik bir ε_r elde edilirken, -30 ile +150 ºC arasında değişen sıcaklıklarda, ε_r'de +%10 ve -%17'lik bir değişim elde edildi. Ayrıca, $BaTiO_3$'ın 10 ve 121 ºC'deki kristal yapısındaki değişim bastırıldı.

Anahtar Kelimeler: Dielektrik Sabiti, Kapasitans, Baryum Titanat, Dielektrik Kayıp, Doping

To my family

ACKNOWLEDGMENTS

Thank you to my supervisor, Prof. Dr. Abdullah Öztürk, for your patience, guidance, and support. I have benefited greatly from your wealth of knowledge and meticulous editing. I am extremely grateful that you took me on as a student and continued to have faith in me over the years.

I would like to acknowledge Tübitak SAGE for their financial support. It has been an honor to be the part of such an organization that providing me complete academic freedom in this research.

Thank you to my committee members, Assoc. Prof. Dr. Volkan Kalem and Prof. Dr. Cihangir Duran. Your encouraging words and thoughtful, detailed feedback have been very important to me.

Thank you to of Dr. Necmettin Kaan Çalışkan, Dr. Mehmet Kaan Pehlivanoğlu, and MSc. Hakan Der for all the kind words and assistance you have provided.

Many thanks to all the members of staff in Fundamental Materials Technologies Division for their kind support during my MSc study. Also, I extend my thanks to all my colleagues at Tübitak SAGE for their continuous encouragement and support, as well as to all my friends at Middle East Technical University and outside for their time, advice, and moral support.

Thanks go to my parents, Suphi and Türkân Özgür, for your endless support. You have always stood behind me, and this was no exception. Mom, thank you for fielding a ridiculous number of phone calls, for calming me down, and for proofreading anytime, anywhere. Dad, thank you for all your love and for always reminding me of the end goal.

I am grateful for friends whose constant love and support keep me motivated and confident. My accomplishments and success are because they believed in me, keep me grounded, remind me of what is important in life, and are always supportive of my adventures.

TABLE OF CONTENTS

LIST OF TABLES

TABLES

LIST OF FIGURES

FIGURES

LIST OF ABBREVIATIONS

ABBREVIATIONS

Å	Angstrom
m	Meter
mm	Millimeter
nm	Nanometer
μm	Micrometer
kHz	Kilohertz
Hz	Hertz
MHz	Megahertz
GHz	Gigahertz
au/arb units	Arbitrary units
rpm	Revolutions per minute
ε_r	Relative Permittivity
DF	Dissipation Factor

CHAPTER 1

INTRODUCTION

Barium titanate ($BaTiO_3$) is one of first ferroelectric and piezoelectric ceramic developed for commercial piezoelectric applications such as sensors, and piezoelectric motors. It also plays a vital role in manufacture of multilayer ceramic capacitors (MLCC) since it has large (~7000) relative permittivity (i.e., dielectric constant, ε_r) at room temperature, though other ceramics have values between 20 and 70 [1]. $BaTiO_3$ ceramics are used as dielectric materials with high ε_r (3500) at 1 kHz, high thermal stability (± 15%) between -30 and +125 °C, and low dissipation factor (~3.5%) to use in high capacitance MLCC's [1], [2]. Also, $BaTiO_3$ have simple composition and structure, high stability, easy adaptations to different applications by doping and tailoring the microstructure, simple and cheap processing of ceramics, and lack of competitors in given applications [2].

Ceramic capacitors are divided into two classes according to the dielectric properties of the materials used [2]. Class 1 ceramic capacitors use paraelectric dielectric materials such as rutile phase TiO_2 with additives of Zn, Mg, Ca, or Ta, and provide minimum temperature dependence in ε_r. Class 2 ceramic capacitors use dielectric material with high ε_r but, it comes with a higher temperature dependence, lower accuracy, and stability. Class 2 ceramic capacitors are made of ferroelectric materials such as $BaTiO_3$ [2].

$BaTiO_3$ has perovskite structure with different crystallographic variants depending on the temperature as shown in Figure 1 [3]. As a result of allotropic transformations, $BaTiO_3$ exhibits different ε_r with respect to temperature. Especially, an abrupt increase in ε_r due to the high temperature transformation of paraelectric cubic structure to the ferroelectric tetragonal structure at the temperature ranging between ~100 and ~150 °C should be avoided.

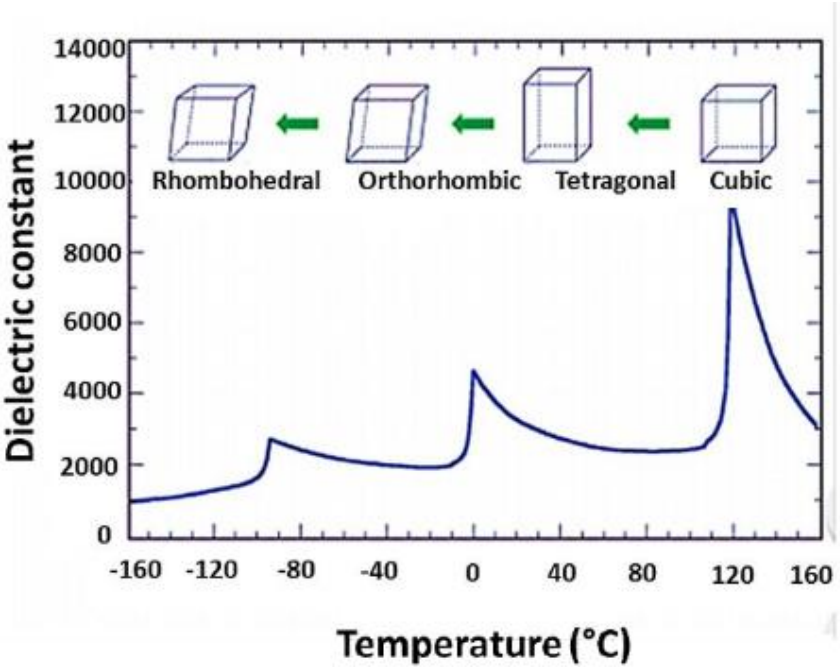

Figure 1. Temperature dependence of perovskite crystal structure of $BaTiO_3$ and variations in relative ε_r with temperature [4].

Dependence of ε_r to temperature in $BaTiO_3$ ceramics is one of the most unfavorable properties for capacitor applications. It has been experienced that doping a small amount of impurity elements into the structure of $BaTiO_3$ overcomes this deficiency. Doping of impurity elements results in the development of core-shell structure, controls grain growth, and hence improves electrical and/or optical properties [5]. Proper dopants are used to improve temperature stability, regulate sintering temperature, and increase lifetime of $BaTiO_3$ ceramics. Kishi et al. [5] reported that at least two dopants are needed to be able to overcome the temperature dependency of ε_r for $BaTiO_3$ and, to produce reliable capacitors with long lifetime. First dopant is an acceptor such as Mn^{2+}, Mg^{2+}, Ca^{2+}, and Co^{2+} to substitute Ti site to prevent degradation of $BaTiO_3$ during sintering [6]. Second dopant could be the ions with intermediate ionic radius such as Y^{3+}, Ho^{3+}, Nb^{5+} which substitute both Ba and Ti site to obtain shell region [5]. Burn [7] reported that Nb addition broadens ε_r peaks of $BaTiO_3$. Also, Co addition is necessary to decrease temperature dependence of relative ε_r. Chazano and Kishi [8] highlight the importance of firing temperature and composition on temperature dependence of ε_r. Chen et al. [9] stated the importance

of Nb/Co ratio for controlling grain growth and providing effective core-shell structure to gain optimal dielectric properties in the temperature ranging from -50 to +125 °C. It has been reported that core-shell structure in $BaTiO_3$ is favored by slow volume diffusion of Nb [10].

Doping of impurity elements into the structure of $BaTiO_3$ could be accomplished by the methods including conventional mixed-oxide [11], sol-gel [12], [13] and hydrothermal synthesis [12], [14]. Among these methods, conventional mixed oxide is the most commonly used one since it has the advantages of low processing temperature, good homogeneity, suitability to mass production, and low cost [15].

Dielectric properties of ceramics could be determined by the techniques such as open-ended coaxial-line probes [16], network analyzers [17], and computer controlled impedance analyzers (LCR Meter) [18]. Among these methods, impedance analyzer method is used in this study since it has the advantages of high accuracy, easy sample preparation, and setup.

Differential scanning calorimetry (DSC) is a thermoanalytical technique that could be employed to detect phase transitions in materials with respect to temperature. Since the main reason of ε_r change of $BaTiO_3$ based ceramics is the allotropic changes at certain temperatures, i.e., ~5 and ~120 °C, DSC could be employed to detect the allotropic changes with respect to temperature variations [19]. Although, as a result of the dielectric properties, are predicted. Although DSC curves of $BaTiO_3$ are available [20], [21], the DSC data on the Nb-Co co-doped $BaTiO_3$ ceramics has not been presented in the open literature yet.

The purposes of the present study are to prepare Nb and Co co-doped $BaTiO_3$ ceramics with controlled microstructure by conventional mixed-oxide route, and to suppress the phase transformations taking place at temperatures between -30 and +125 °C so that dielectric properties of $BaTiO_3$ ceramics are improved. Structural analyses by XRD, SEM and EDS provide an insight on the compositional dependency of the phases developed during processing, and hence on the dielectric properties. DSC measurements are carried out to observe the relationship between ε_r and crystal structure variations with respect to temperature.

CHAPTER 2

LITERATURE REVIEW

2.1 Dielectric Phenomenon

A dielectric material is an electrically insulating (nonmetallic) material which exhibits or may be made to exhibit an electric dipole structure [22]. In this type of materials, there is a separation of positive and negative electrically charged entities on a molecular or atomic level. As a result of dipole interactions with electric fields (ξ), dielectric materials are frequently used in design and fabrication of capacitors. ε_r is the ratio of permittivity of a dielectric medium (ε) to the permittivity of vacuum (ε_0 = 8.854 x 10^{-12} F/m) as formulated in Eq 1 [23]. ε_r is one of the primary considerations for capacitor design.

$$\varepsilon_r = \frac{\varepsilon}{\varepsilon_0} \qquad \text{Eq. 1.}$$

Capacitance phenomenon could be described with the help of field vectors. An electric dipole moment between separated charges could be described as:

$$p = qd \qquad \text{Eq. 2.}$$

Where: p = polarization vector
q = electric charge magnitude
d = distance

Schematic of electric dipole generated by two electric charges is shown in Figure 2. After ξ is applied, force appeared on the poles orients them according to the direction of the ξ, as displayed in Figure 2 [24].

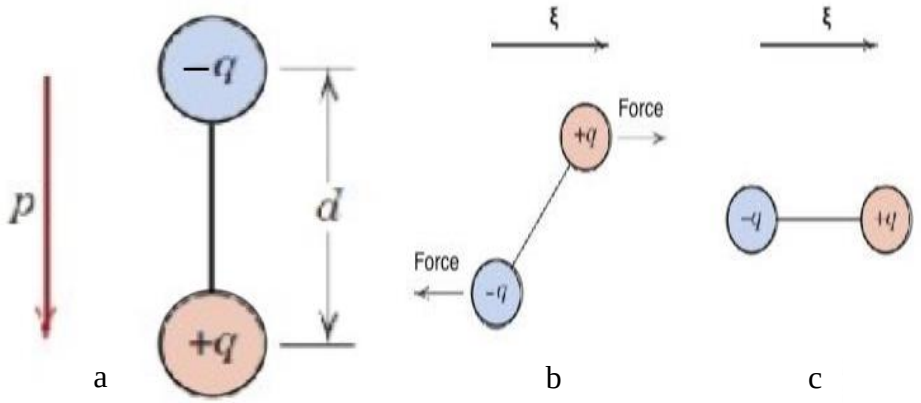

Figure 2. (a) Schematic illustration of the electric dipole. (b) Imposed forces on a dipole. (c) Final dipole with field [24].

Polarization is defined as the alignment of dipoles to the direction of applied ξ. There are three types of polarization: electronic, ionic, and orientation polarization [25]. Electronic polarization is the result of position shift of positive nucleus relative to electron cloud that surrounds the nucleus by applied ξ. Electronic polarization is the main working principle of dielectric materials and only exists when an ξ is present. It is schematically shown in Figure 3a.

Ionic polarization exists in ionic materials. Applied ξ attracts cations and anions to the opposite directions, this results in increased net dipole moment. It is schematically shown in Figure 3b.

Orientation polarization only exists in materials that have permanent dipole moments [25]. Polarization happens by applying ξ to align the permanent dipoles in same direction with applied field. This polarization is hindered by thermal vibrations, i.e., increasing temperature decreases the polarization. It is schematically shown in Figure 3c.

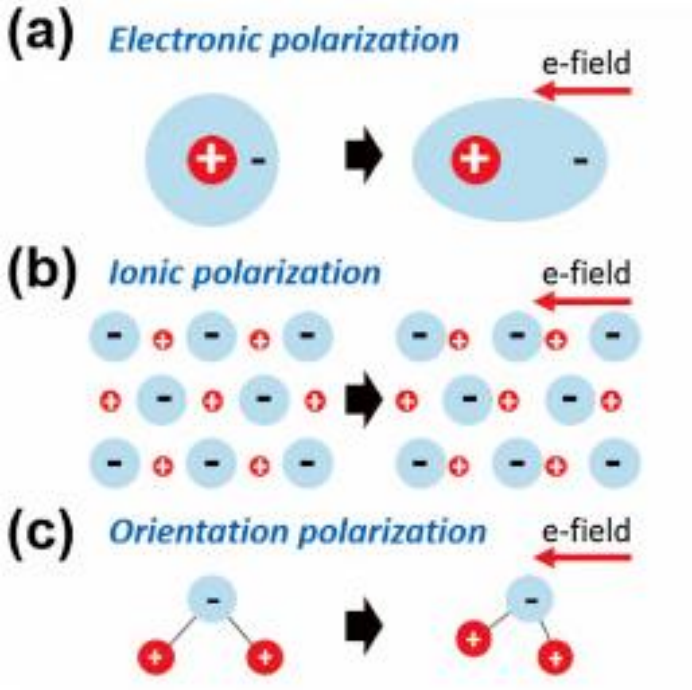

Figure 3. Schematic of (a) electronic, (b) ionic and (c) orientation polarization [24].

Total polarization of a sample is:

$$p = p_e + p_i + p_o \qquad \text{Eq. 3.}$$

Where: p_e is the electronic polarization.
P_i is the ionic polarization
P_o is the orientation polarization

It is possible that one or more of these polarizations are relatively very small against other types of polarization. For example, if a sample does not have permanent dipole moments, orientation polarization value is negligible in magnitude against electronic or ionic polarization [24].

Nowadays, in most of the electronic applications alternative current (AC) is used. When an AC is applied, voltage or ξ changes with time in the same direction. If a material polarized by an electronic polarization, every time the ξ changes its

direction, dipoles try to rearrange with applied field [26]. Rearrangement requires some time. Each polarization type has different minimum rearrangement time. Relaxation frequency is the reciprocal of this minimum rearrangement time.

A dipole cannot keep shifting its orientation direction when the frequency of applied ξ exceeds its relaxation frequency. Therefore, orientation polarization does not contribute to ε_r at high frequencies. Dependence of ε_r to the contributions of different types of polarizations with frequency is shown in Figure 4. Because of these variations, every sample should be tested at its operating temperature and frequency [24].

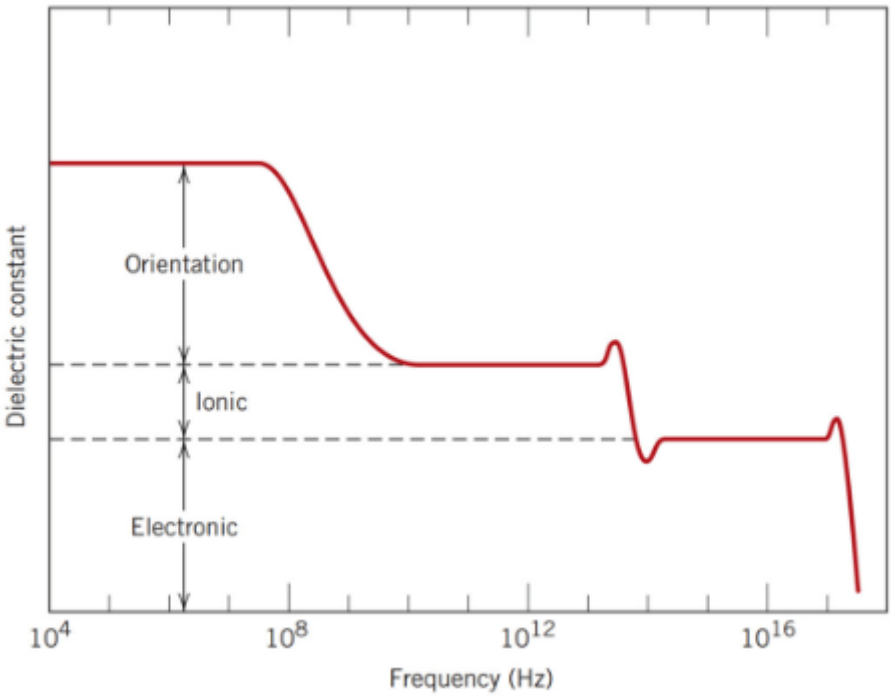

Figure 4. Variation of ε_r with frequency. Contributions of polarization types to ε_r [24].

Dielectric loss is the absorption of electrical energy by a dielectric material subjected to an alternating ξ. A low dielectric loss is desired at the application frequency. It also indicates the efficiency of the material used in a given application [27]. Dissipation factor (DF or tanδ) is the electrical property of an electrically insulating

material. It is the electrical energy absorbed and lost (power dissipation) when electrical current is applied to an insulating material. Most of the absorbed energy is dissipated as heat. DF indicates the inefficiency of material to hold energy or behave as an insulating material. The lower the DF, the more efficient is the insulator system. DF is a dimensionless measure, and hence no units. The low DF indicated high-quality, high performance electrical or electronic systems. It is important for insulator materials in high-frequency applications such as radar equipment or microwave parts. Low values mean better dielectric materials with less dielectric heating.

2.2 Capacitors

A capacitor is an electronic component that can be charged to store electrical energy. The main reason behind the research and development of capacitors are consumer electronics market including computers, mobile phones, TV's, etc. But since defense and aerospace industry contains so many electronical components, the capacitors also become widely used in such areas [28].

Capacitance (C) is the amount of electrical charge that can be stored in a capacitor. C of a capacitor consisting of two parallel plate electrodes with an overlapping surface area (A) separated by dielectric layer of thickness (t), could be calculated as:

$$C = \frac{\varepsilon_r \varepsilon_0 A}{t} \qquad \text{Eq. 4.}$$

Where: ε_r = relative permittivity of dielectric layer

ε_0 = permittivity of free space = 8.854 x 10^{-14} F cm^{-1}

Charge in a capacitor could be calculated as:

$$Q = CV \qquad \text{Eq. 5.}$$

Where: Q = Charge (in Coulombs)

V = Potential difference between the plates in Volts.

In order to increase the capacity of a capacitor, a big A, a thin dielectric t and, a high ε_r of dielectric layer is preferred [29].

Capacitors are classified into the three categories [30].

1. Electrostatic capacitors
2. Electrolytic capacitors
3. Electrochemical capacitors.

Electrostatic capacitors are the base for this thesis work. Electrostatic capacitors typically consist of two metal electrodes which are parallel, separated by a dielectric layer as shown in Figure 5.

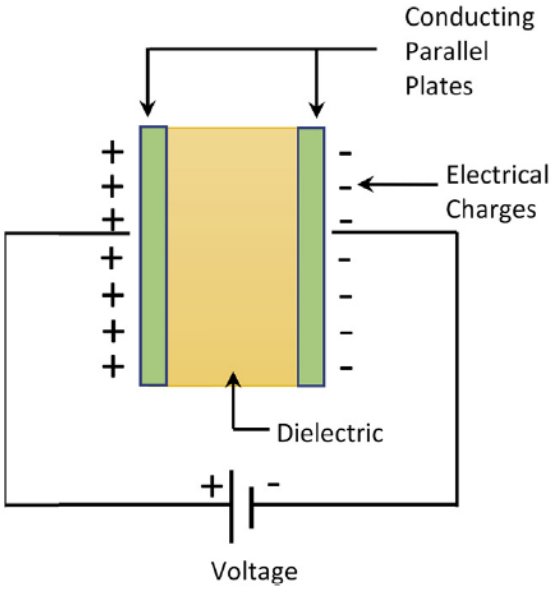

Figure 5. Schematic for an electrostatic capacitor [30].

The ideal dielectric material to be used in a capacitor should have high ε_r, low dielectric loss, and high dielectric strength (breakdown voltage). ε_r values of various dielectric materials are given in Table 1 [30].

Ceramics, films, and papers are some of the commercially available electrostatic capacitors. Charge capacity of a capacitor depends on the material used for manufacturing and its ε_r. For high C power-based charge delivery applications, generally ceramic based capacitors are used, and these applications are generally operated at low frequencies such as 1-10 kHz. The ε_r values specified in Table 1 are based on 1 kHz. Therefore, 1 kHz frequency was taken for the dielectric measurements in the present study.

Ceramic capacitors make use of a ceramic as the dielectric material. There are two types of ceramic capacitors widely used in modern electronics which are: MLCC and ceramic disc, as shown in Figure 6 [31]. MLCCs are considerably smaller than disc capacitor. As a result, they could be used at surface mount devices in electronical circuits [32].

Table 1. ε_r values for various dielectric materials [30].

Material	**ε_r (at 1 kHz)**
Vacuum	1
Air	1.0006
Polypropylene	2.2
Polyphenylene sulfide	3
Polyester	3.3
Mica	6.8
Aluminum oxide	9.7
Tantalum oxide	27.7
Paraelectric ceramics	5-90
$BaTiO_3$	3000-8000

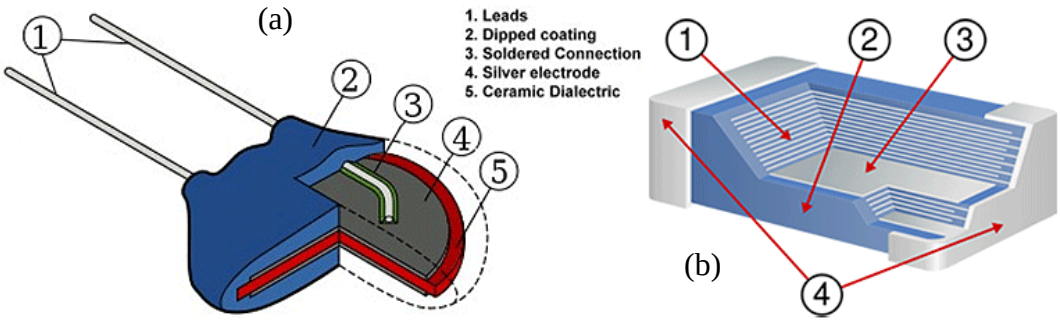

Figure 6. Schematic of (a) ceramic disc capacitor and (b) MLCC [33].

Ceramic capacitors are classified into two types in terms of the ceramic dielectric used: class 1 and class 2 [2]. Class 1 ceramic capacitors use paraelectric dielectric materials such as rutile phase TiO_2 with additives of Zn, Mg, Ca, or Ta, and provide minimum temperature dependence in ε_r. Because of relatively low ε_r, C value of class 1 capacitor is low. Class 1 capacitors mostly used in low loss applications such as filters and oscillators that their C varies very little over temperature. NP0 and C0G capacitors have very common class 1 temperature coefficients and have a temperature coefficient of 0 and tolerance of +/-30 ppm.

Class 2 ceramic capacitors use dielectric material with high ε_r, but it comes with a higher temperature dependence, lower accuracy, and stability [2]. They are made of ferroelectric materials such as $BaTiO_3$. They are used in high charge density applications as well as coupling and decoupling applications in which the exact value of C is not critical. X7R capacitor is a very common class 2 temperature coefficient, and X7R capacitors typically have tolerance of 5%, 10%, and 20%. Naming of class 2 capacitors are given in Table 2. It consists of X, Y, and Z as low temperature letter code, 4, 5, 6, 7, 8, and 9 as upper temperature number code, and P, R, S, T, U, and V as letter code of C change over the temperature range. Examples of capacitor types are given in Table 3. NP0 is a class 1 capacitor and X7R and Y5V is a class 2 capacitor. C change and DF is very low for class 1 capacitor and higher for class 2 capacitors as mentioned earlier.

Table 2. Naming of class 2 capacitors.

Letter code low temperature (°C)	**Number code upper temperature (°C)**	**Letter code of capacitance change over the temperature range (%)**
X = -55	4 = +65	P = ± 10
Y = -30	5 = +85	R = ± 15
Z = +10	6 = +105	S = ± 22
	7 = +125	T = + 22 / -33
	8 = +150	U = + 22 / -56
	9 = +200	V = + 22 / -82

Table 3. Examples of class 1 and 2 capacitors and required dissipation factor.

Material	**ε_r**	**C change (%)**	**DF (%)**
NP0	15-100	<0.4 (-55 to 125 °C)	0.1
X7R	2000-4000	+/-15 (-55 to 125 °C)	3.5
Y5V	>16000	Up to 82 (-30 to 85 °C)	9

2.3 $BaTiO_3$ Based Dielectric Ceramics

$BaTiO_3$ is the first ferroelectric and piezoelectric ceramic developed for commercial applications [1]. It is used as high $\boldsymbol{\varepsilon_r}$ dielectric in MLCC and as a semiconducting material in thermistors with positive temperature coefficient of resistivity (PTCR). Utilization of $BaTiO_3$ ceramic in dielectric applications started after realization of its high ε_r. The cause of high ε_r is the ferroelectricity. Additionally, $BaTiO_3$ has high chemical stability and wide operation temperature range [34]. After more than 75 years of investigation, $BaTiO_3$ ceramic has been used in capacitors, lead-free piezoelectric devices, ceramics, and composites for energy storage. Main reason of the success is simple composition and structure, high stability, and ease to adapt the properties to the specific application by doping, formation of solid solutions with

other perovskites and tailoring of microstructure. Relatively simple and cheap processing especially in the case of ceramics, and lack of effective competitors in core applications are among the advantages [35].

The crystal structure of $BaTiO_3$ and the origin of ferroelectricity in this compound based on the cooperative ordering of the electrical dipoles arising from the deformation of the prototype perovskite cubic cell was well established by Rooksby [36], Megaw [37], and Kay and Vousden [38]. The BaO-TiO_2 phase diagram shown in Figure 7 presents at least 9 ternary compounds which have been proven to be useful as electro ceramics, with the most important being the perovskite $BaTiO_3$ for its application in MLCCs and PTCR devices [39].

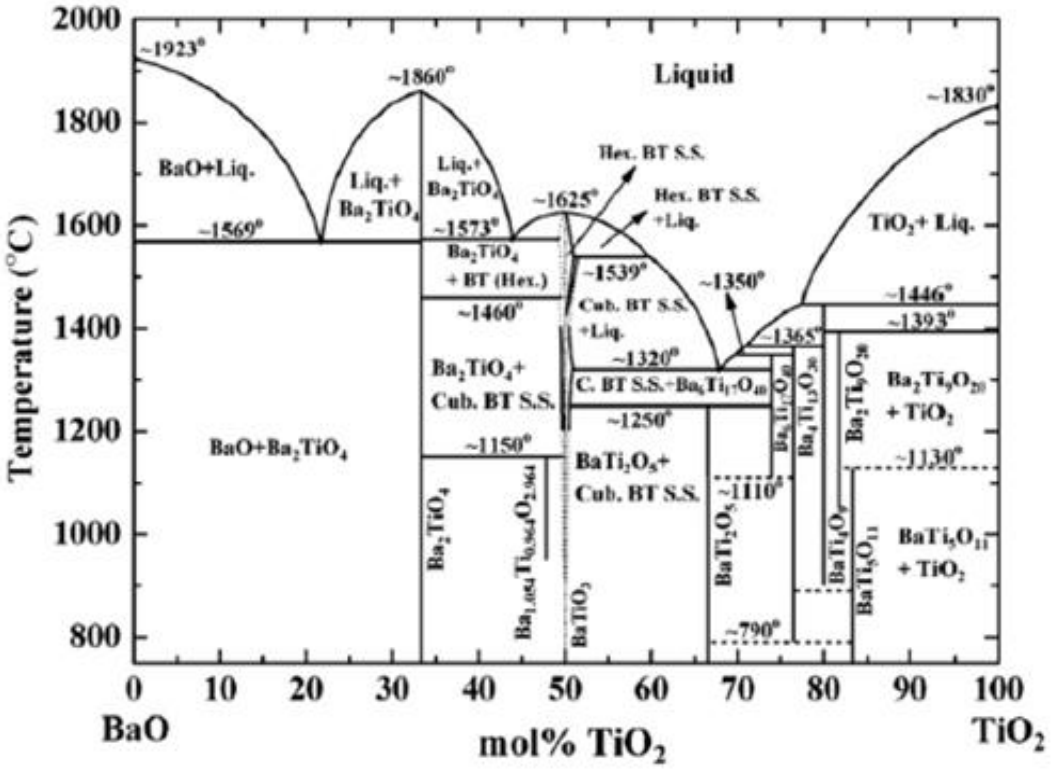

Figure 7. BaO-TiO_2 phase diagram [39].

The perovskite form of $BaTiO_3$ exhibits different crystallographic variants, depending on temperature, as shown in Figure 8 [40]. The high temperature cubic form has the prototype ABO_3 (with Ba^{+2} as A and Ti^{+4} as B) perovskite structure. This is a centrosymmetric structure with Ba^{+2} at the corners, Ti^{+4} at the center, and the oxygen at the face centers. The Ti ion is octahedrally coordinated by six oxygen ions while Ba^{+2} has a dodecahedral coordination. As seen in Figure 8, at the Curie temperature, T_C = 110–130 °C, it transforms from the high temperature paraelectric cubic form (C, Pm3m) to the ferroelectric tetragonal structure (T, P4mm). On further cooling, another ferroelectric phase is observed which is orthorhombic (O, Amm2), below 5–15 °C.

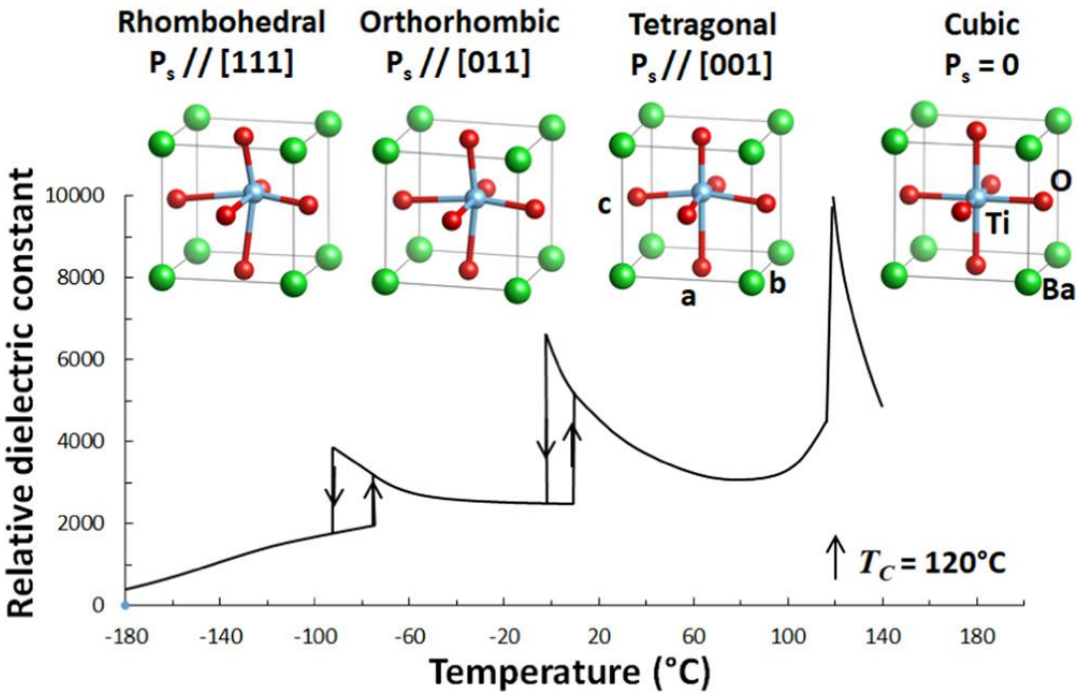

Figure 8. Temperature dependence of $BaTiO_3$ crystal structure [40].

The structural changes directly affect the relative ε_r of the sample and C of whole structure. Thus, to prepare temperature independent powders for capacitor fabrication, the slope, and positions (temperature) of the peaks should be modified for suitable applications.

Chemical modification is the most common and simple approach for tuning these phase transitions and properties of $BaTiO_3$. The term doping is used to indicate the substitution of a limited amount of parent ions. Even at very small amounts, like few mole%, doping can change the functional properties of $BaTiO_3$, like electrical conductivity and ε_r. [41]. To change the phase transition temperature and especially to shift the Curie temperature to room temperature the chemical modification is a must. The formation of solid solutions creates local compositional fluctuations. With coexistence of polymorphs and diffuse phase transitions over a relatively high-temperature range result in broad ε_r peaks. Doping is also essential to modify some characteristics essential for its processing and reliability under operating conditions such as resistance to degradation of dielectric properties during sintering, high insulation resistance, and resistance to aging. [42]. The modification of chemical structure has huge effect on final properties by defect chemistry, shift and modification of phase transitions, and changes in crystal structure.

Dielectric properties can also be controlled by modifying microstructure and grain size. It is a general knowledge that the ε_r activity of $BaTiO_3$ is maximized for a grain size of ~1 μm. It is also known that producing the ceramics with core-shell grains could improve ε_r and temperature stability of ceramic capacitors. The method of producing core-shell grains combines the chemical modification of $BaTiO_3$ with the control of microstructure and formation of compositional gradients [40].

The preferred microstructure for temperature-stable dielectrics consists of $BaTiO_3$ core surrounded by a shell of more heavily doped material. This microstructure broadens the ε_r peaks around room temperature [43].

The core-shell microstructure can be obtained by controlling the Ba/Ti ratio, the amount of an appropriate dopant oxide, and grain growth [19], [43]. Kishi et al. [5] and Sato et al. [6] reported that to obtain reliable capacitors with improved lifetime, that uses base metal electrode technology, at least two dopants are needed. First dopant is an acceptor (Mn, Mg, Ca etc.) which substitutes at the Ti site that avoids degradation of dielectric properties of $BaTiO_3$. The second dopant is generally a rare-earth ion with intermediate ionic radius such as (Y, Ho, Dy) which substitutes both

Ti and Ba site to produce shell region. Microstructure control plays a crucial role on the performance of the capacitors and needs the optimization of several parameters. Mizuno et al. [42] reports that only 10-20 °C variation of sintering temperature can change the microstructure, thus dielectric properties significantly since it could change the shell and core structure.

Currently, the $BaTiO_3$-Nb_2O_5-Co_3O_4 system is well known for a high ε_r and temperature-stable ceramics to be used for MLCCs with Pd or Ag/Pd internal electrode. Hennings and Schreinemacher [19], reported that the Nb/Co ratio had great influence on the grain growth and electric properties in the system $BaTiO_3$–Nb_2O_5–Co_3O_4. Similarly, the investigation of materials with various Nb/Co ratios in the $BaTiO_3$–Nb_2O_5–Co_3O_4 ternary system, especially the Nb-rich composition (Nb/Co = 3.00), and the Co-rich composition (Nb/Co = 1.67) with the same Nb + Co amount of 2 at%, has revealed a large influence of the Nb/Co ratio on the electric properties, densification behavior, and microstructural evolution. Usually a sintering aid, powdered glass or silica, is added to lower the sintering temperature. It has been stated that [10], [44–46] the formation of the shell does not occur by solid-state diffusion of the dopant. It happens by a dissolution-precipitation process of a liquid phase in which dopants dissolve.

The preparation of samples starts with mixing $BaTiO_3$, Nb_2O_5, and Co_3O_4 powders at various concentrations. They are blended by wet ball milling, then uniaxially pressed into pellets in a hydraulic press. After that, the discs are sintered at different temperatures. Finally, ceramics are characterized, and their ε_r is measured.

Burn [7] stated that the Nb_2O_5 addition to $BaTiO_3$ can broaden the ε_r peaks as shown in Figure 9 since the C change directly related to the ε_r of the sample. Lower mole percent (2.1 mole%) Nb_2O_5 content provides lower C change throughout the temperature range. He also stated that the Co_3O_4 addition is necessary to obtain temperature stability as shown in Figure 10. Higher Co content (i.e. 0.9 mole%) provides lesser C change throughout the temperature range which means, lesser ε_r change and lower temperature dependency.

Chen et al. [9] indicated that the Nb/Co ratio is very important for gaining optimal dielectric properties, as shown in Figure 11. Lower Nb/Co ratio provides higher ε_r but, the ε_r change throughout the temperature range is higher.

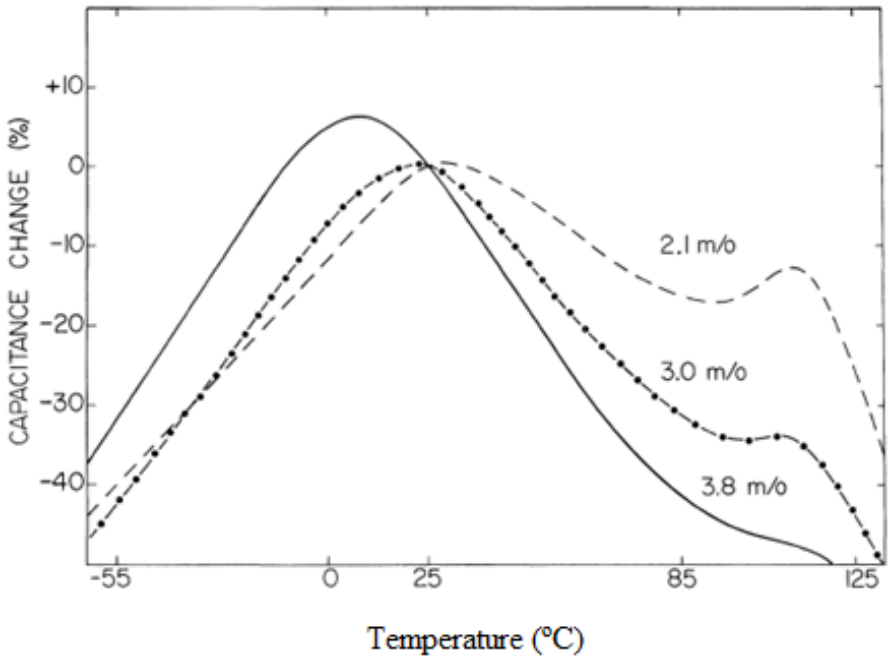

Figure 9. Addition of Nb_2O_5 to $BaTiO_3$ and its effect on capacitance [7].

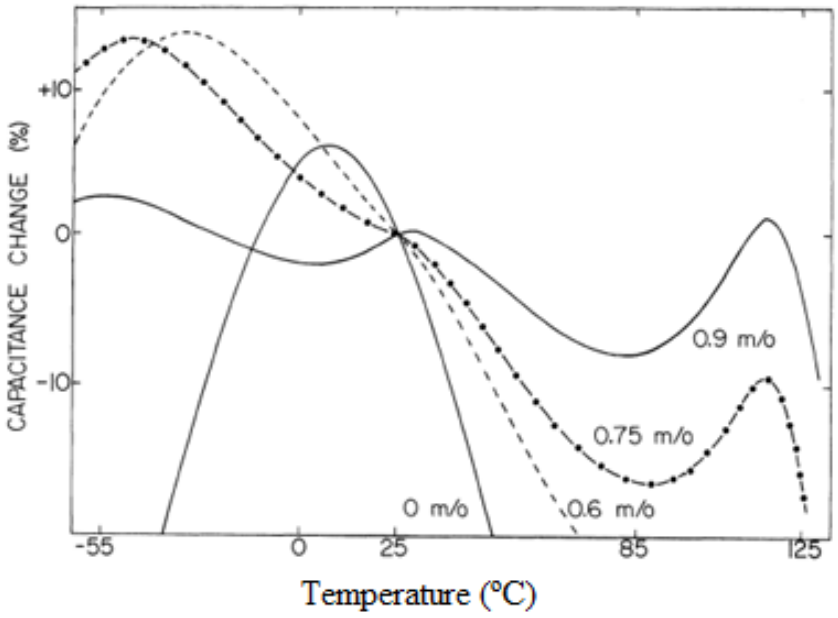

Figure 10. Addition of Co_3O_4 to 3.6 mole% Nb_2O_5 added $BaTiO_3$ and its effect on capacitance [7].

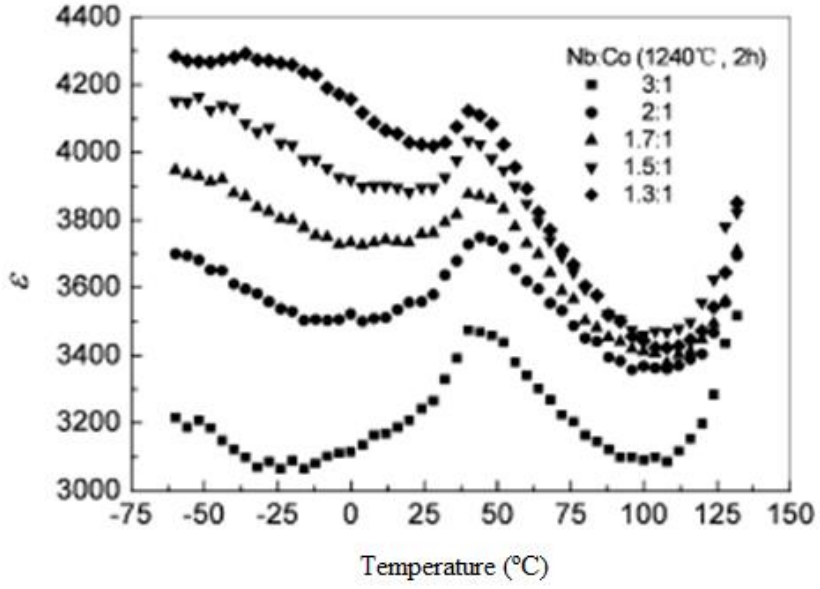

Figure 11. Effect of Nb/Co on dielectric properties and temperature stability [9].

Chazono and Kishi [8] showed in Figure 12 that the firing temperature and composition have significant effect on temperature dependence of ε_r. Higher Nb content leads to lower temperature dependency of ε_r. Higher Co content broadens the sharp $BaTiO_3$ peaks, but the temperature stability of the structure is lower than the composition having higher Nb content. Also, higher sintering temperature for both compositions provides higher ε_r. It could be concluded that the higher sintering temperature and higher Nb content in $BaTiO_3$ structure provides better dielectric properties.

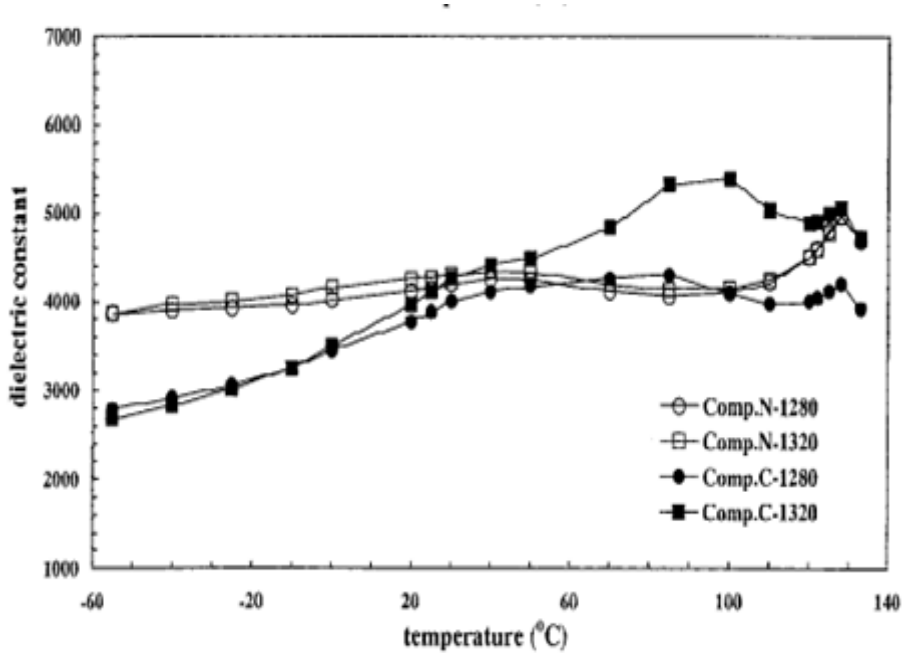

Figure 12. Effect of composition and sintering temperature on ε_r [8]. (Comp N means higher Nb content while Comp C means higher Co content.)

Hennings and Schreinemacher [19] stated that the core-shell structures in $BaTiO_3$ was favored by slow volume diffusion of Nb that provides temperature stability. Nb donors and Co acceptors on Ti sites forms the complex NbCo structure. Core-shell structure obtained by co-doping of Nb and Co is shown in Figure 13. The core consists of slightly doped $BaTiO_3$ by Nb atoms, while the shell region is doped heavily by both Nb and Co atoms.

Figure 14 shows the crystal structure of $BaTiO_3$; it has tetragonal crystal system with perovskite three-dimensional structure. Ba^{2+} bonded to twelve O^{2-} atoms. There are two inequivalent O^{2-} sites. In the first O^{2-} site, O^{2-} is bonded in a 2-coordinate geometry to four equivalent Ba^{2+} and two equivalent Ti^{4+} atoms. In the second O^{2-} site, O^{2-} is bonded in a 1-coordinate geometry to four equivalent Ba^{2+} and two equivalent Ti^{4+} atoms according to topological material database [47].

The fractional coordinates of Ba and O atoms in the $BaTiO_3$ structure are shown in Table 4.

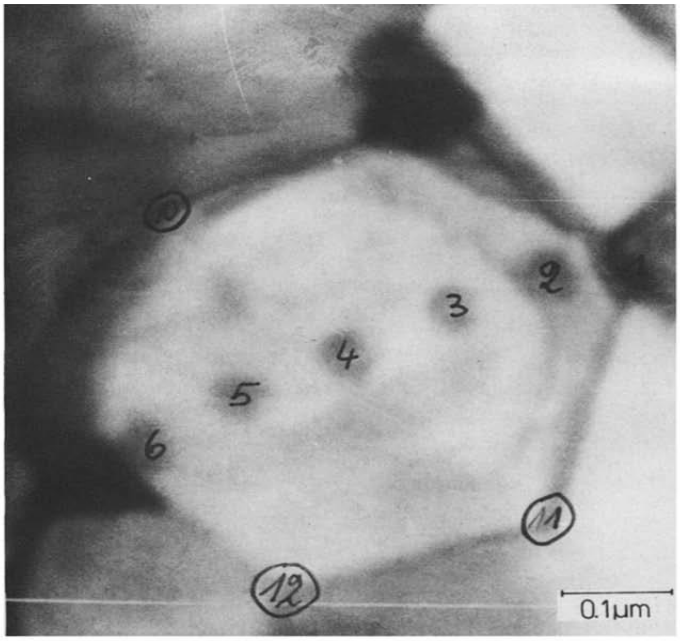

(a)

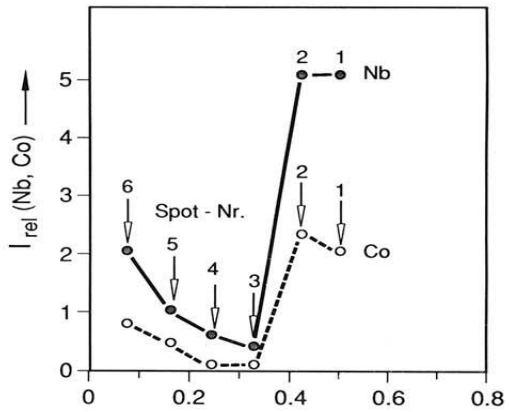

Figure 13. Core-shell structure obtained in Ba-Nb-Co ternary system [19].

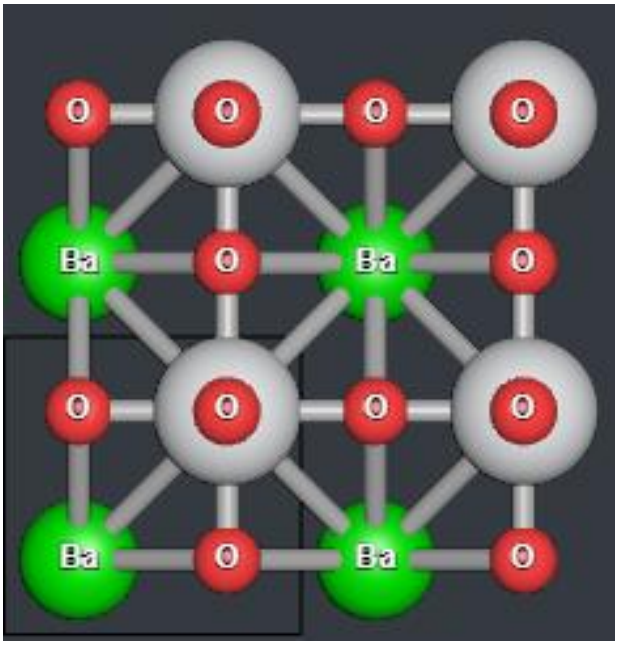

Figure 14. Crystal structure of $BaTiO_3$. The black square at bottom left shows the unit cell [47].

Table 4. Fractional coordinates of the elements in the $BaTiO_3$ structure [47].

Atom/Coordinates	**a**	**b**	**c**
Ba	0	0.5	0.0041
Ti	0	0	0.5243
O1	0	0.5	0.4793
O2	0	0	0.9589
O3	0.5	0	0.4793

*Numbers next to oxygen refers to the rank of that element relative to origin point.

The crystal structure of Co_3O_4 is shown in Figure 15. There are two inequivalent $Co^{2.67+}$ sites. $Co^{2.67+}$ is bonded to six equivalent O^{2-} atoms to form CoO_6 octahedra that share corners with six equivalent CoO_4 tetrahedra and edges with six equivalent CoO_6 octahedra according to topological materials database [40]. The fractional coordinates of Co_3O_4 are shown in Table 5.

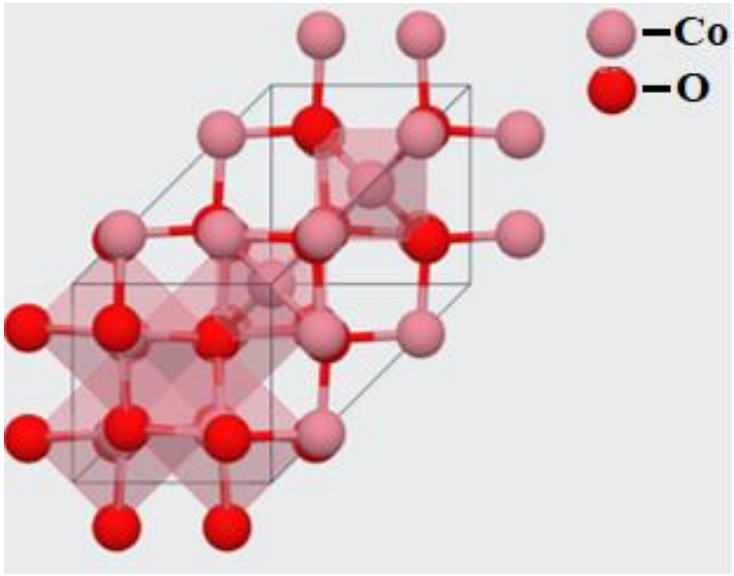

Figure 15. Crystal structure of Co_3O_4 [47].

Table 5. The fractional coordinates of the elements in the Co_3O_4 structure [47].

Atom/Coordinates	**a**	**b**	**c**
Co1	0.0009	0.9991	0.0009
Co2	0.1287	0.6233	0.6247
Co3	0.2508	0.2492	0.2508
Co4	0.6247	0.6233	0.1287
Co5	0.6268	0.1213	0.6268
Co6	0.6268	0.6251	0.6268
O1	0.3822	0.3862	0.8455
O2	0.3843	0.8463	0.3843
O3	0.3843	0.3852	0.3843
O4	0.4036	0.8659	0.8646
O5	0.8454	0.3862	0.3821
O6	0.8636	0.4046	0.8636
O7	0.8636	0.8682	0.8636
O8	0.8645	0.866	0.4036

*Numbers next to elements refers to the rank of that element relative to origin point.

Figure 16 shows the crystal structure of Nb_2O_5. There are fifteen inequivalent Nb^{5+} sites. Since there are too many inequivalent sites the structure is very hard to define, and the fractional coordinates are too complex to handle [3].

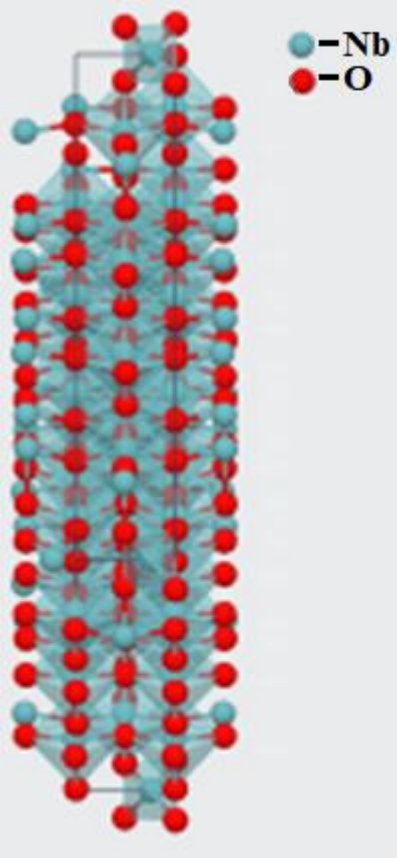

Figure 16. Crystal structure of Nb_2O_5 [47].

2.4 Conventional Mixed Oxide Method

The production procedure of the components produced by the conventional mixed oxide method consists of three main steps. In the first step, oxide powders are weighed to predetermined amount and mixed with a binder. Mixing is crucial for applications because the errors in mixing cannot be fixed by the following processes. The inhomogeneities in a mixture are in two different forms, (1) binder-powder

separation, and (2) segregation of particle size with binder. Mixing should provide coating of the particles with binder, disperse agglomerates, and obtain uniform distribution of binder and particle size [48].

After mixing, the powder with binder, is compacted by a suitable compaction technique, usually pressing. In order to achieve high density in the compacted piece, green body, external application of pressure is required. As pressure is applied, initial rearrangement of particles takes place with large pore filling. Higher pressures increase density by the fracture and fragmentation of the particles. Small and irregular particles hinder compaction because of higher inter particle friction [48].

Conventional compaction is followed by sintering. In this step, the compact is heated to high temperature to get a chemical bond between the particles. The driving force for sintering is the reduction of surface energy. Higher surface area particles such as small and spherical ones sinter faster than lower surface area particles such as coarse and irregular ones. Sintering is a thermally activated process which occurs by atomic transport through diffusion [15].

2.5 Differential Scanning Calorimeter (DSC)

DSC is applied to determine alterations in structural properties of a material as a function of time and temperature [49], [50]. Heat quantity is measured by the instrument as the temperature changes [51]. Two types of DSCs are used based on the mechanism of operation: heat-flux DSC and power compensated DSC [52], [53]. Typical scan rates are between 1 and 10 °C/min. For the purpose of peak resolution and sample investigation close to equilibrium, low scan rates are preferred, while sensitivity of measurement is enhanced at high scan rates as it leads to heat exchange within short period of time [54].

2.6 Parallel Plate Method

The parallel plate capacitor method is involving sandwiching of a dielectric material (thin sheet sample) between two electrodes to form a capacitor. Measurements can be taken using LCR meter or impedance analyzer and a dielectric fixture. In this method typically low frequencies (< 1 GHz) are used. Parallel plate test parameters are derived by considering the dimensions of the material and by measuring its C and DF. C value of the dielectric sample, measured via the above mentioned equipment, is used to calculate the ε_r of the material. Parallel plate method has high measurement accuracy (about ±1% for ε_r and 5% ±0.005 for tanδ) and involves very simple sample preparation and setup. Typically, frequency range from 20 Hz to 1 GHz is used for this purpose [55].

CHAPTER 3

EXPERIMENTAL PROCEDURE

In this chapter, the preperation procedure for pristine $BaTiO_3$ and Nb_2O_5 and/or Co_3O_4 single and co-added $BaTiO_3$ ceramics as well as the characterization and measurement procedures for the properties hve been outlined.

3.1 Ceramic Preparation

Ceramic capacitor samples were prepared by the solid state reaction method using high purity oxide powders. Three different powders used in this study were; Barium titanate ($BaTiO_3$; >99.5%, Entekno), Niobium Oxide (Nb_2O_5; 99.99%, Sigma-Aldrich), and Cobalt Oxide (Co_3O_4; (99.5%, Sigma-Aldrich). The $BaTiO_3$ ceramic was prepared as a reference material. In order to see the effects of Niobium (Nb) and/or Cobalt (Co) single or co-doping on dielectric properties of BTO, required amounts of Nb_2O_5 and/or Co_3O_4 were added to $BaTiO_3$ powder. 3 atomic percentages (at%) Nb and/or 3 at% Co were intended to dope $BaTiO_3$ structure. The label name of the samples produced, and their composition are given in Table 6. Hereafter, the single and co-doped $BaTiO_3$ ceramics will be called according to the names given in Table 6.

First, the starting powders were weighed using OHAUS pionner precision balance with high accurracy (±0.0001) to yield a ceramic with predetermined composition. Then, the powders were mixed in a ball mill using distilled water and yttria stabilized zirconia (YSZ) balls for 24 h. The mixture contained 100 g of powders, 100 g of distilled water and, 20 pieces of YSZ balls of 8 mm in diameter. Powder mixture was dried and screened with mesh number of 2000 to get rid of the agglomerates as much as possible.

Table 6. Names and compositions of the Nb_2O_5 and/or Co_3O_4 single and co-added $BaTiO_3$ ceramics.

Name	**$BaTiO_3$ (mole%)**	**Nb_2O_5 addition (mole%)**	**Co_3O_4 addition (mole%)**
$BaTiO_3$	100	-	-
Nb3	98.5	1.5	-
Co3	99	-	1
Nb1Co1	98.75	0.75	0.5
Nb3Co1	98.625	1.125	0.25

A polyvinyl alcohol (PVA) solution was prepared using a temperature controlled magnetic stirrer. 95 g distilled water and 5 g PVA were mixed in a beaker using a magnetic stirrer at 80 °C at 200 rpm for 4 h. Then, 2 g of 5% PVA solution was added to 100 g of the screened powder mixture and mixed in an agate mortar with pastle. Powder mixtures were compacted by uniaxial pressing in a hardened steel die. Pressing was carried out by aplying 200 MPa of uniaxial pressure for 10 s. The nominal dimensions of the disk shaped green pellets were 15 mm and 3 mm in diameter and height, respectively. Sintering was done in an electrically heated furnace at temperatures of 1250, 1270, and 1290 °C for 30, 60, and 120 min in air. Heating and cooling rates were 4 °C/min. Time vs temperature graph of heat treatment applied for the production of $BaTiO_3$ based ceramic capacitors is shown in Figure 17. A photograph of a representative sintered pellet is shown in Figure 18.

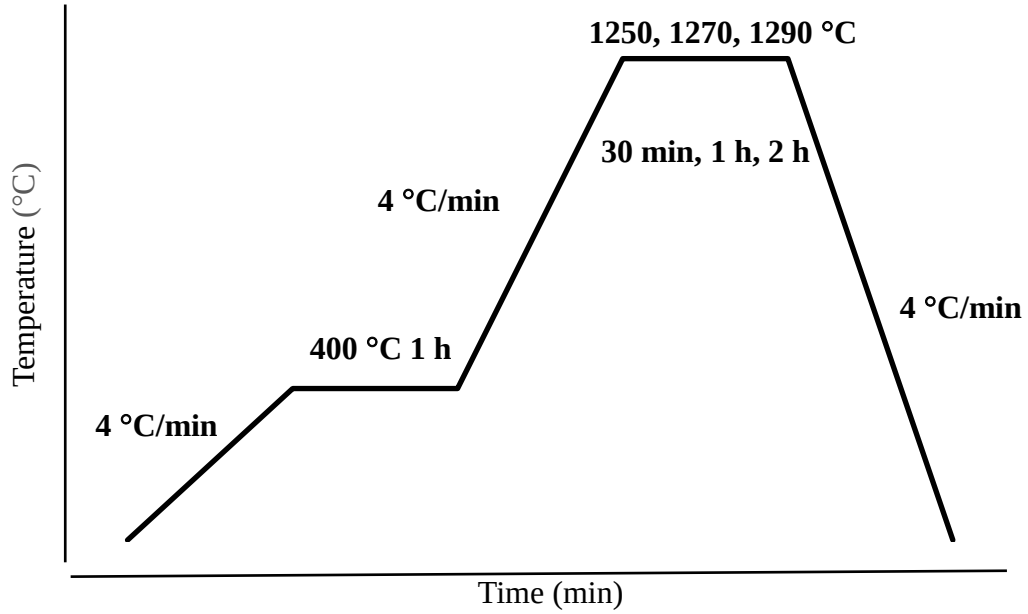

Figure 17. Time vs temperature graph of heat treatment applied for the production of $BaTiO_3$ based ceramic capacitors.

Figure 18. Sintered pellet.

A flowsheet showing the steps applied for the preparation of the $BaTiO_3$ based ceramic capacitors is shown in Figure 19.

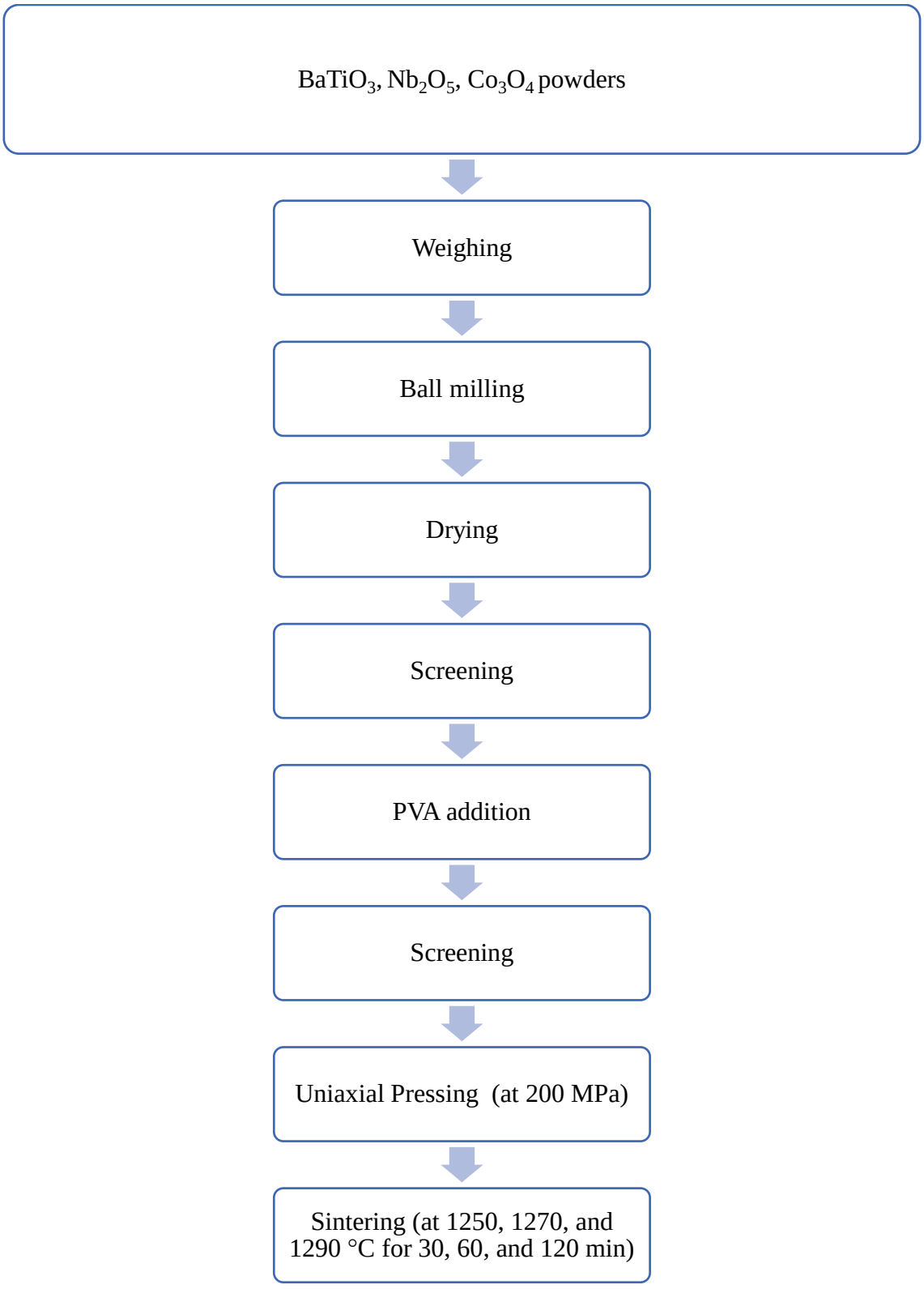

Figure 19. Flowsheet showing the steps applied for the preparation of the $BaTiO_3$ based ceramic capacitors.

3.2 Characterization of Samples

3.2.1 X-Ray Diffraction (XRD) Analysis

Identification of phase(s) and crystal structure for $BaTiO_3$, Nb_2O_5 added, Co_3O_4 added and, Nb_2O_5 and Co_3O_4 co-added $BaTiO_3$ ceramics were done using an X-Ray diffraction (XRD) analyzer (MiniFlex 300/600). Diffraction patterns were taken between 2θ angles of 20 and 80° using Cu Kα radiation (λ = 1.5418 Å). The operating voltage was 40 kV, current was 15 mA, and scan speed was 2 °/min. XRD patterns were investigated by PDXL integrated X-ray powder diffraction software.

3.2.2 Scanning Electron Microscopy (SEM) Examination

Microstructural analysis of starting powders and sintered ceramic bodies were performed using a scanning electron microscope (SEM, Zeiss MERLIN Field Emission Gun). Before the SEM examinations, samples were hot mounted with bakelite. After that the pellets were polished to obtain smooth surface. Pellets were etched chemically with HF and HNO_3 and washed with distilled water to enhance contrast on surface to visualize the microstructure. All the pellets were coated with Au-Pd conductive layers. Conduction was completed with carbon (C) bands. The applied operation voltage in SEM was 15 kV.

3.2.3 Energy Dispersive Spectroscopy (EDS) Analysis

Chemical compositions of all ceramics were determined by EDS detector attached to the SEM. Elemental analysis were done at 15 kV.

3.2.4 Particle Size Analysis

Particle size of starting powders was determined using Malvern Instruments Mastersizer 2000 particle size analyzer by Hydro 2000G accessory adapted. Dispersant used in laser measurements was distilled water. Measurable particle size range was 0.020 to 2000 μm. For each powder three measurements were done. Size measurement data was established by taking the mean average of the three measurements.

3.3 Property Measurements

3.3.1 Density

Density of sintered pellets were measured based on Archimedes' principle using an OHAUS PR series precision digital balance with ±0.0001 accuracy. Mass of the pellets were measured in dry form (w_{dry}), in xylene (w_{susp}) and, after saturated with xylene for 8 h (w_{sat}). Sintered density of the ceramics was calculated using the Equation shown below:

$$\rho_{bulk} = \frac{w_{dry} * \sum \rho_{liq}}{w_{sat} - w_{susp}} \qquad \text{Eq. 6}$$

Where:

ρ_{bulk} is the bulk density of sample

ρ_{liq} is the density of immersion liquid (xylene).

For each powder three measurements were done. Density determination data was established by taking the mean average of the three measurements.

3.3.2 Dielectric Properties

ε_r and tanδ values of $BaTiO_3$ based ceramics were measured using Hioki IM3536 Impedance analyzer. Before the measurements, surfaces of the pellets were ground and polished to obtain flat and parallel surfaces. SiC sandpapers were used for grinding from #80 to #1200 grids whereas; MD-Chem, and MD-Dac polishing clothes were used for polishing with suitable suspensions.

Parallel and flat surfaces of the pellets were printed with Heraeus silver paste to both sides with screen printing method. The silver paste applied on pellets were dried at 80 °C for 1 h. Then, the silver layer was heat treated at 950 °C for 30 min to stick to surface. Finally, two wires were connected to the silver coated surfaces by soldering process. The wires soldered to the surface of sample connected to the impedance analyzer (setup for dielectric measurement) were shown schematically in Figure 20.

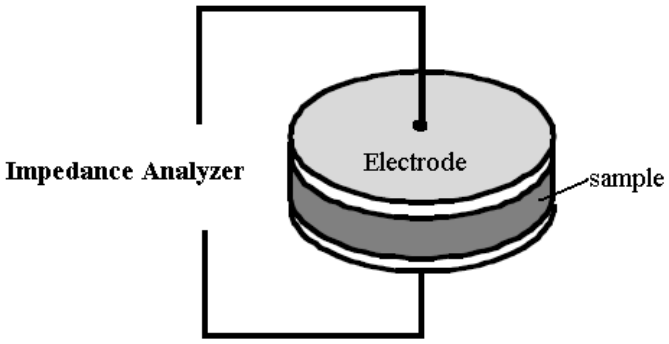

Figure 20. Schematically showing the dielectric measurement setup.

The impedance analyzer measures the C of the sample. The ε_r of a pellet is calculated using Equation 4. Temperature of sample measured by Type K thermocouple connected to the Testo 176T4.

C values of all ceramics were measured at 1 kHz frequency. DF values of ceramics were measured directly by impedance analyzer. Then, tanδ values were calculated accordingly.

3.3.3 Differential Scanning Calorimeter (DSC) Measurements

In the present study heat flux type DSC was used. The DSC measurements of ceramic samples was done by TA Instruments Discovery DSC 2500 Differential Scanning Calorimeter, with a refrigerated cooling system 90 accessory adapted. Before the measurements, sintered ceramics were crushed and ground to ~20 μm size using an agate mortar with pastle. Tzero Aluminum pan and Tzero DSC Sample Encapsulation Press is used to encapsulate samples. Scan speed was 5 °C/min between -50 and +150 °C. TRIOS software were used to analyze the data.

CHAPTER 4

RESULTS AND DISCUSSION

Results of the experimental study conducted on the preparation and dielectric properties of Nb_2O_5, Co_3O_4, and Nb_2O_5-Co_3O_4 added $BaTiO_3$ ceramics with controlled microstructure by conventional mixed-oxide route were presented and discussed in this chapter.

4.1 Characterization of Starting Powders

4.1.1 Barium Titanate Powder

Particle size histogram of $BaTiO_3$ starting powder is shown in Figure 21. Even though there is a small peak at ~0.4 μm size, the volume percentage of the particles accumulated around this size is quite small (~0.5%). Therefore, it is accepted that $BaTiO_3$ starting powder has unimodal particle size distribution. The size of the particles ranges from 0.22 to 12.62 μm. Particle size distribution of $BaTiO_3$ starting powder is shown in Table 7. Manufacturer suggests that the particle size of the $BaTiO_3$ is less than 10 μm. Particle size measurement of starting $BaTiO_3$ powder confirms the particle size data provided by the manufacturer.

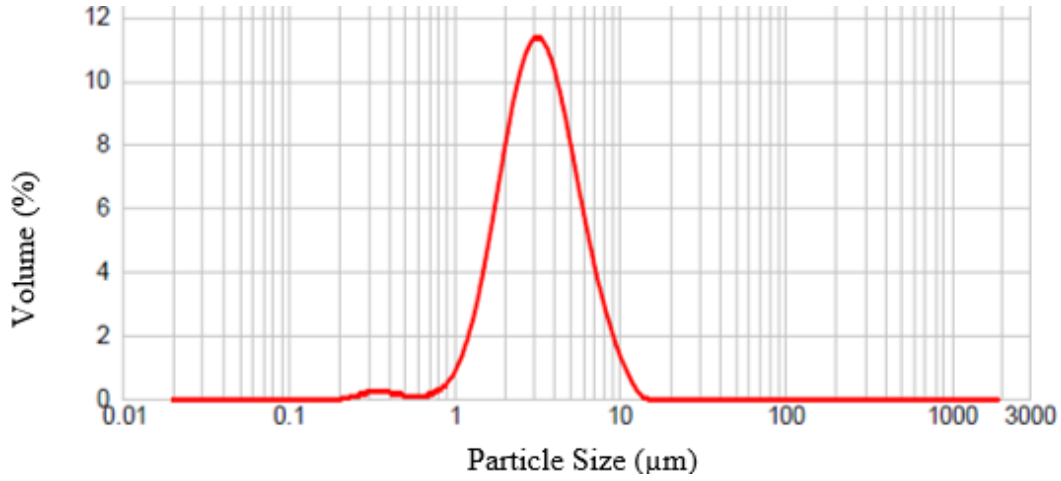

Figure 21. Particle size distribution histogram of $BaTiO_3$ starting powder.

Table 7. Particle size distribution of $BaTiO_3$, Co_3O_4, and Nb_2O_5 starting powders.

Distribution/Material	**$BaTiO_3$ powder**	**Co_3O_4 powder**	**Nb_2O_5 powder**
d (0.1) µm	1.63	0.19	11.06
d (0.5) µm	3.22	8.35	33.17
d (0.9) µm	6.42	24.31	67.69

The XRD pattern of $BaTiO_3$ starting powder is shown in Figure 22. All 2θ values of the XRD peaks for $BaTiO_3$ starting powder well matched with that of phase pure $BaTiO_3$ powder as defined by ICDD (International Centre for Diffraction Data) (PDF2.DAT). The characteristic peaks located at 22.6°, 32.0°, 39.4°, 45.8°, 51.48°, and 56.74° correspond to the (001), (101), (111), (200), (102), and (112) planes of the phase pure $BaTiO_3$ phase, respectively. At ~26° there is a weak peak which matches with TiO_2. The peak could present in the structure because of the production method of $BaTiO_3$ contains BaO and TiO_2 to mix and calcinate together. Similar results have been reported by Biglar et al. [56]. XRD pattern suggests that $BaTiO_3$ powder has almost the same peak positions with the data given in DB card number 00-075-2121 that reports that $BaTiO_3$ has perovskite structure and belongs to tetragonal crystal system with P4mm space group. It can be concluded that the starting $BaTiO_3$ powder is pure, and it has very small amount of TiO_2 impurity phases

that as detected by XRD instrument. But, it is anticipated that the presence of small amount of TiO_2 does not affect the results of this study since sintering could favor the more stable $BaTiO_3$ phase.

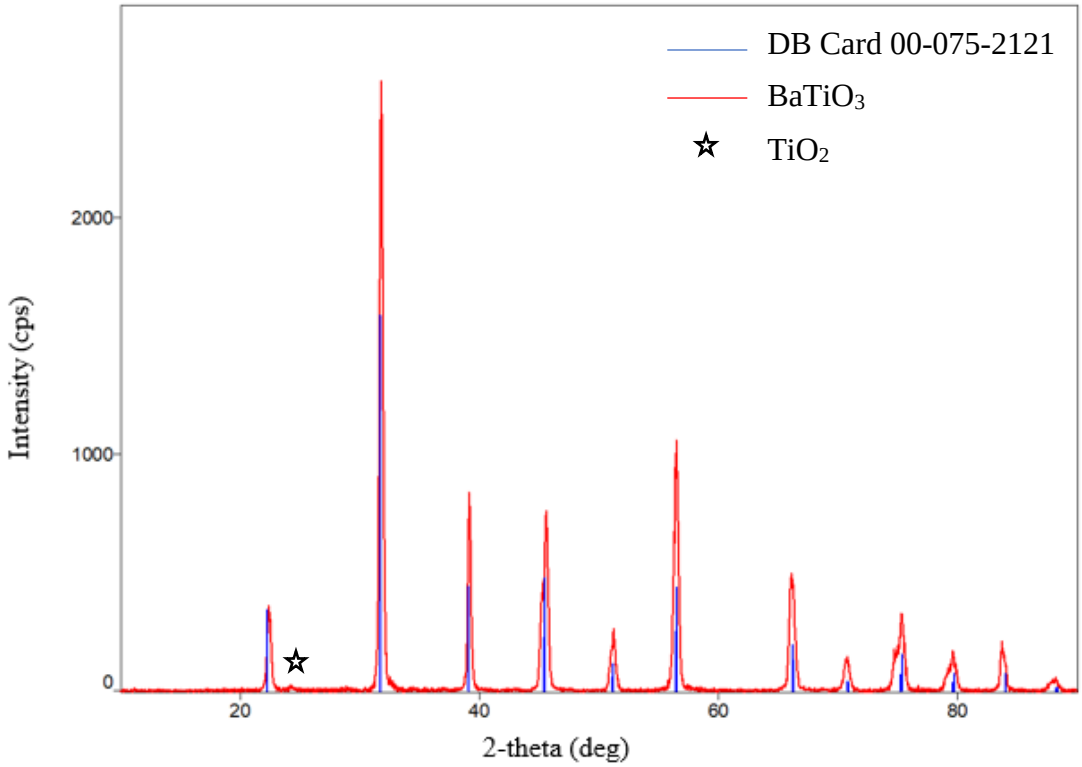

Figure 22. XRD pattern of $BaTiO_3$ starting powder.

A representative SEM image of $BaTiO_3$ is shown in Figure 23. SEM micrograph suggests that the powder consists of particles smaller than 10 µm. The particles are agglomerated and have virtually spherical in shape. The particle size measurement data collected from the SEM examinations supports the data gathered from the particle size analysis presented in Table 4 and in Figure 21.

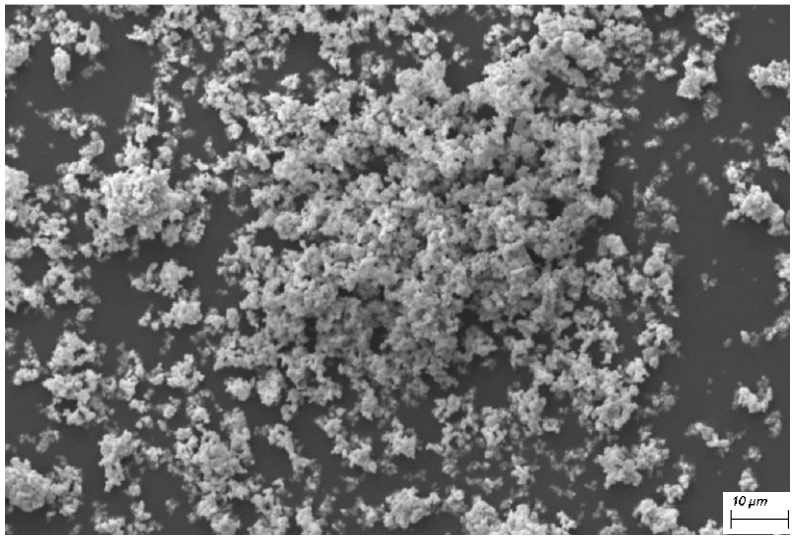

Figure 23. SEM image of $BaTiO_3$ starting powder.

4.1.2 Cobalt Oxide Powder

Particle size histogram of Co_3O_4 starting powder is shown in Figure 24. The histogram suggests that the powder has trimodal particle size distribution. The particle size of Co_3O_4 ranges from 0.04 to 50.24 µm. Size distribution of Co_3O_4 starting powder is presented in Table 7. Manufacturer suggests that the size of Co_3O_4 powder is less than 10 µm. The repeated measurements suggest that there are bigger particles than 10 µm. However, the volume percentage of bigger particles is small.

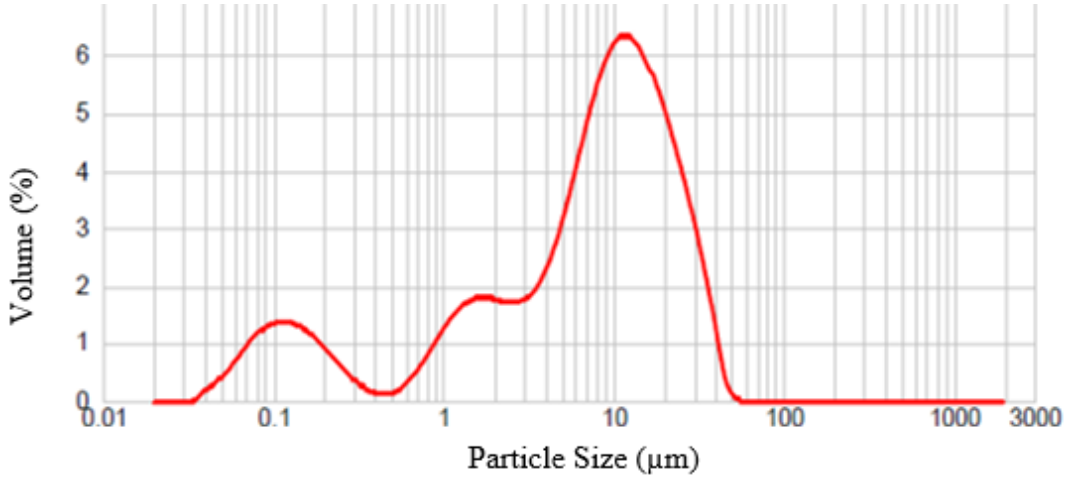

Figure 24. Particle size distribution histogram of Co_3O_4 starting powder.

The XRD pattern of Co_3O_4 starting powder is shown in Figure 25. All 2θ values of the XRD peaks for Co_3O_4 starting powder well matched with that of phase pure Co_3O_4 powder as defined by ICDD (International Centre for Diffraction Data). The characteristic peaks located at 31.37°, 36.94°, 38.69°, 44.85°, 55.79°, 59.54°, and 65.39° correspond to the (220), (311), (222), (400), (422), (511), and (440) planes of the phase pure Co_3O_4 phase, respectively. Similar results have been reported by Bielun et al. [57]. XRD pattern suggests that Co_3O_4 powder has almost the same peak positions with the data given in DB card number 00-074-1656 that reports that Co_3O_4 has cubic structure and belongs to trigonal crystal system with Fd-3m space group. It can be concluded that the starting Co_3O_4 powder is phase pure, and it does not have any impurity phases that can be detected by XRD measurements.

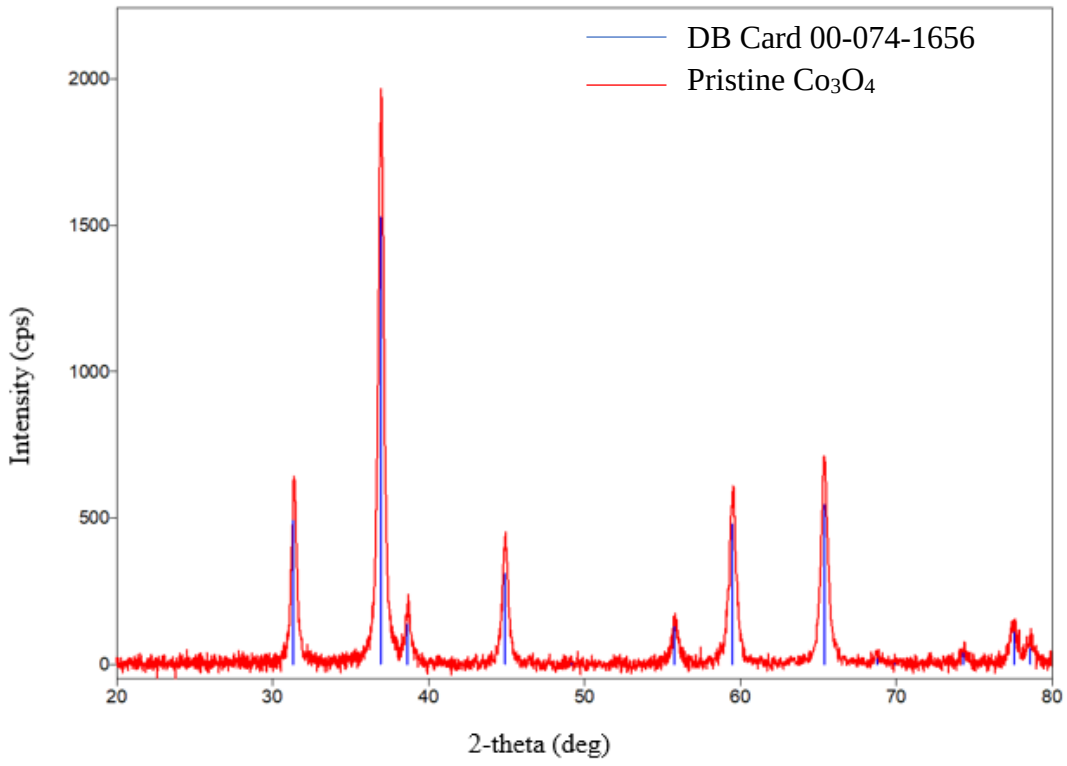

Figure 25. XRD pattern of Co_3O_4 starting powder.

SEM image of pristine Co_3O_4 powder is shown in Figure 26. As seen in the image, there are particles bigger than 10 µm. Image supports the results of particle size measurement histogram presented in Figure 24. Particle size distribution is inhomogeneous. Particle shapes are nearly spherical, and agglomeration was not observed.

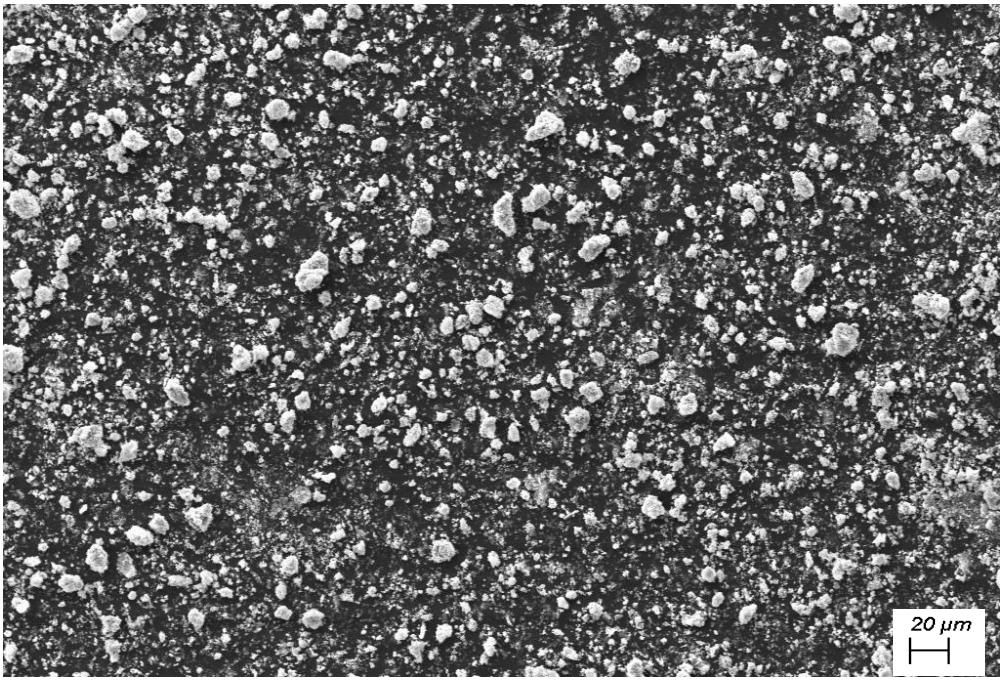

Figure 26. SEM image of Co_3O_4 starting powder.

4.1.3 Niobium Oxide Powder

In Figure 27, particle size measurement histogram of Nb_2O_5 starting powder is shown. The particle size distribution histogram of the Nb_2O_5 powder suggests that the powder has unimodal particle size distribution. The particle size of Nb_2O_5 ranges from 0.40 to 100.24 µm. Particle size distribution data for Nb_2O_5 starting powder is shown in Table 7. Nb_2O_5 have the biggest particle size among all three-starting powder.

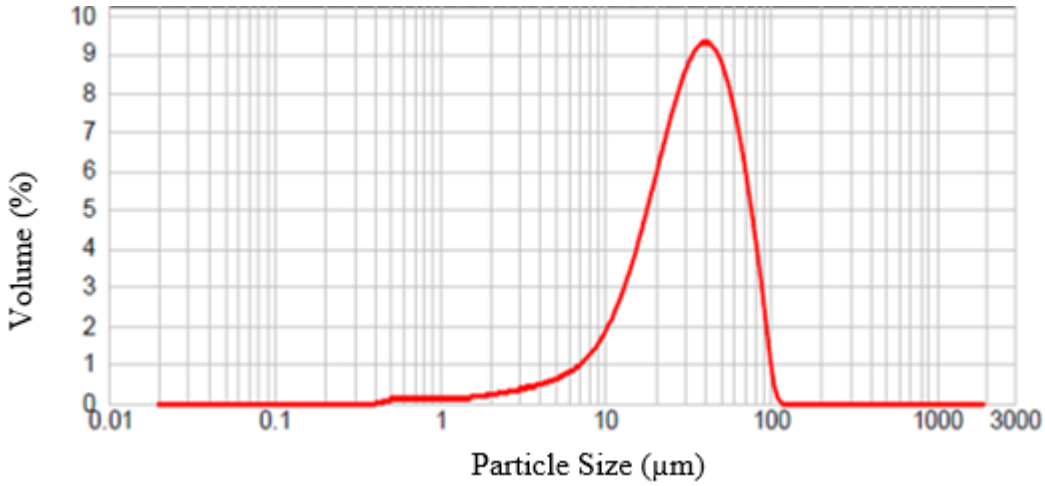

Figure 27. Particle size distribution histogram of Nb_2O_5 starting powder.

The XRD pattern of Nb_2O_5 starting powder is shown in Figure 28. All 2θ values of the XRD peaks for Nb_2O_5 starting powder matched with that of phase pure Nb_2O_5 powder as defined by ICDD (International Centre for Diffraction Data). The characteristic peaks located at 22.7°, 28.48°, 29.04°, 36,7°, 37.1°, and 47.7° correspond to the (001), (180), (200), (181), (201), and (002) planes of the phase pure Nb_2O_5 phase, respectively. Similar results have been reported by Marin et al. [58] and Liu et al. [59]. XRD pattern suggests that Nb_2O_5 powder has almost the same peak positions with the data given in DB card number 00-071-0005 that reports that Nb_2O_5 has cubic structure and belongs to monoclinic crystal system with P12/m1 space group. The undefined peaks in the pattern were searched and another pattern was taken between 20 and 55° at a lower scanning rate. These unmatched peaks are belonged to the orthorombic phase of Nb_2O_5. It can be concluded that the starting Nb_2O_5 powder has mixture of monoclinic and orthorhombic phases, and it does not have any impurity phases that can be detected by XRD measurements.

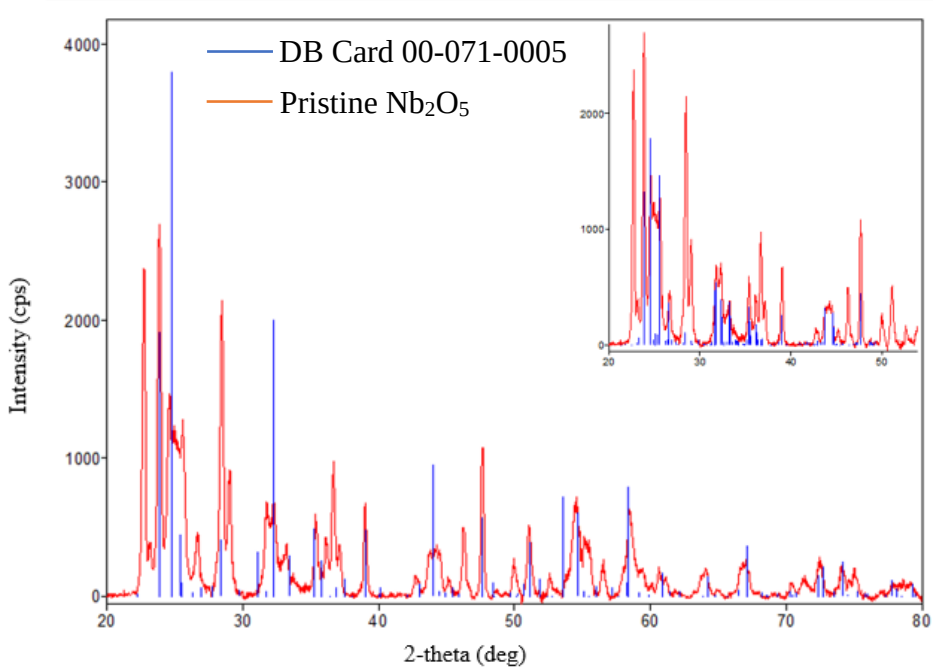

Figure 28. XRD pattern of Nb_2O_5 starting powder. (Inset shows the pattern between 20-55° at a scanning rate lower than the main pattern).

SEM image of pristine Nb_2O_5 particles is shown in Figure 29. Image shows that average particle size is between 40 and 50 µm. The image supports the particle size measurement histogram presented in Figure 24. The particles have irregular 3D shape and agglomeration was not observed.

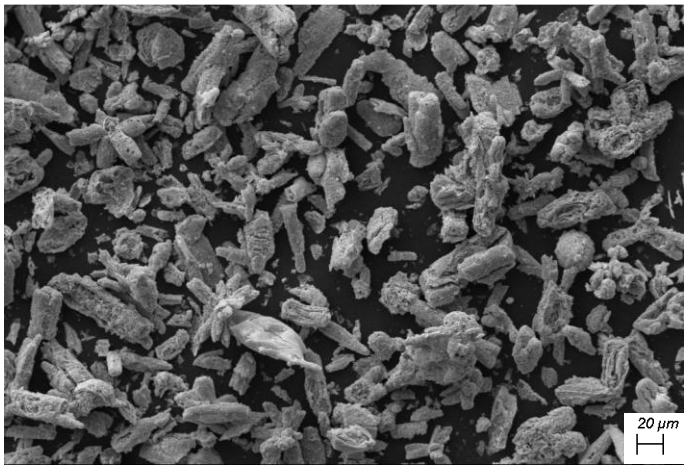

Figure 29. SEM image of Nb_2O_5 starting powder.

4.1.4 XRD Characterization of Ceramics Before Sintering

Ceramics with the composition mentioned at Table 6 are characterized by XRD analysis before sintering. Figure 30 shows that addition of Nb_2O_5 and Co_3O_4 to the $BaTiO_3$ affects the XRD results. The most intense peaks of Nb_2O_5 and Co_3O_4 could be seen in measurements at ~24° and ~39° respectively. $BaTiO_3$ peaks are not affected by Nb_2O_5 and Co_3O_4 addition before sintering. Measurements shows that the increased quantity of Nb_2O_5 and Co_3O_4 increases the intensity of relative peaks. For example, most Co_3O_4 added ceramic (Co3) has the highest Co_3O_4 peak intensity whereas decreasing Co_3O_4 content decreases the intensity of the peak. Measurements shows that before sintering the additions are present in the ceramics as a powder mixture. Measurements after sintering are given in Section 4.2.

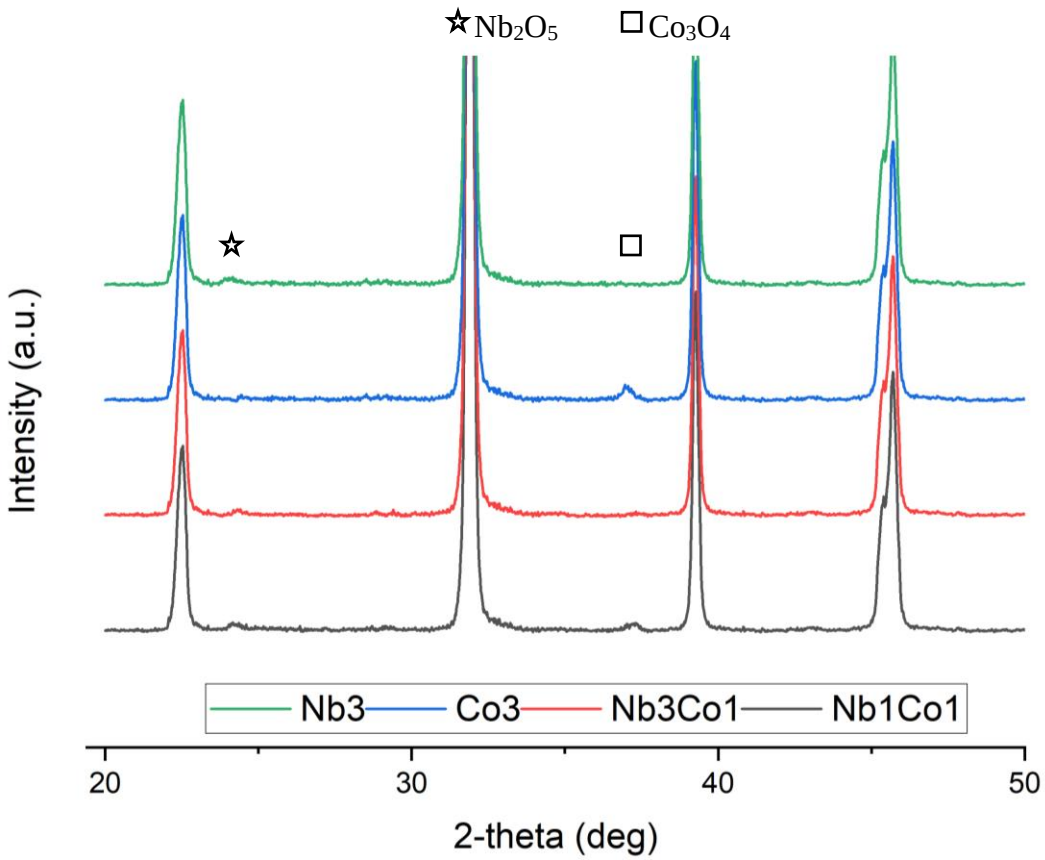

Figure 30. XRD patterns of ceramics before sintering.

4.2 Ceramic Preparation and Characterization

In order to see the compositional effect on the microstructure developed during processing, all other processing variables were kept constant. The samples were sintered at 1270 °C for 1 h in the same furnace at the same conditions.

4.2.1 Pristine $BaTiO_3$ Ceramics

4.2.1.1 XRD Analysis

The XRD pattern of $BaTiO_3$ ceramic remained unchanged after sintering the green pellet at 1270 °C, with respect to that of $BaTiO_3$ starting powder as mentioned at Section 4.1.1. The characteristic peaks located at 22.60°, 32.00°, 39.40°, 45.80°, 51.48°, and 56.74° corresponding to the (001), (101), (111), (200), (102), and (112) planes of the phase pure $BaTiO_3$ phase, respectively appeared more or less at the same diffraction angles. The analysis suggest that no additional phase developed during sintering.

4.2.1.2 Microstructural Analysis

The microstructure of $BaTiO_3$ ceramic sintered at 1270 °C for 1 h is shown in Figure 31. The image was taken with active electron back scattering detector (EBSD). Measured sizes of grains are in the sample varied between 5 and 7 μm. Grain sizes are close to each other implying that the microstructure developed during sintering is homogeneous. The pore sizes varied between 0.5 and 1.5 μm. Pore shape is spherical which means the sintering is advanced to the final stage of solid-state sintering. Measured density results will be presented later in Section 4.3.1.1. Fernandez et al. [60] observed a similar microstructure on the $BaTiO_3$ ceramic sintered at 1200 °C for 2 h. Even though sintering temperature is lower, longer sintering time may compensate to get similar results.

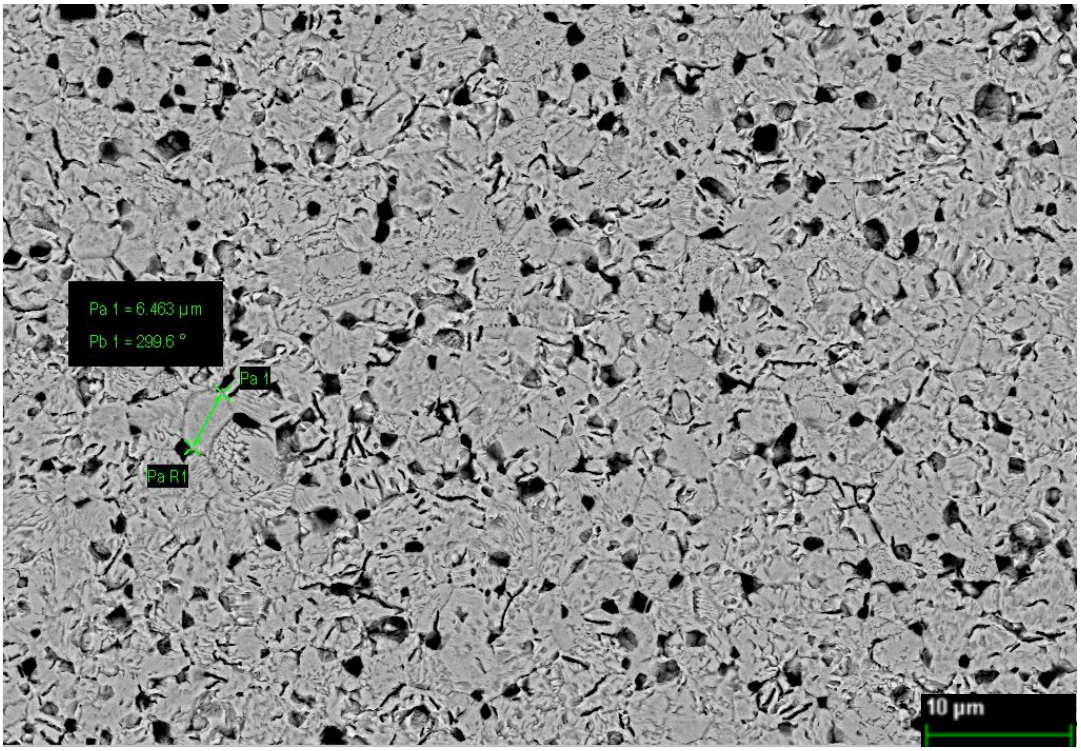

Figure 31. Microstructure of $BaTiO_3$ ceramic sintered at 1270 °C for 1 h.

4.2.1.3 EDS Analysis

The EDS analysis of $BaTiO_3$ ceramic sintered at 1270 °C for 1 h is shown in Figure 32. The analysis reveals that the ceramic consists of Ba, Ti, O, Al, Au, and Pd. The elements Ba, Ti, and O belong to starting powder. The at% of Ba and Ti are close to each other as expected since the Ba/Ti ratio in the unit formula is 1. The O content is somehow lesser than expected value, but the EDS method could have measurement tolerance for low keV values because the atomic number of O is small and close to the measurement limits. Li et. al. [61] reported akin results for the EDS analysis taken at similar voltage and intensity values for $BaTiO_3$ ceramic.

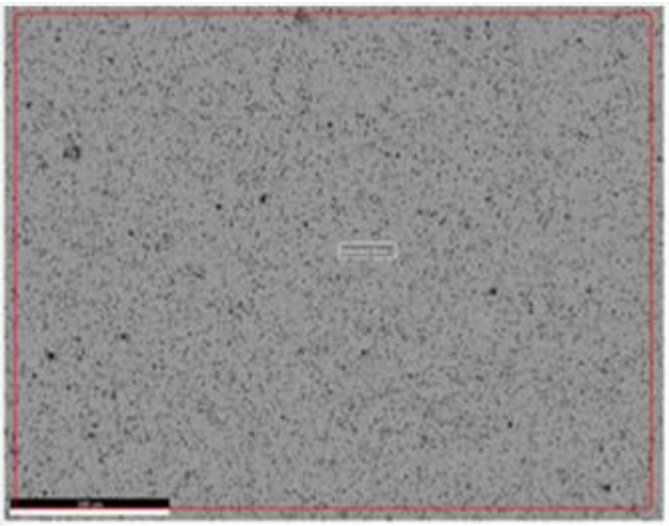

Element	Weight%
O	11.61
Al	0.91
Au	3.21
Pd	1.714
Ba	63.08
Ti	19.45

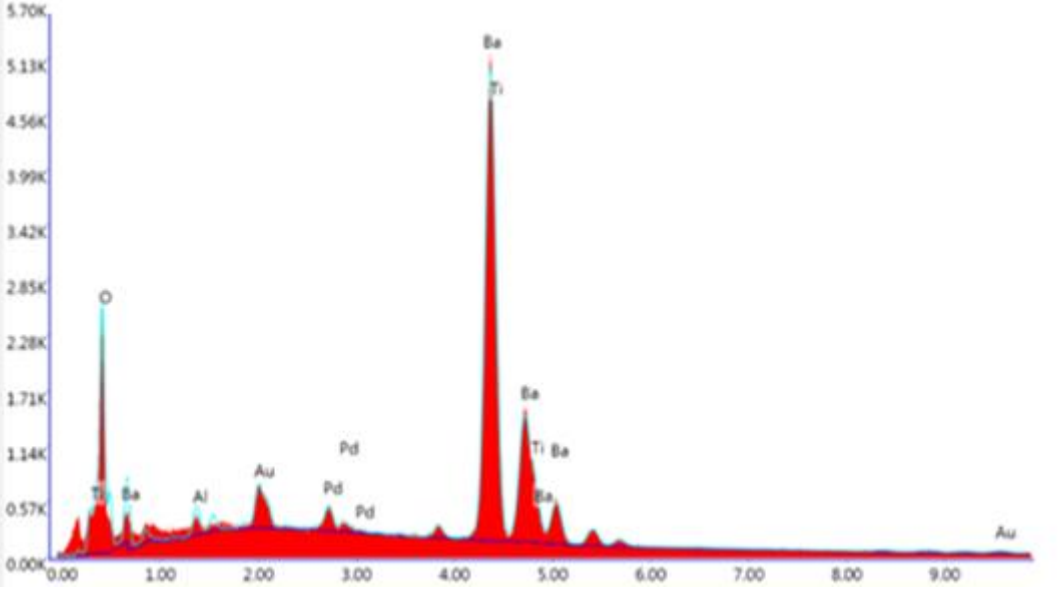

Figure 32. EDS analysis of $BaTiO_3$ ceramic sintered at 1270 °C for 1 h.

The Al content of the ceramic is assumed to be caused during the milling process since the jar used for the ball milling is made from Al_2O_3. Au and Pd peaks are detected because the ceramics are sputter coated to be able to get the required conductivity in the ceramics for the SEM analysis.

4.2.2 Nb_2O_5 Added $BaTiO_3$ Ceramics

4.2.2.1 XRD Analysis

The XRD pattern of the Nb_2O_5 added $BaTiO_3$ ceramic is shown in Figure 33. All 2θ values of the major peaks matched with the XRD peaks of the $BaTiO_3$ phase as defined at ICDD DB card number 00-051-0402 where it was stated that Nb_2O_5 added $BaTiO_3$ ceramic belongs to cubic crystal system with Pm-3m space group. The characteristic peaks located at 22.18°, 31.55°, 38.92°, 45.20°, 50.91°, 56.17°, and 65.85° correspond to the (001), (101), (111), (200), (102), (112), and (221) planes, respectively, of the $BaTiO_3$ phase. Cui et al. [62] reported that the XRD pattern of more than 1.5 mole% Nb_2O_5 added $BaTiO_3$ ceramics sintered at 1250 °C for 2 h indicated a weak peak at ~27° belonging to $Ba_6Ti_{17}O_{40}$ phase. Very small peak detected at ~27° in Figure 33 may belong to $Ba_6Ti_{17}O_{40}$ phase. A second peak belonging to $Ba_6Ti_{17}O_{40}$ phase was not detected separately though it may overlap with the peaks belonging to $BaTiO_3$ phase. The peak belonging to $Ba_6Ti_{17}O_{40}$ phase is weak since the concentration of Nb_2O_5 is low, i.e., 1.5 mole%. Since the $Ba_6Ti_{17}O_{40}$ phase consists of high Ti content, the Nb atoms could incorporate the similar ionic size Ti atoms in $BaTiO_3$ phase and by segregation of that Ti atoms produced $Ba_6Ti_{17}O_{40}$ phase. It can be concluded that Nb atoms doped the $BaTiO_3$ structure and replaced some Ti atoms.

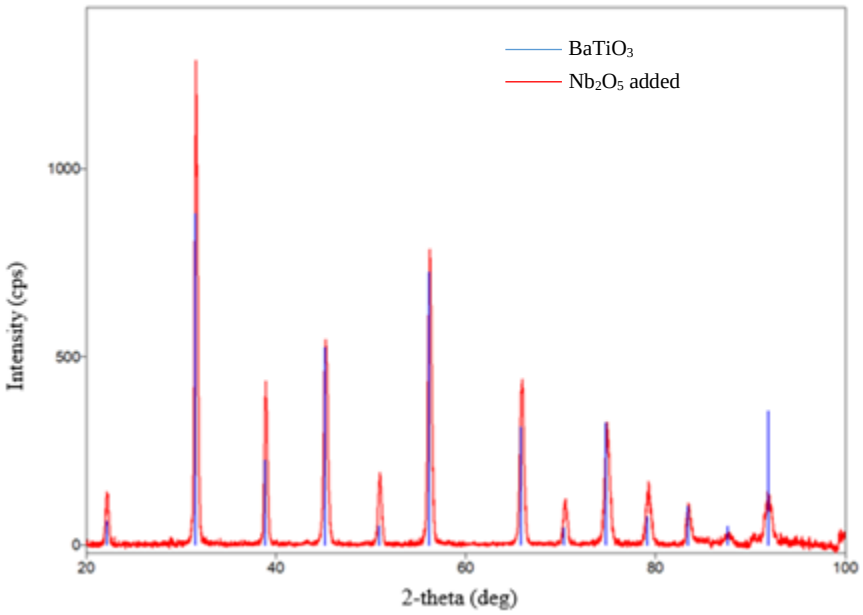

Figure 33. XRD pattern of 1.5 mole% Nb_2O_5 added $BaTiO_3$ ceramic sintered at 1270 °C for 1 h.

4.2.2.2 Microstructural Analysis

A SEM image of the 1.5 mole% Nb_2O_5 added $BaTiO_3$ ceramic is shown in Figure 34 a. Low concentrations of Nb^{5+} in $BaTiO_3$ ceramic moderately suppress the grain growth to improve several physical properties. In the present study, it is analyzed that Nb^{5+} ions exist in high concentrations at or near the grain boundary to suppress abnormal grain growth during sintering and promote the formation of fine grains. A SEM image taken at a larger magnification for 1.5 mole% Nb_2O_5 added $BaTiO_3$ is presented in Figure 34b.

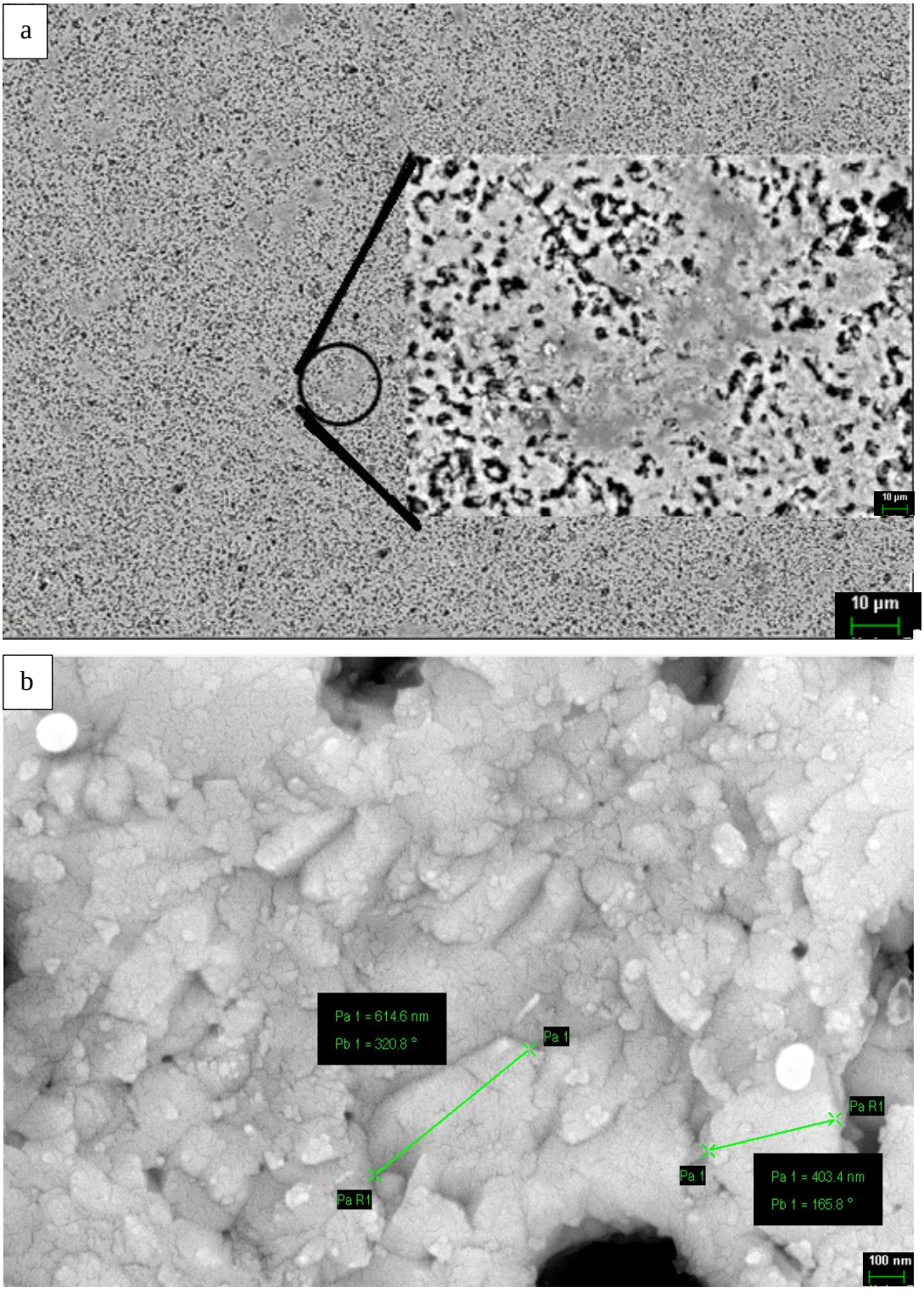

Figure 34. SEM images of 1.5 mole% Nb_2O_5 added $BaTiO_3$ ceramics sintered at 1270 °C for 1 h. a) Inset image was taken when SED is active. b) EBSD image.

Size analysis reveal that the microstructure is made up of grains with size between 400 and 700 nm. This shows that the Nb_2O_5 addition to the $BaTiO_3$ ceramic could inhibit the grain growth since the grains in $BaTiO_3$ have approximately 6 μm in size (Figure 31). Inhibition of grain growth is also very important to obtain better dielectric properties such as higher ε_r. Hoshina [63] reported that the optimum dielectric properties of $BaTiO_3$ based ceramics can be obtained at grains in the size range of 900-1300 nm.

Also, Brzozowski et al. [64] and Hoshina et al. [63] stated that for Nb_2O_5 concentrations of 0.30–0.60 mole%, the uniform dopant distribution allows its complete incorporation into the $BaTiO_3$ lattice. As most of the Nb^{5+} ions solubilize into the $BaTiO_3$ lattice, there is an important segregation of Ti in the whole system. In this case, the Ti ions contribute to the second phase formation, which becomes close to the composition $Ba_6Ti_{17}O_{40}$. Due to the high incorporation of Nb^{5+} in the $BaTiO_3$ lattice, an important shrinkage of the host lattice takes place. When secondary electron detector (SED) is active, some of these phases could be identified as more gray colored areas as shown in Figure 34a. To be able to observe these phases clearly, EBSD active imaging is done. A representative EBSD image is shown in Figure 34b.

EBSD imaging shows the higher atomic number ceramics brighter. The needle-like structures are more pronounced and relatively darker in color in the SEM image. Color of needle-like structures is darker than the rest of the microstructure. Since $Ba_6Ti_{17}O_{40}$ phase have more percentage of Ti atoms than the $BaTiO_3$ phase, dark colored areas could be assigned to $Ba_6Ti_{17}O_{40}$ phase. Also, EDS results shows that the Nb content at the darker needle-like structure zones are higher than the rest of the microstructure as shown in the inset in Figure 34a. Distribution of these needle-like structures are homogeneous throughout the ceramic. So, it can be concluded that Nb distribution is homogenous across the ceramic. The needle-like structures have been also observed by Cui et al. [65].

4.2.2.3 EDS Analysis

EDS analysis of the Nb doped $BaTiO_3$ ceramic, shown in Figure 35, proves that the microstructure consists of the elements Ba, Ti, O, Au, Pd, and Al. The image was taken from the red box in Figure 35. Ba, Ti, and O comes from $BaTiO_3$ starting powder. Au and Pd peaks come from the sputter coating which is used to be able to image under SEM. Al peaks present because of ball milling process that utilized a jar made of Al_2O_3. Nb should be present in the structure. But it is not detected in the EDS analysis because the Nb peaks overlaps with Au peaks. To prove Nb existence in the structure and spot the distribution of Nb atoms EDS elemental mapping is done.

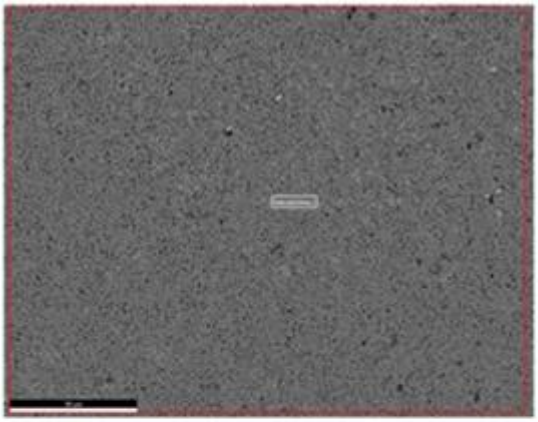

Element	Weight%
O	12.95
Al	0.84
Au	4.58
Pd	2.2
Ba	58.26
Ti	21.17

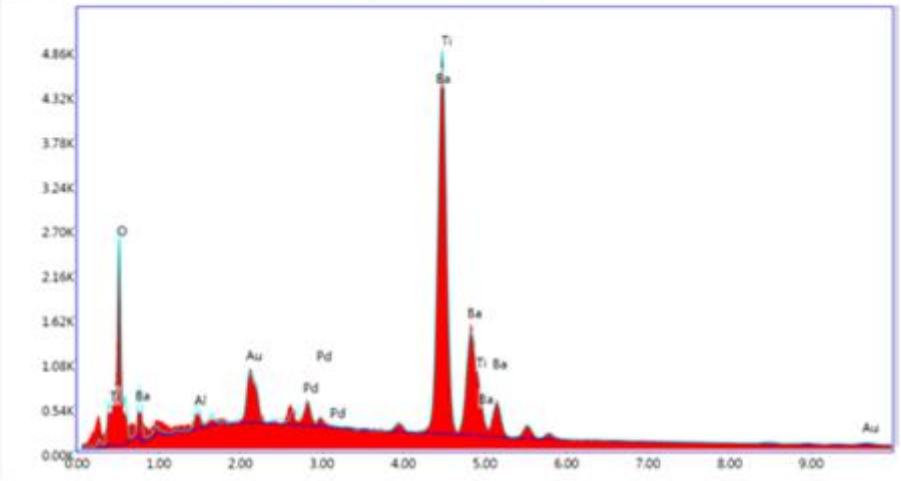

Figure 35. EDS analysis of Nb doped $BaTiO_3$ ceramics sintered at 1270 °C for 1 h.

The distribution of Nb, Ba, and Ti in microstructure is shown by EDS mapping in Figure 36a, b, and c, respectively. The analyses revealed that Nb is present in the structure and distributed homogenously. There are some dark colored spaces in the Nb mapping. The reason for this could be core-shell structures in the microstructure. The cores could contain $BaTiO_3$ phase while the surrounding structures contains Nb doped $BaTiO_3$ phase. EDS mapping of Nb doped $BaTiO_3$ has not been presented elsewhere in open literature for comparison.

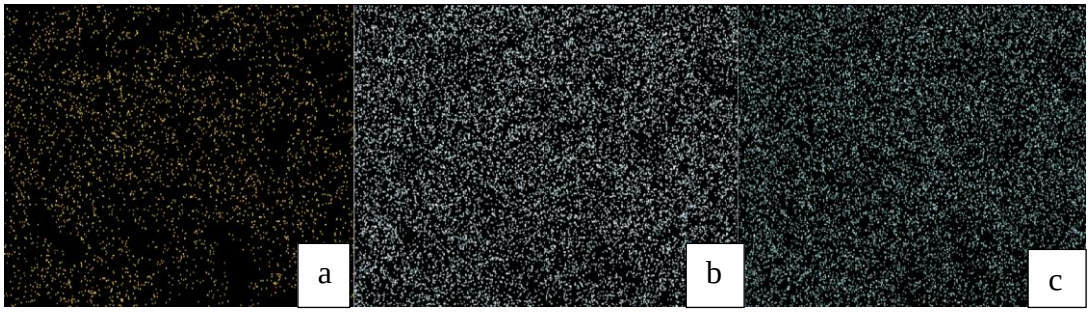

Figure 36. (a) Nb, (b) Ba, and (c) Ti atoms in EDS mapping of Nb doped $BaTiO_3$ ceramic.

4.2.3 Co_3O_4 Added $BaTiO_3$ Ceramics

4.2.3.1 XRD Analysis

The XRD pattern for 1 mole% Co_3O_4 added $BaTiO_3$ ceramic is shown in Figure 37. All 2θ values of XRD peaks show similar peak positions with $BaTiO_3$, and match with the same DB card. The characteristic peaks located at 22.59°, 31.87°, 39.22°, 45.57°, 51.29°, and 56.53° correspond to the (001), (101), (111), (200), (102), and (112) planes of the $BaTiO_3$ phase, respectively. But the peaks shifted 0.1° to the left suggesting that the Co atoms doped into the $BaTiO_3$ cells. No peak belonging to Co_3O_4 phase were detected implying that all Co could be doped into the $BaTiO_3$ crystal structure. Similar results with peak shifts upon doping of Co to $BaTiO_3$ structure have been reported by Padilla et al. [12] and claimed that Co substitution

on the $BaTiO_3$ structure shifts the (2 0 0) reflection at 44°, which is characteristic of the cubic lattice of Co doped $BaTiO_3$.

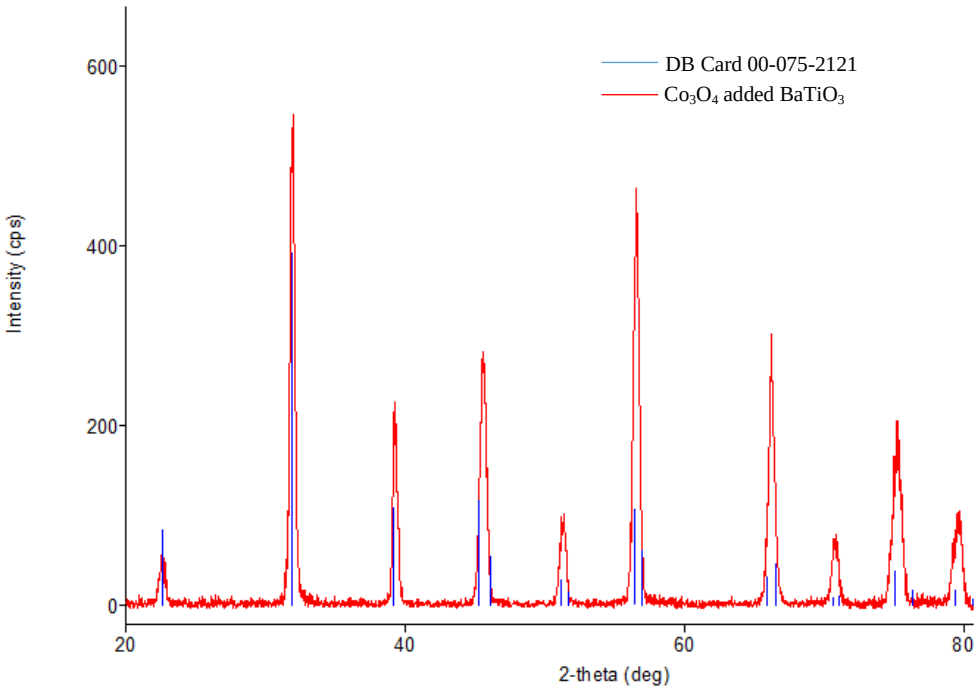

Figure 37. XRD pattern of 1 mole% Co_3O_4 added $BaTiO_3$ ceramic sintered at 1270 °C for 1 h.

4.2.3.2 Microstructural Analysis

A SEM image of the Co_3O_4 added $BaTiO_3$ ceramic is shown in Figure 38 a. Image shows that the Co_3O_4 addition to $BaTiO_3$ makes microstructure consists of smaller grains when it is compared to the microstructure of $BaTiO_3$ ceramic shown in Figure 40. Co affects the microstructure by inhibiting grain growth, thus decreases pore size. Grain size data displayed in Figure 38 b reveal that the 1 mole% Co_3O_4 added $BaTiO_3$ ceramics have grain sizes ranging from 500 to 900 nm. The Co_3O_4 addition inhibited the abnormal grain growth, thus made the structure denser. Langhammer et al. [11] observed the development of rod like grains when Co doped $BaTiO_3$ ceramic was sintered at 1400 °C. Rod like grains were not observed in the present study because the sintering temperature was lower.

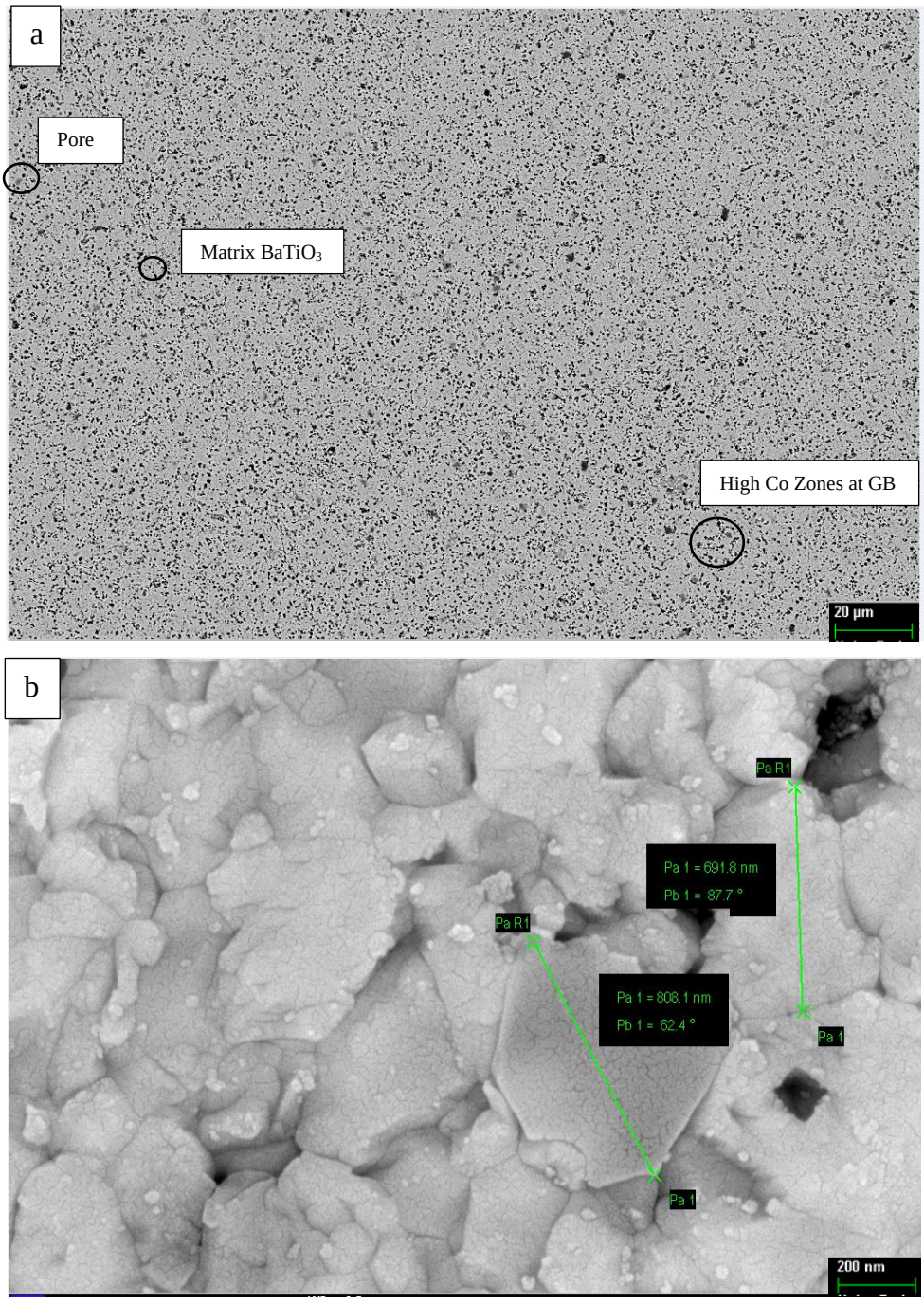

Figure 38. SEM images of 1 mole% Co_3O_4 added $BaTiO_3$ ceramic sintered at 1270 °C for 1 h. (a) Low magnification. (b) High magnification for grain size measurement.

4.2.3.3 EDS Analysis

EDS analysis of the Co doped $BaTiO_3$ ceramic, shown in Figure 39, proves that the microstructure consists of the elements Ba, Ti, O, Au, and Pd. The image was taken from the red box in Figure 39. Ba, Ti, and O comes from $BaTiO_3$ starting powder. Au and Pd peaks come from the sputter coating which is used to be able to image under SEM. Co should be present in the structure. But it was not detected on the EDS analysis probably due to low Co content of the sample. In order to prove the existence of Co in the structure and spot the distribution of Co atoms EDS elemental mapping was done.

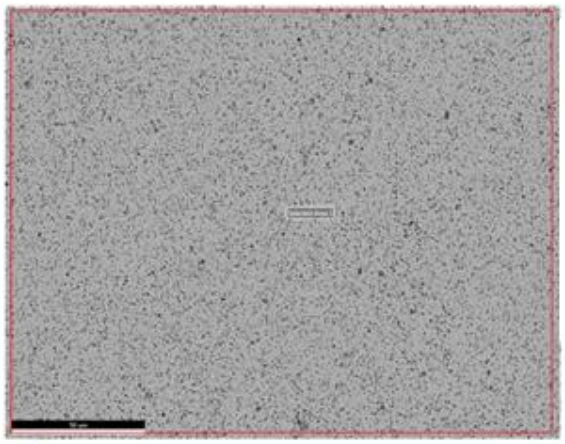

Element	Weight%
O	14.53
Au	3.79
Pd	2.04
Ba	57.2
Ti	22.44

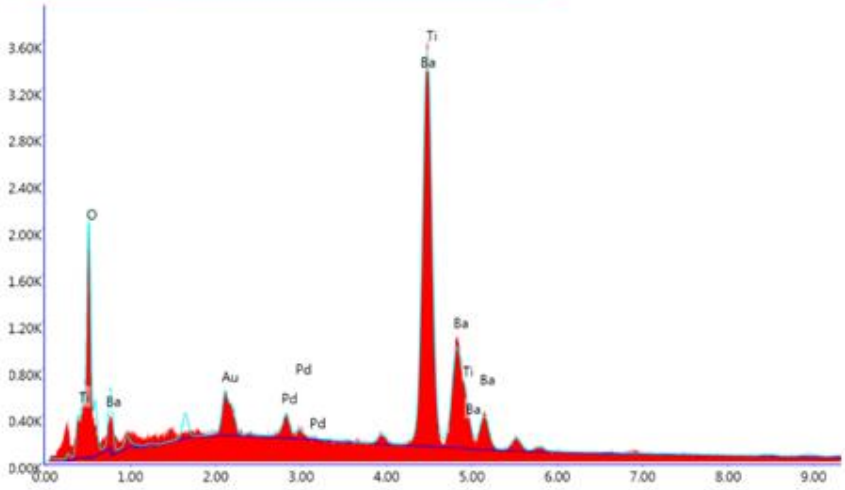

Figure 39. EDS analysis of the Co doped $BaTiO_3$ ceramic sintered at 1270 °C for 1 h.

The distribution of Co, Ba, and Ti in the microstructure is shown by EDS mapping in Figure 40a, b, and c, respectively. The analyses revealed that Co is present in the structure and has a uniform distribution. Figure 40b and c show that the Ba and Ti atoms have also uniform distribution in the structure which means that the $BaTiO_3$ is the main component in this composition. Similar distribution of Co atoms has been obtained by Baiju et al. [66] with 1 mole% Co_3O_4 added $BaTiO_3$ synthesized by hydrothermal method.

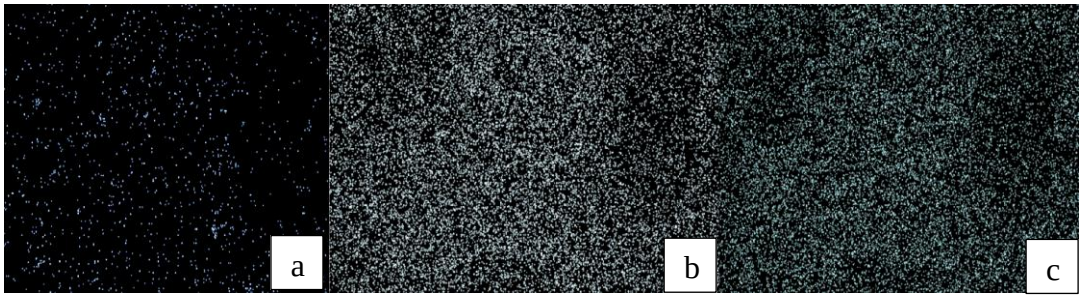

Figure 40. EDS mapping analysis of 1 mole% Co_3O_4 added $BaTiO_3$ ceramic sintered at 1270 °C for 1 h. (a) Co, (b) Ba, and (c) Ti.

4.2.4 Nb_2O_5-Co_3O_4 Co-Added $BaTiO_3$ Ceramics

4.2.4.1 XRD Analysis

XRD patterns of Nb1Co1 and Nb3Co1 ceramics were presented in Figure 41. Characteristic XRD peaks located at 2θ of 22.67°, 31.88°, 39.32°, 45.66°, 51.15°, and 56.53° for Nb3Co1 ceramic correspond to the (001), (101), (111), (200), (102), and (112) planes of $BaTiO_3$. XRD peaks for Nb1Co1 ceramic located at 22.44°, 31.77°, 39.41°, 45.56°, 51.26°, and 56.53° correspond to the (001), (101), (111), (200), (102), and (112) planes of $BaTiO_3$. XRD patterns shows that both ceramics have nearly the same peak positions with $BaTiO_3$ ceramic though there is slight shift in the 2θ values of the peaks. Both Nb3Co1 and Nb1Co1 showed a peak shift to the left as compared to $BaTiO_3$. Also, there is not any peaks belonging to Nb_2O_5 or Co_3O_4 phases suggesting that Nb and Co doped together into the $BaTiO_3$ crystal

structure. Osoro et al. [67] claims that when Nb/Co ratio is equal to 1 the hexagonal form of $BaTiO_3$ can be observed, resulting in the formation of oxygen vacancies in $BaTiO_3$, probably because there is not enough Nb to fully balance the charge defects induced by the substitution of Ti by Co. In contrast, when Nb/Co ratio is equal to 2, hexagonal form is not observed. The crystal structure of $BaTiO_3$ changes gradually from the tetragonal form to the cubic form. The broader peaks observed are attributed to composition heterogeneities present in the structure.

The 2nd and 4th peaks of the Nb3Co1 ceramic have similar intensities while the same position peaks in Nb1Co1 ceramic have larger difference in intensity. This shows that both ceramics doped with different amount so that the crystal structure undergoes a change. Similar shifts were reported by Osoro et al. [67] which supports the idea of structure changed gradually from the tetragonal to cubic.

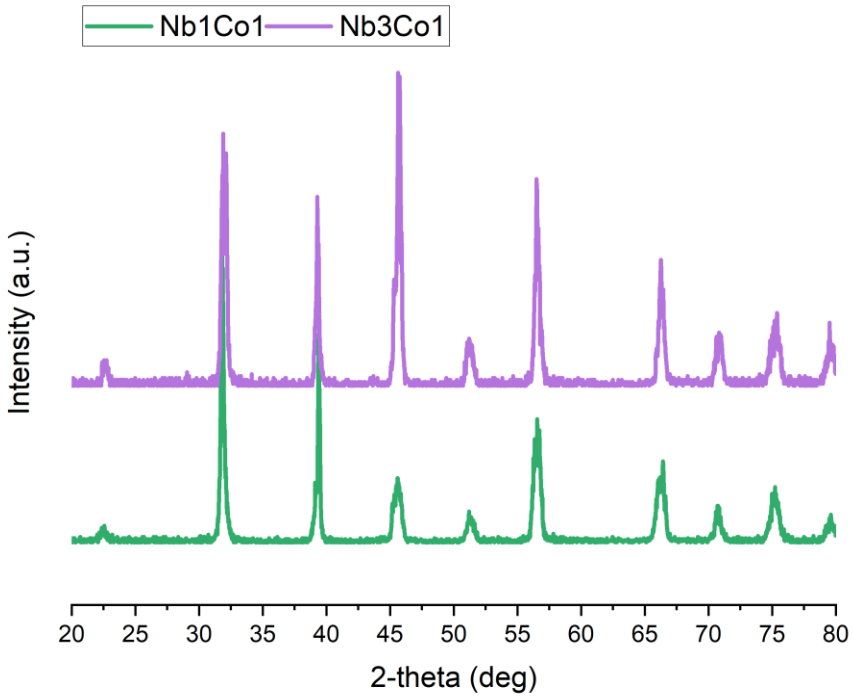

Figure 41. XRD pattern of Nb1Co1 and Nb3Co1 ceramics sintered at 1270 °C for 1 h.

4.2.4.2 Microstructural Analysis

Main difference between two images shown in Figure 42 is the presence of $Ba_6Ti_{17}O_{40}$ phase. Nb doping is linked with $Ba_6Ti_{17}O_{40}$ phase formation as mentioned in Section 4.2.3. Increase of the Nb content causes the formation of $Ba_6Ti_{17}O_{40}$ phase. Both images show that $Ba_6Ti_{17}O_{40}$ distributed in the microstructure homogenously. The pore amounts of ceramics are more or less the same. Matrix color difference between the images caused by the brightness settings of SEM imaging method.

Grain size measurements of Nb1Co1 and Nb3Co1 ceramics revealed that the average grain size for Nb1Co1 ceramic is 1.2 μm, while that for Nb3Co1 ceramic is 0.8 μm as shown in Figure 43a and b, respectively. The measurement data proves that Nb is better grain growth inhibitor than Co for $BaTiO_3$ ceramics. This finding is important for dielectric properties because grain size is directly affecting the dielectric properties of the ceramics [63].

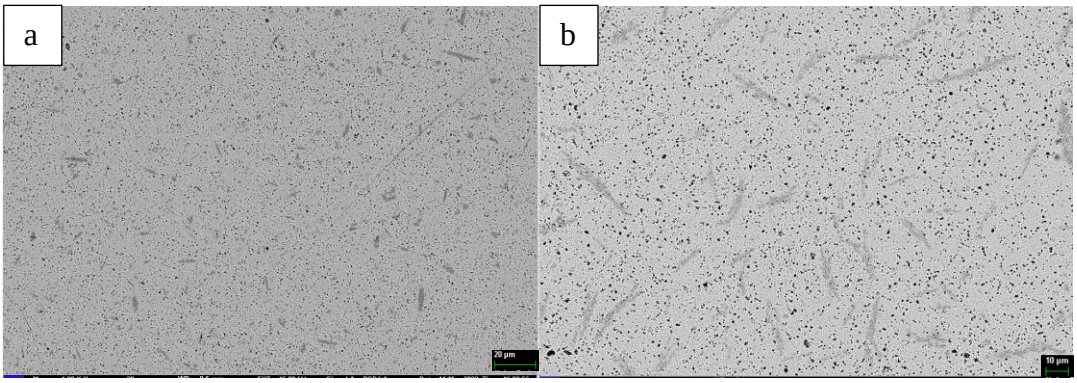

Figure 42. SEM images for (a) Nb1Co1 and (b) Nb3Co1 ceramics sintered at 1270 °C for 1 h. Images were taken with EBSD detector active.

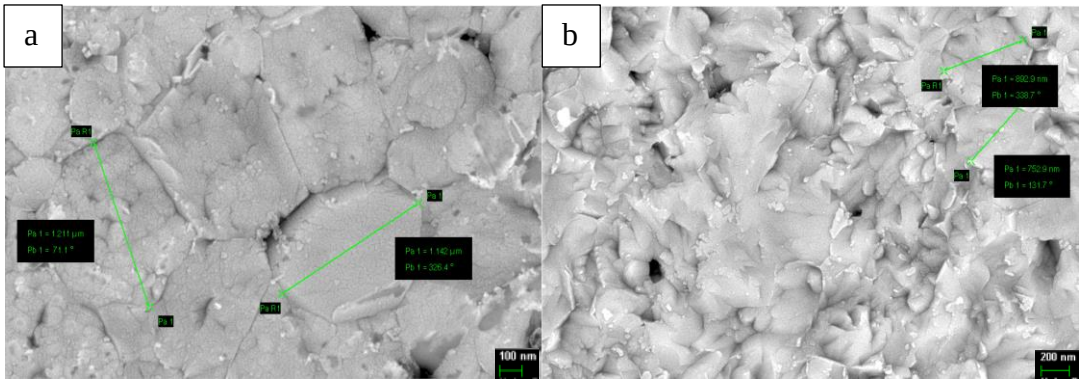

Figure 43. Grain size measurements of (a) Nb1Co1 and (b) Nb3Co1 ceramics sintered at 1270 °C for 1 h.

Hennings and Schreinmacher [19] reported that although Nb_2O_5 and Co_3O_4 powders were separately added to $BaTiO_3$, the grain shells generally contained a combination of both elements in a ratio close to Nb : Co= 2 : 1. Regions with high concentration of Nb thus always showed a comparably high concentration of Co. This effect of so-called 'co-solubility' suggests that both elements preferably enter the perovskite lattice as the complex $[Nb^{5+}_{2/3}Co^{+2}_{1/3}]^{4+}$, rather than as separate Nb^{5+} donors or Co^{2+} acceptors.

4.2.4.3 EDS Analysis

Figure 44 and Figure 45 shows the images taken from the EDS mapping analysis for Nb1Co1 and Nb3Co1 ceramics, respectively. Main difference between these figures is the Nb and Co contents. In Figure 45, Nb content is more than that in Figure 44. On the other hand, Co content contrasts with Nb content, Nb1Co1 ceramic has more Co content than Nb3Co1 ceramic. This verifies that the compositions are preserved throughout the sintering process. EDS mapping of similar compositions are reported by Chazono and Kishi [8] and claimed that Ba and Ti were distributed inhomogeneously, Nb and Co distributed homogeneously in the similar composition sample.

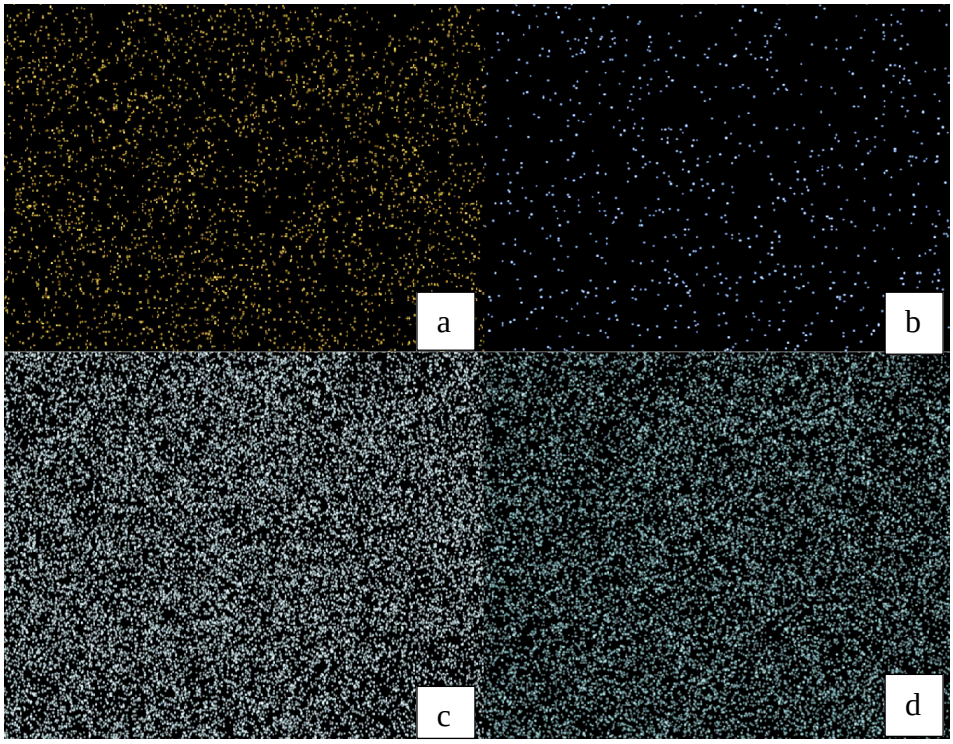

Figure 44. EDS mapping analysis of Nb1Co1 ceramic sintered at 1270 °C for 1 h. (a) Nb, (b) Co, (c) Ba, and (d) Ti.

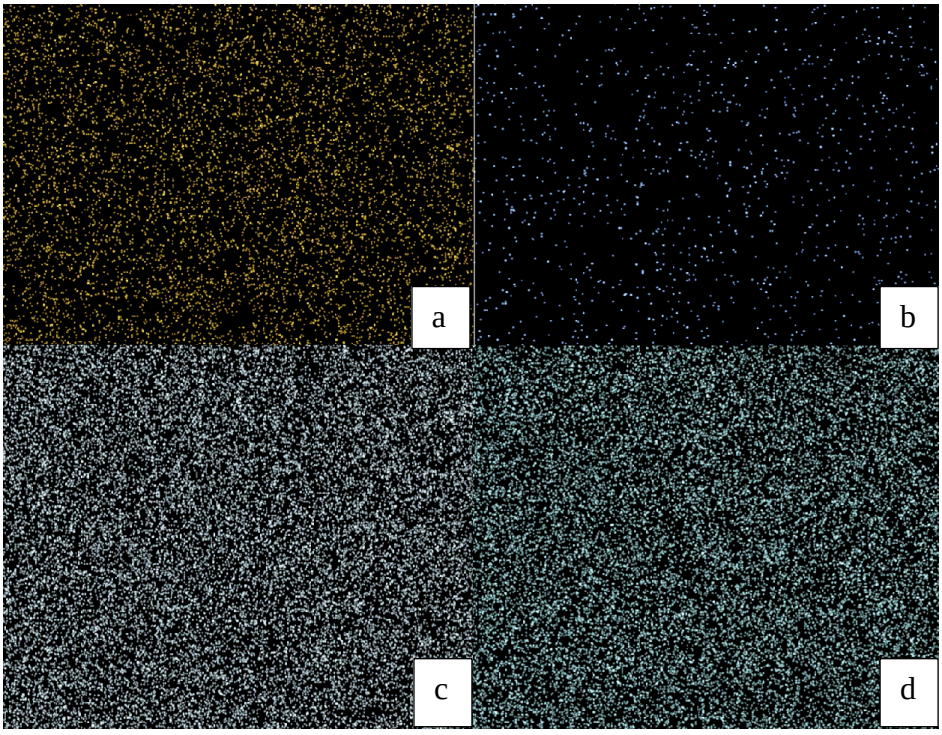

Figure 45. EDS mapping analysis of Nb3Co1 ceramic sintered at 1270 °C for 1 h. (a) Nb, (b) Co, (c) Ba, and (d) Ti.

4.3 Property Measurements

4.3.1 Pristine $BaTiO_3$ Ceramics

4.3.1.1 Density Measurements

Table 8 shows the density data for three different $BaTiO_3$ ceramics sintered at 1270 °C for 1 h. Average density relative to the theoretical density is ~95.5%. Ertuğ et al [68] stated that two-step sintering at 900 and 1100 °C led to 95% relative density. In the study of Panteny et al. [69] $BaTiO_3$ ceramics was produced with final relative density of 94.5%, and they claimed that it is a typical densification value. In the light of abovementioned information, a densification of ~95.5% was considered satisfactory in this study. It is obvious that sintering at 1270 °C for 1 h results in satisfactory densification for $BaTiO_3$ ceramics to be used in capacitor applications.

Table 8. Density data for three $BaTiO_3$ ceramics sintered at 1270 °C for 1 h.

	Experimental Density (g/cm^3)	**Theoretical Density (g/cm^3)**	**Relative Sintered Density (%)**
$BaTiO_3$-1	5.74	6.02	95.29
$BaTiO_3$-2	5.76	6.02	95.71
$BaTiO_3$-3	5.67	6.02	94.19
$BaTiO_3$ Av	5.72	6.02	95.50

4.3.1.2 Dielectric Properties

ε_r versus temperature graph of the $BaTiO_3$ ceramic sintered at 1270 °C for 1 h is shown in Figure 46. ε_r versus temperature graph of $BaTiO_3$ ceramic shown in Figure 46 exhibits similar features indicated in Figure 8 projected by Tan et al. [40]. As discussed in Section 2.2, in this experiment the cubic, tetragonal, and orthorhombic phase transitions can be observed by ε_r variation at certain temperatures. At 120 °C

the structure changes from cubic to tetragonal, at 15 °C structure changes from tetragonal to orthorhombic. This structure changes can be spotted in Figure 46 because of its effects on ε_r of the ceramic.

ε_r variations with respect to temperature cannot be tolerated in ceramic capacitor applications because the energy storage capacity changes directly related to the ε_r changes. In $BaTiO_3$ the capacity increases nearly 4 times at 120 °C, which can be fatal for electronic device applications. ε_r changes could be suppressed by doping the ceramic with Nb and Co. The structure change happened at 15 °C have lesser impact on the dielectric properties of $BaTiO_3$ ceramic.

The tanδ value of this $BaTiO_3$ ceramic at room temperature and at 1 kHz frequency is 2%. Similar tanδ values are reported by Lee et al. [70].

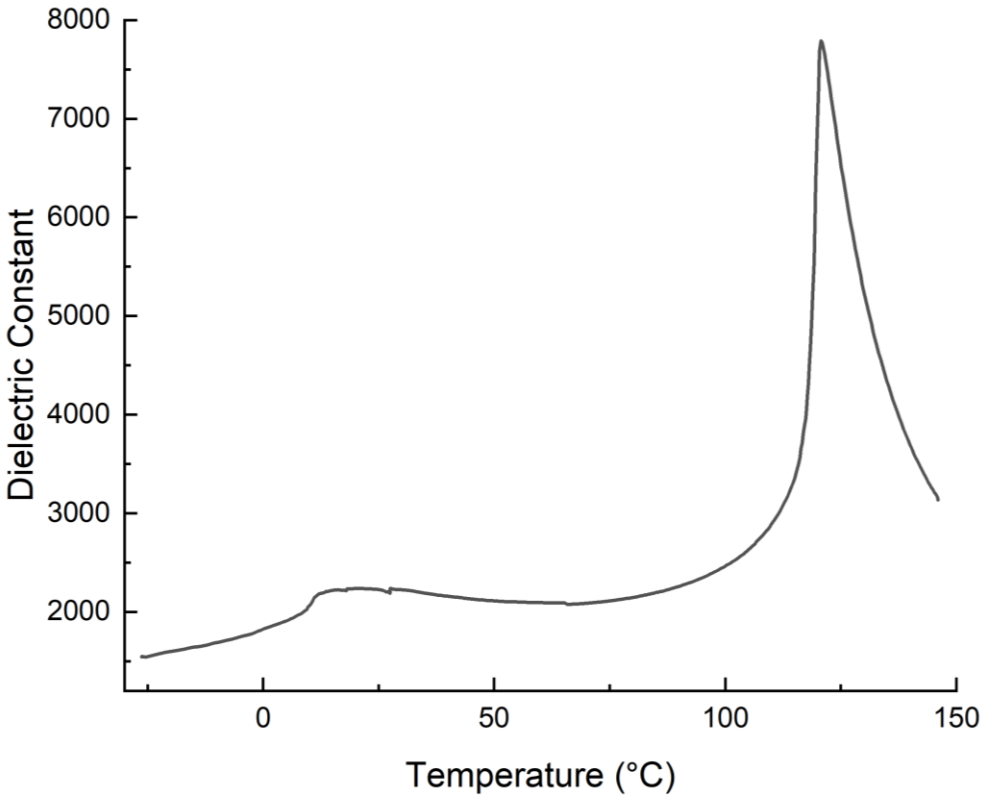

Figure 46. ε_r vs temperature graph of $BaTiO_3$ ceramic sintered at 1270 °C for 1 h.

4.3.1.3 DSC Analysis

Heat flow vs temperature graph of $BaTiO_3$ ceramic sintered at 1270 °C for 1 h is shown in Figure 47. The heat flow of $BaTiO_3$ ceramic changes both at 10 and 120 °C. Since structure transformations cause sudden changes of heat flow in DSC, it could be concluded that the $BaTiO_3$ ceramics undergoes structure transformation at both 10 and 120 °C. Beaten et al. [71] found similar results for 120 °C peak. 10°C peak is observed in the study of Glos et al. [72]. These temperature values overlap with the ε_r change peak values shown in Figure 46. This overlap phenomenon shows that ε_r change occurs because of cubic-tetragonal-orthorhombic structure transformation. The intensity of heat flow changes also correlated with ε_r change. So, the DSC measurements show similar results with dielectric property measurements, and it can be used as an alternative or supplement to dielectric measurement for $BaTiO_3$ based ceramics.

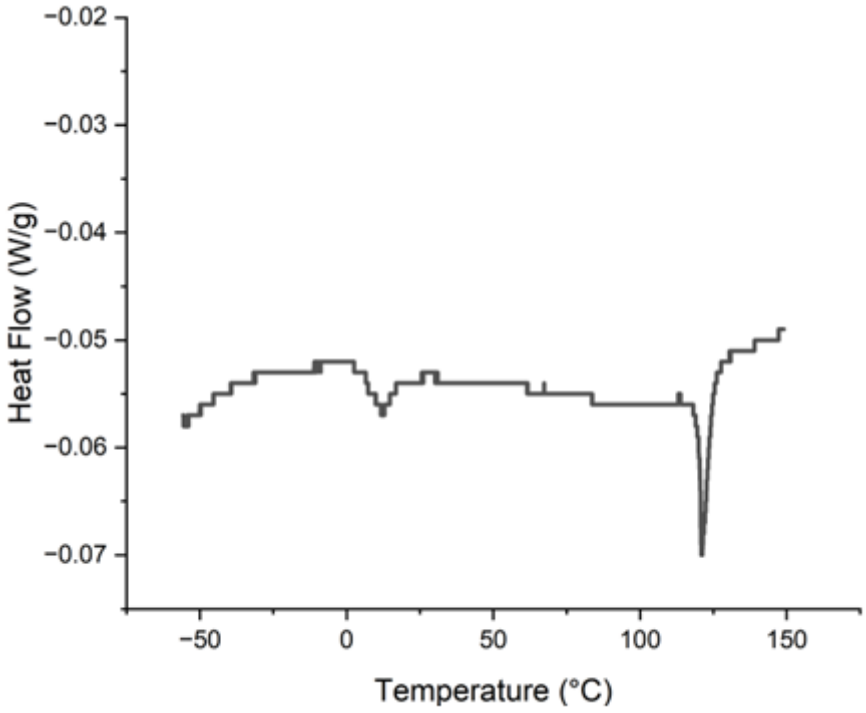

Figure 47. Heat flow vs temperature graph of $BaTiO_3$ ceramic sintered at 1270 °C for 1 h.

4.3.2 Nb Doped $BaTiO_3$ Ceramics

4.3.2.1 Density Measurements

Density of 3 at% Nb doped $BaTiO_3$ ceramics sintered at 1270 °C for 1 h is shown in Table 9. Average relative density is ~91%. The density of sample decreased with respect to $BaTiO_3$ ceramics which could be caused by oxygen vacancies since there is not any acceptor to nullify the effect of Nb doping. Similar density values are reported by Paunovic et al. [73]. By sintering at 1450 °C for 2 h, a relative density of 95% is obtained by Dechakupt et al. [74]. This relative density difference can most probably be attributed to the fact that the temperature activation of sintering is much higher at 1450 °C than at 1270 °C. In the light of abovementioned information, a densification of ~91% was considered unsatisfactory in this study. It is obvious that sintering at 1270 °C for 1 h gives unsatisfactory densification for Nb3 ceramics to be used in capacitor applications.

Table 9. Density data of Nb_2O_5 added $BaTiO_3$ ceramics sintered at 1270 °C for 1 h.

	Experimental Density (g/cm^3)	**Theoretical Density (g/cm^3)**	**Relative Sintered Density (%)**
Nb3-1	5.46	5.99	91.15
Nb3-2	5.44	5.99	90.82
Nb3-3	5.47	5.99	91.32
Nb3-Av	5.46	5.99	91.10

4.3.2.2 Dielectric Properties

ε_r graph of 3 at% Nb doped $BaTiO_3$ is given with respect to the temperature in Figure 48. Nb doping to the $BaTiO_3$ shifts the ε_r peak positions to higher temperatures such as the ε_r peak of $BaTiO_3$ is at 120°C but the Nb doped $BaTiO_3$ has the ε_r peak at 127

°C. Paunovic et al. [73] reported similar temperature dependency of ε_r but with higher ε_r values. The difference between the studies is in the Nb content and sintering temperature. Increasing Nb content decreases the ε_r but increases the temperature stability of ceramics. This is a very desirable outcome since one of the most common capacitor types (X7R) has the temperature dependence condition of ±15% C change between -50 and +125 °C. The Nb doping makes the $BaTiO_3$ C change very stable under varying temperatures, but it has a downside effect which is the drastic decrease in the εr of the ceramic. To be able to produce a high C capacitor, ε_r must be as high as possible.

tanδ value of 3 at% Nb doped $BaTiO_3$ ceramic at room temperature and at 1 kHz frequency is 2.2% which is very similar to pristine $BaTiO_3$. Similar tan δ values are also reported by Paunovic et al [73].

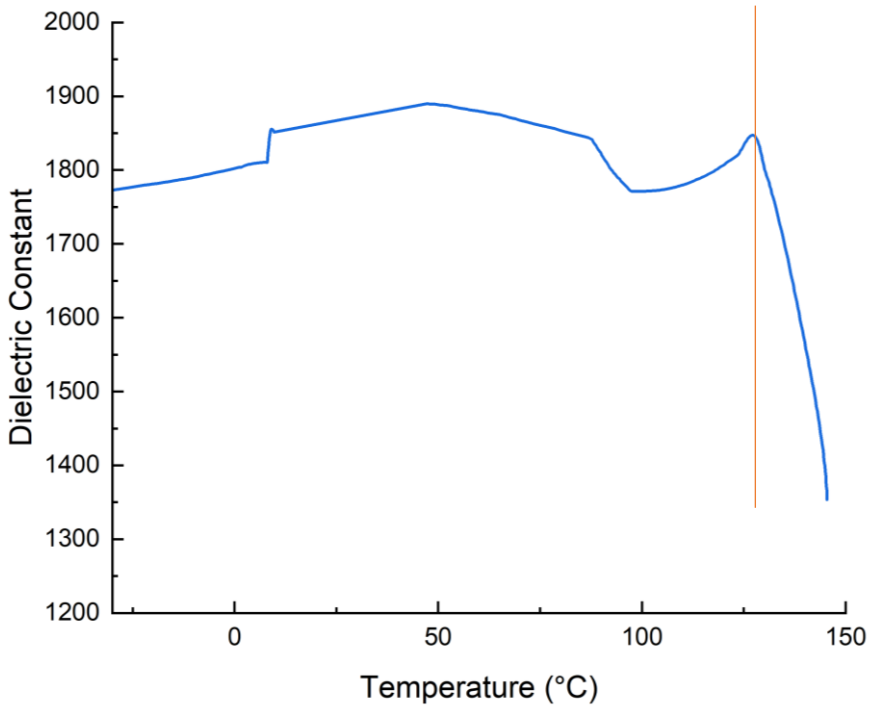

Figure 48. ε_r vs temperature graph of Nb doped $BaTiO_3$ ceramic sintered at 1270 °C for 1 h.

Paunovic et al. [73] stated that substitution-of isovalent impurities in $BaTiO_3$ has a small effect on the electrical conductivity, but off-valent impurities have a large effect on the ferroelectric behavior and conductivity. The main role of the donor cation Nb^{5+} is the effect on grain boundary mobility because charge compensation has a significant effect on dielectric properties. When Nb^{5+} replace Ti^{4+}, the difference in radius and valence of Nb^{5+} and Ti^{4+} leads to a change in the vacancy concentration of the crystal to compensate for the charge imbalance.

4.3.2.3 DSC Analysis

Heat flow vs temperature graph of Nb doped $BaTiO_3$ ceramic shown in Figure 49 shows very little heat flow variation throughout the temperature range of the measurement. This kind of behavior overlaps with the dielectric measurement results shown in Figure 48. The DSC graph also shows that Nb doping to the $BaTiO_3$ inhibits the crystal structure changes as the heat flow is stable throughout the temperature range. DSC measurement of Nb doped $BaTiO_3$ is not present in open literature for comparison.

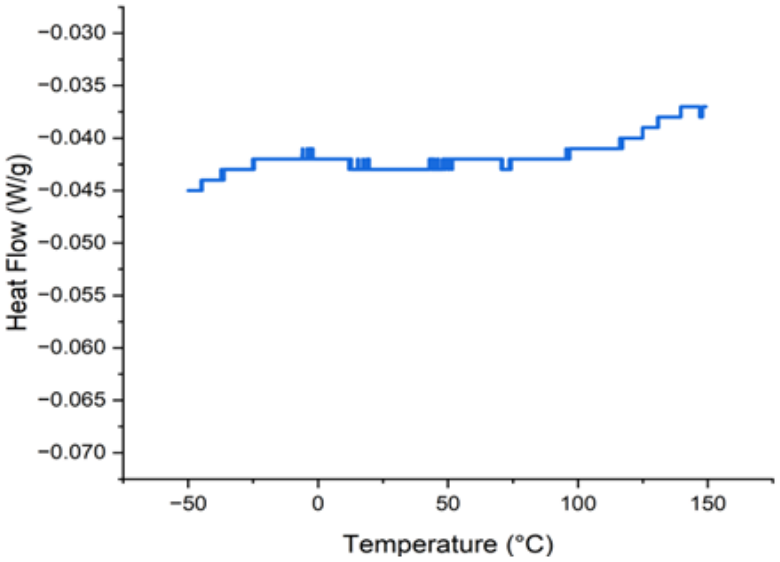

Figure 49. Heat flow vs temperature graph of Nb doped $BaTiO_3$ ceramic sintered at 1270 °C for 1 h.

4.3.3 Co Doped $BaTiO_3$ Ceramics

4.3.3.1 Density Measurements

The density of 3 at% Co doped $BaTiO_3$ ceramics sintered at 1270 °C for 1 h is shown in Table 10. Average relative density of 3 at% Co doped $BaTiO_3$ ceramic is ~91.8%. The density decrease could be caused by oxygen vacancies since there is not any donor to nullify the difference. Osoro et al. [67] reported that a relative density of 96% is obtained by sintering at 1350 °C for 4 h. The difference between the relative densities are most probably due to the differences in sintering temperature and time. It can be concluded that the results are compatible with the present study. In the light of abovementioned information, a densification of ~91.8% was considered unsatisfactory in this study. It is obvious that sintering at 1270 °C for 1 h gives unsatisfactory densification for Co3 ceramics to be used in capacitor applications.

Table 10. Density data of 3 at% Co doped $BaTiO_3$ ceramics sintered at 1270 °C for 1 h.

	Experimental Density (g/cm^3)	**Theoretical Density (g/cm^3)**	**Relative Sintered Density (%)**
Co3-1	5.52	6.03	91.50
Co3-2	5.54	6.03	91.84
Co3-3	5.54	6.03	91.95
Co3-Av	5.53	6.03	91.76

4.3.3.2 Dielectric Properties

ε_r vs temperature graph of Co doped $BaTiO_3$ ceramic is shown in Figure 50. The graph shows that Co doping to the $BaTiO_3$ reduces the intensity of the peak at ~125 °C. The peak is shorter but wider. Even though this behavior is desirable, it is not enough for commercial use because the ε_r is increasing nearly 80% between room

temperature and 125 °C. Similar results between 50 and 125 °C have been reported by Mishra and Mishra [75]. The ε_r is higher than the 3 at% Nb doped $BaTiO_3$ ceramic, but the temperature dependence of ε_r is also higher. So, the combination of Nb and Co should be tried to get both better ε_r and lower temperature dependence throughout the required temperature range.

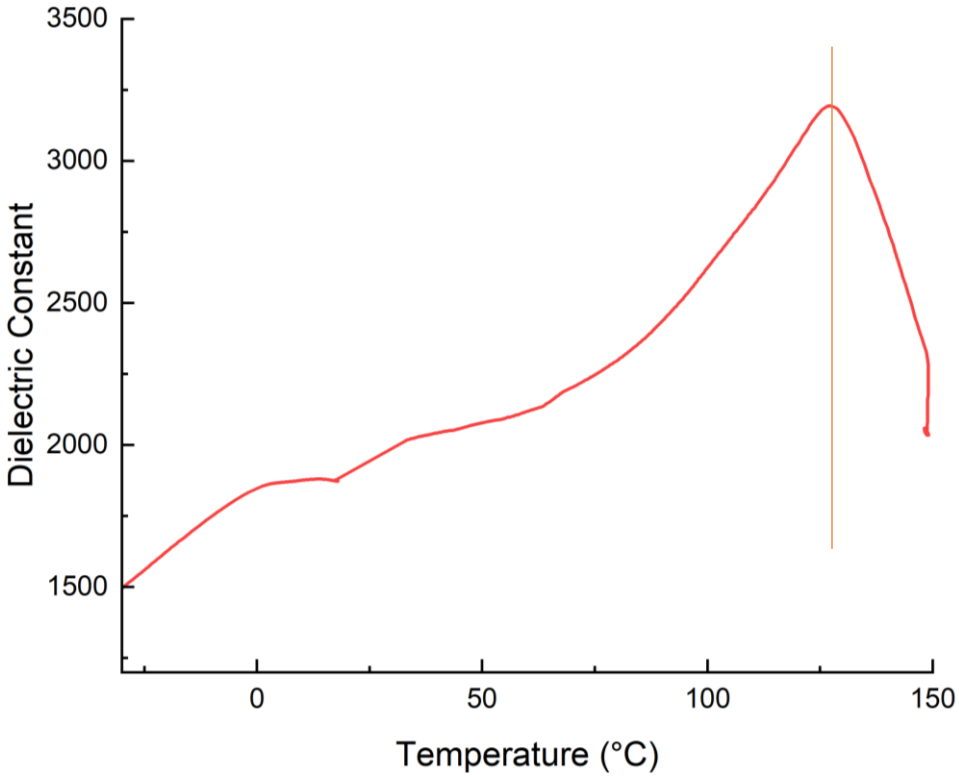

Figure 50. ε_r vs temperature graph of 3 at% Co doped $BaTiO_3$ ceramic sintered at 1270 °C for 1 h.

4.3.3.3 DSC Analysis

Heat flow vs temperature graph of 3 at% Co doped $BaTiO_3$ ceramic is shown in Figure 51. DSC measurement shows that the heat flow decrease starts from 40 °C and continues to 110 °C and after that it starts to increase again. This behavior also overlaps with the ε_r measurement graph of 3 at% Co doped $BaTiO_3$ ceramic shown in Figure 50. The graph also shows that the Co doping $BaTiO_3$ inhibits the crystal structure changes as the heat flow is relatively stable throughout the temperature

range. DSC measurements of Co doped $BaTiO_3$ is not present in open literature for comparison.

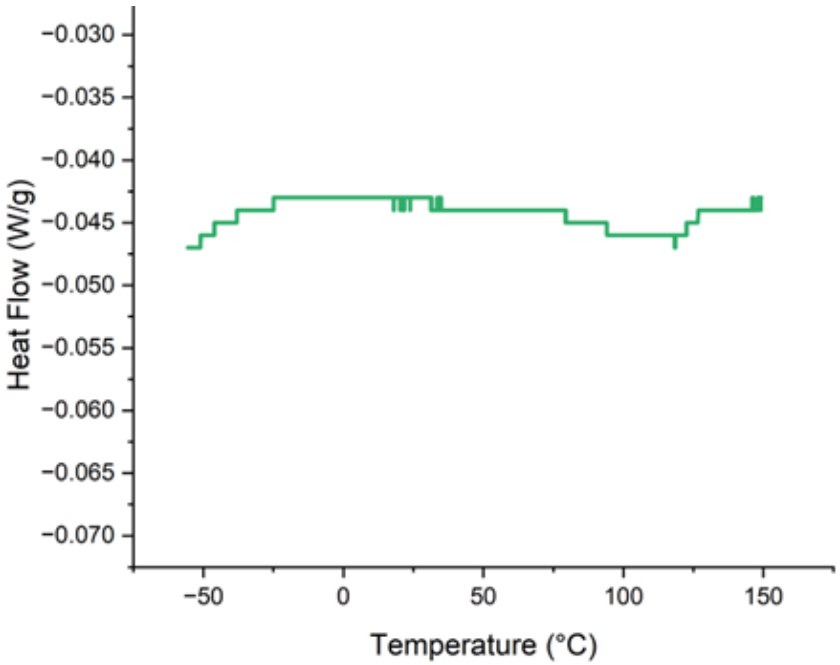

Figure 51. Heat flow vs temperature graph of 3 at% Co doped $BaTiO_3$ ceramic.

4.3.4 Nb-Co Co-Doped $BaTiO_3$ Ceramics

4.3.4.1 Density Measurements

Table 11 shows the density of Nb-Co co-doped $BaTiO_3$ ceramics sintered at 1270 °C for 1 h. Average relative density for Nb3Co1 ceramic is 94.4% and average relative density for Nb1Co1 ceramic is 95.1%. Results show that the increasing Co content increases the relative density of Nb-Co co-doped $BaTiO_3$ ceramics. Similar relative density measurements have been reported by Fernandez et al. [76]. In the light of abovementioned information, a densification of ~94.4% and 95.1% was considered satisfactory in this study. It is obvious that sintering at 1270 °C for 1 h gives satisfactory densification for Nb1Co1 and Nb3Co1 ceramics to be used in capacitor applications.

Table 11. Density data of Nb3Co1 and Nb1Co1 ceramics sintered at 1270 °C for 1 h.

	Experimental Density (g/cm^3)	**Theoretical Density (g/cm^3)**	**Relative Sintered Density (%)**
Nb3Co1-1	5.66	6.00	94.30
Nb3Co1-2	5.68	6.00	94.61
Nb3Co1-3	5.66	6.00	94.27
Nb3Co1-Av	5.67	6.00	94.39
Nb1Co1-1	5.74	6.01	95.58
Nb1Co1-2	5.67	6.01	94.31
Nb1Co1-3	5.73	6.01	95.40
Nb1Co1-Av	5.71	6.01	95.10

4.3.4.2 Dielectric Properties

Dielectric measurements of Nb1Co1 and Nb3Co1 ceramics are shown in Figure 52. Dielectric measurements show that the Nb3Co1 ceramic has an ε_r value ~1.5 times of Nb1Co1 ceramic at room temperature. For a capacitor component, the ε_r is directly related to the energy storage capacity. Higher ε_r is favorable for this application. So Nb3Co1 ceramic potentially has higher application performance at room temperature. Also, the variation of ε_r of Nb3Co1 ceramic can be maintained within ~±15% throughout the temperatures between -30 and +125 °C, which is a boundary for commercially used Y7R type capacitors. On the other hand, the ε_r of Nb1Co1 ceramic could be maintained up to higher temperatures but when the temperature is going down the ε_r decreases constantly which is an undesirable result for an application. The importance of Nb/Co ratio is reported by Chen et al. [9]. Most probably, the complex perovskite $Ba(Co_{1/3}Nb_{2/3})O_3$, reported by Galasso [77] strongly modifies the Curie point of $BaTiO_3$. Hence, the Co_3O_4 additive not only

regulates diffusion and incorporation of Nb_2O_5 but also decisively influences the temperature characteristic of the dielectric material.

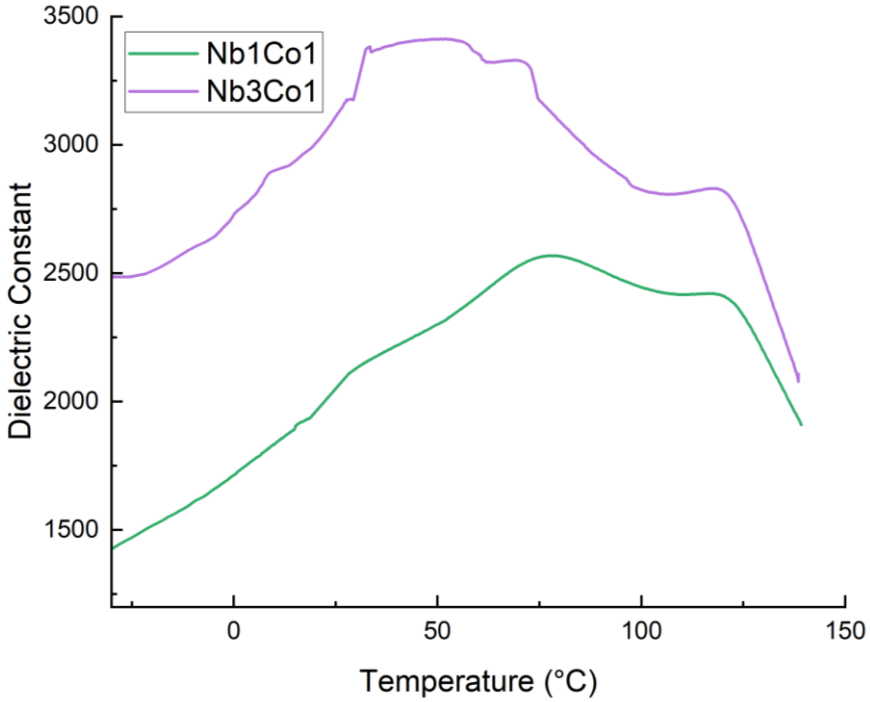

Figure 52. ε_r vs temperature graph of Nb1Co1 and Nb3Co1 ceramics sintered at 1270 °C for 1 h.

4.3.4.3 DSC Analysis

Heat flow vs temperature graph shows that Nb3Co1 ceramics have slightly higher heat flow compared to Nb1Co1 ceramics throughout the temperature range, but the heat flow is more stable as seen in Figure 53. This behavior overlaps with ε_r vs temperature graph shown in Figure 52. Both ceramics show that the doping of Nb and Co into the $BaTiO_3$ structure suppress the structure change in $BaTiO_3$ that otherwise can be detected by DSC measurements. DSC data for Nb-Co co-doped $BaTiO_3$ ceramics are not available in open literature for direct comparison.

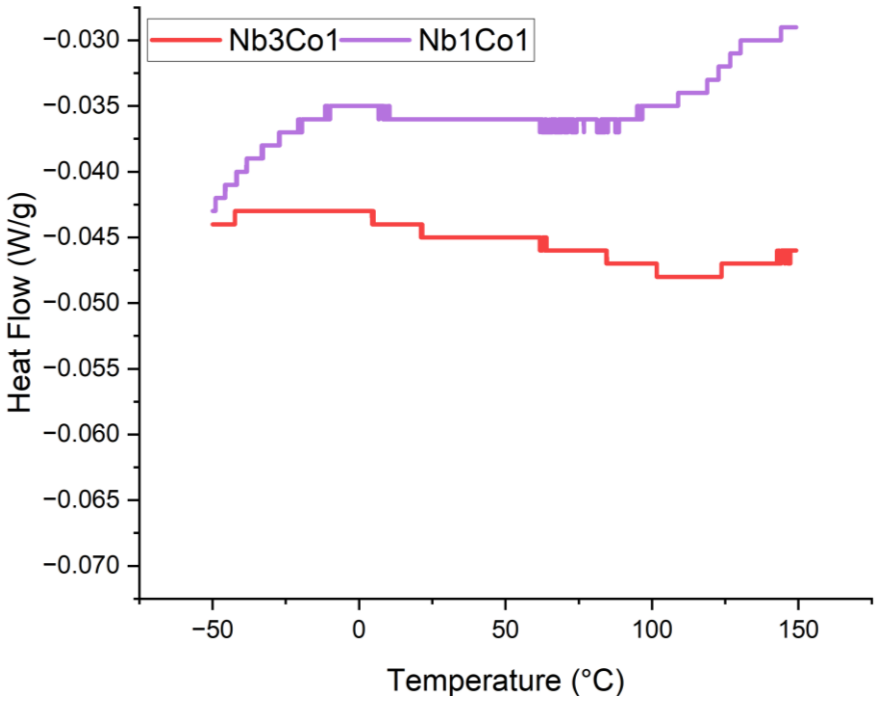

Figure 53. Heat flow vs temperature graph of Nb1Co1 and Nb3Co1 ceramics sintered at 1270 °C for 1 h.

4.4 Comparison of Dielectric Properties

The combined ε_r versus temperature graph of all the studied ceramics in this experimental set is shown in Figure 54. Doping effect on the peak that is observed at ~120 °C in $BaTiO_3$ ceramic is clearly recognized in Figure 54. All the compositions stabilize the ε_r to some extent. The most stable ceramic in this study is Nb3. But its ε_r value is the lowest among all the ceramics. The highest performance ceramic is Nb3Co1 co-doped $BaTiO_3$ ceramic. It has the highest ε_r throughout the measurement range and its ε_r variation in this temperature range is acceptable for Y7R type of capacitors which has ±15% C change throughout the temperature range of -30 to +125 °C.

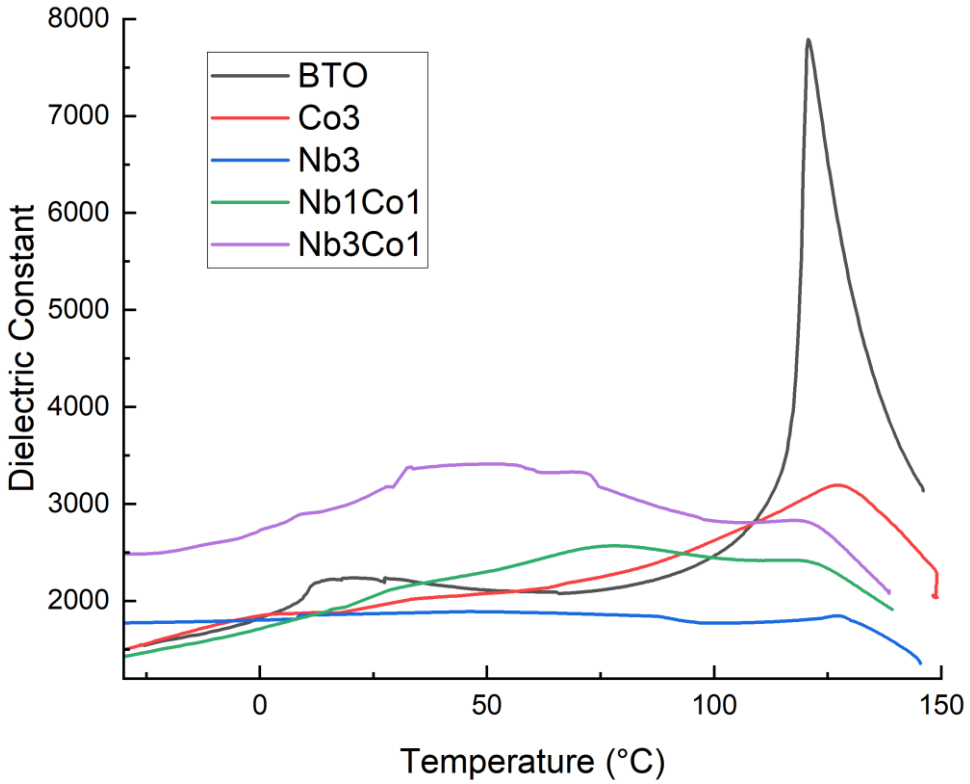

Figure 54. ε_r vs temperature graph of different compositional ceramics sintered at 1270 °C for 1 h.

4.5 Tetragonality effect on Dielectric properties

Tetragonality of the samples are given in Table 12. Tetragonality results shows that if the structure is closer to the cubic (c/a = 1) the temperature dependence decreases accordingly. Doping of the $BaTiO_3$ with Nb and Co decreases tetragonality [78]. The measurements shows that the pristine $BaTiO_3$ ceramics have the highest tetragonality in the study, which has the highest temperature dependence amongst the samples. Nb3, Nb3Col, and Nb1Co1 samples have c/a ratio of 1 which means Nb doping to the $BaTiO_3$ favors the cubic stabilization in room temperature. Cubic structure of samples could be the reason of low temperature dependency of ε_r. Co-doping of the $BaTiO_3$ with Nb and Co favors the cubic structure at room temperature as shown in Table 12.

Tetragonality peaks of the samples shown in Figure 55. Separation of (2 0 0) and (0 0 2) peaks is seen in $BaTiO_3$ ceramic. On the other hand, doped samples other than Co3 sample does not show any peak separation. Suppression of the peak separation could mean that the doping of the $BaTiO_3$ leads to cubic structure at room temperature where it has more temperature stable ε_r compared to tetragonal structure.

Table 12. Tetragonality of different compositional ceramics sintered at 1270 °C for 1 h.

Sample	**a**	**c**	**Tetragonality (c/a)**
$BaTiO_3$	3.9695	4.0058	1.0091
Nb3	3.9747	3.9747	1.0000
Co3	3.9946	3.9489	0.9886
Nb3Co1	4.0288	4.0288	1
Nb1Co1	4.017	4.017	1

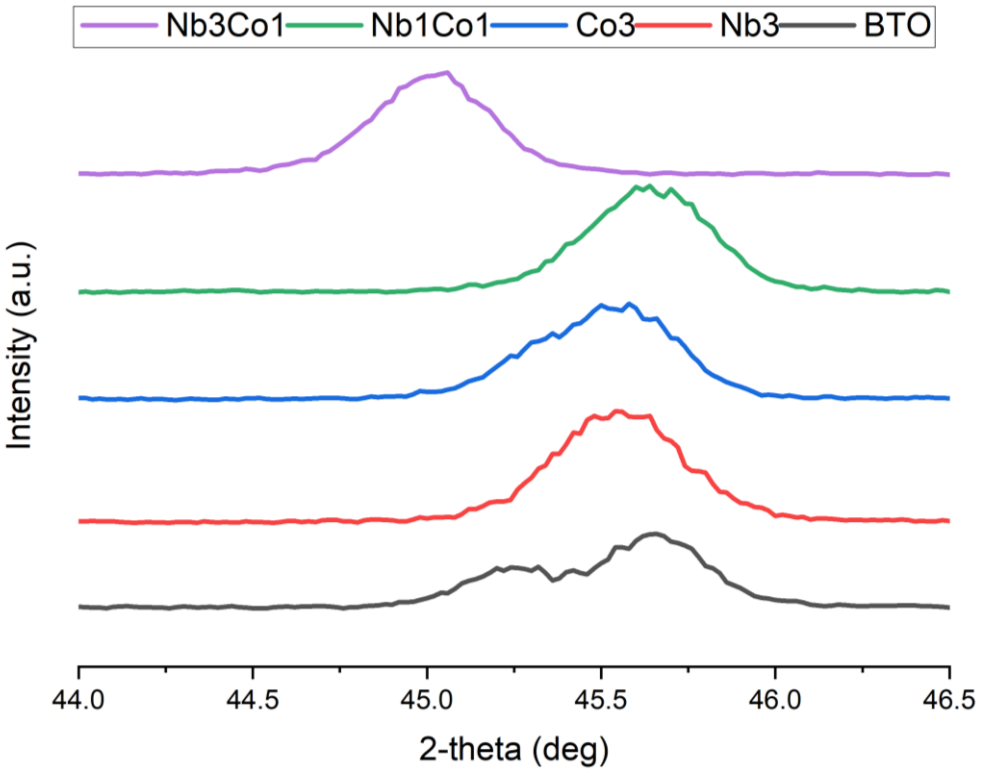

Figure 55. Tetragonality peaks of ceramics.

4.6 Effect of Sintering Temperatures

The effect of sintering temperature on the microstructure, density, and dielectric properties is studied on a selected ceramic composition. The most efficient composition, which is Nb3Co1, is selected to examine the effect of sintering temperature.

4.6.1 Characterization

The microstructures of the Nb3Co1 ceramics sintered at 1250, 1270, and 1290 °C are given in Figure 56. Main difference between these three microstructures is the density of the ceramics. The density of the ceramics are increased by increasing sintering temperature which leads to better pore closure, and smaller and fewer pores. The secondary glassy phase $Ba_6Ti_{17}O_{40}$ is more elongated and pronounced in 1290 °C sintered ceramics. Chazono and Kishi [8] reported that the microstructural development of the high Nb/Co ratio (Nb/Co = 3) ceramic was characterized by the extensive formation of the secondary phase and no growth of matrix grains. It has been reported that the core-shell microstructure forms in a grain in the system $BaTiO_3$ –Nb_2O_5–Co_3O_4 [19], [79] Solution–precipitation has been proposed for the formation mechanism of the core-shell microstructure in the bismuth (Bi) doped $BaTiO_3$ system [80]. Therefore, it was important to investigate whether the secondary phase observed in our system formed a liquid phase. Burn [7] reported that the densification was promoted by the presence of a liquid phase and that the addition of Co, Mg, Ni, and Mn oxides hindered the densification of the $BaTiO_3$ - Nb_2O_5 system. He concluded that such hindrance was caused either by the formation of a refractory compound, such as Nb_2O_6, or by the lack of a liquid phase because of enhanced substitution of Nb.

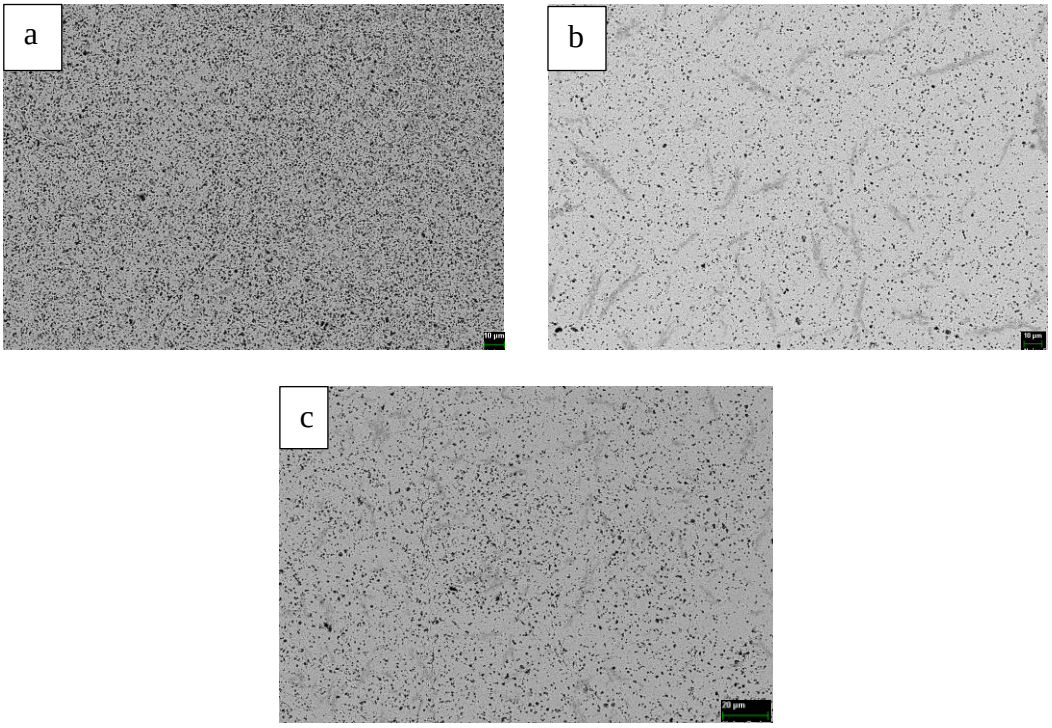

Figure 56. SEM images of sintered microstructures of Nb3Co1 ceramics for 1 h. at (a) 1250 °C (b) 1270 °C (c) 1290 °C.

4.6.2 Density Measurements

Table 13 shows the density measurements of Nb3Co1 ceramics sintered at different temperatures. 1250 °C sintered ceramics have the lowest relative density with the average of ~87.3%. 1290 °C sintered ceramics have the highest relative density with the average of ~96.2%. The difference in relative densities shows that the higher sintering temperature provides higher relative density. Increase of relative density becomes smaller after 1270 °C because densification mechanism slows down exponentially. Sintered density characteristics are reported by Chazono and Kishi [8] by using dilatometry measurements. Similar composition to Nb3Co1 ceramic is presented in that study and the shrinkage behavior is found to be one-step and maximum densification rate is observed at 1250 °C and shrinkage gradually continued to 1450 °C. Similarly, comparison of our results with those of Chazono

for 3 Nb/Co ratio show that the densification is rapidly increased until 1270 °C and then gradually slowed down until 1290 °C.

Table 13. Density data of Nb3Co1 ceramics sintered at 1250, 1270, and 1290 °C for 1 h.

	Experimental Density (g/cm^3)	**Theoretical Density (g/cm^3)**	**Relative Sintered Density (%)**
Nb3Co1-1250-1	5.25	6.00	87.50
Nb3Co1-1250-2	5.23	6.00	87.17
Nb3Co1-1250-3	5.23	6.00	87.17
Nb3Co1-1250-Av	5.24	6.00	87.28
Nb3Co1-1270-1	5.66	6.00	94.30
Nb3Co1-1270-2	5.68	6.00	94.61
Nb3Co1-1270-3	5.66	6.00	94.27
Nb3Co1-1270-Av	5.67	6.00	94.39
Nb3Co1-1290-1	5.78	6.00	96.33
Nb3Co1-1290-2	5.77	6.00	96.18
Nb3Co1-1290-3	5.77	6.00	96.17
Nb3Co1-1290-Av	5.77	6.00	96.23

4.6.3 Dielectric Measurements

The ε_r variation through the temperature range of -30 to +125 °C is shown in Figure 57. ε_r at room temperature gradually increases with increasing sintering temperature. 1250 °C sintered ceramic has the smallest ε_r through the measurement temperature range which shows that the densification of the ceramic is not enough to have desirable performance. 1290 °C sintered ceramic has the highest ε_r value at elevated temperatures but at lower temperatures the ε_r shows a gradual decrease. The reason of the ε_r decrease at lower temperatures might be due to the vaporization of Co at higher sintering temperatures. Chazono and Kishi [8] reported that the vaporization

of Co starts after 1260 °C and gradually increases with further increasing temperature. ε_r decrease is an undesirable property since the change in charge storage capacity becomes larger. Similar ε_r versus temperature graphs are reported by various studies [7]–[9], [19], [76].

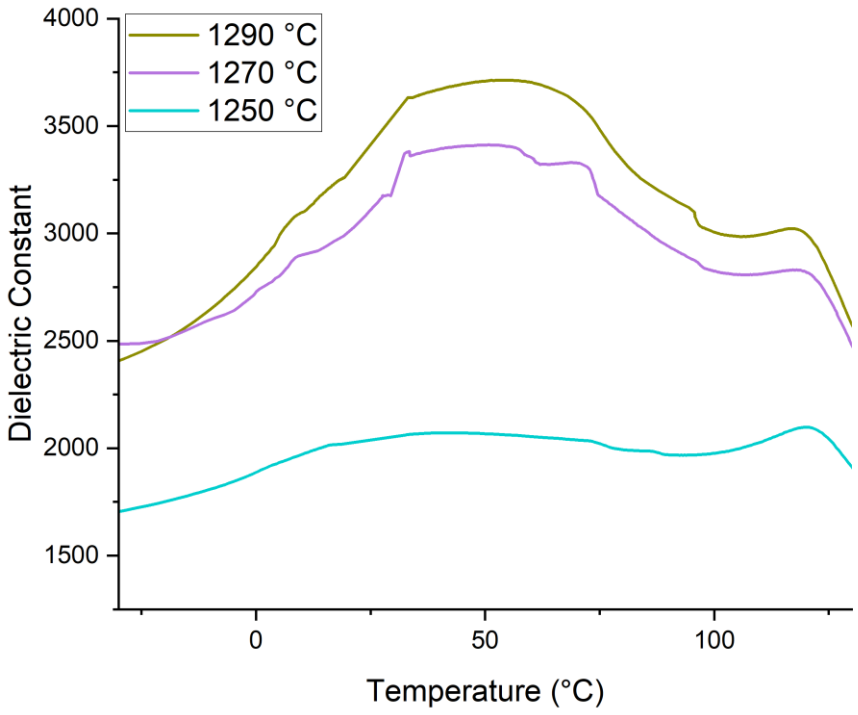

Figure 57. ε_r vs temperature graph of Nb3Co1ceramics sintered at 1250, 1270, and 1290 °C.

Table 14 shows the ε_r data in the temperature range from -30 to +125 °C. The most consistent ceramic is 1250 °C sintered ceramic but, its ε_r is 33% lower than ceramics sintered at 1270 and 1290 °C, at room temperature. Since the most common usage of capacitors is at or around room temperature, higher ε_r ceramic should be preferred.

Table 14. ε_r change of Nb3Co1 ceramic within the -30 to +125 °C temperature range for different sintering temperatures

Property	**Sintering Temperature (°C)**		
	1250	**1270**	**1290**
max ε_r	2098	3355	3714
min ε_r	1711	2486	2177
ε_r at Room Temperature	2015	2950	3258
+% ε_r change	4.12	13.73	13.97
-% ε_r change	-15.08	-15.73	-33.18
Tanδ (1 kHz) (%)	1.8	2.7	4.1

The ε_r characteristics of 1270 and 1290 °C sintered ceramics are relatively closer. But the 1270 °C sintered ceramic comes forward again because the ε_r difference at room temperature is 10% for this ceramic but 1290 °C sintered ceramic could not keep this difference throughout the temperature range. Also, the tanδ value of the 1290 °C sintered ceramic is ~50% higher than the 1270 °C sintered ceramic. Value of tanδ in capacitor ceramics should be as low as possible. When these two facts are considered together, the 1270 °C sintering temperature is preferable amongst these three temperatures.

4.7 Effect of Sintering Time

The effect of different sintering times on the microstructure, density, and dielectric properties of selected ceramics is examined. The most efficient composition, which is Nb3Co1, and the most efficient sintering temperature which is 1270 °C is selected to observe the effect of sintering times (30, 60, and 120 min).

4.7.1 Characterization

The effect of sintering time difference is seen in Figure 58 which shows the SEM images of sintered microstructures for different sintering times. The bowtie-like features in the microstructure were caused by the metallographic etching process. The etchant used to reveal the microstructure of $BaTiO_3$ based ceramics includes HF. These bowtie-like features are mostly containing F and probably hydrogen, but SEM and EDS methods are not sufficient for this measurement.

The main difference among the microstructures again comes from the densification process. The difference between 30 min and other sintering times is more pronounced than the difference between 60 min and 120 min. The pore sizes got smaller with increasing sintering times. The average pore size is between 2-3 μm for 30 min sintering while it is 1-2 μm for 60, and 120 min sintering, respectively.

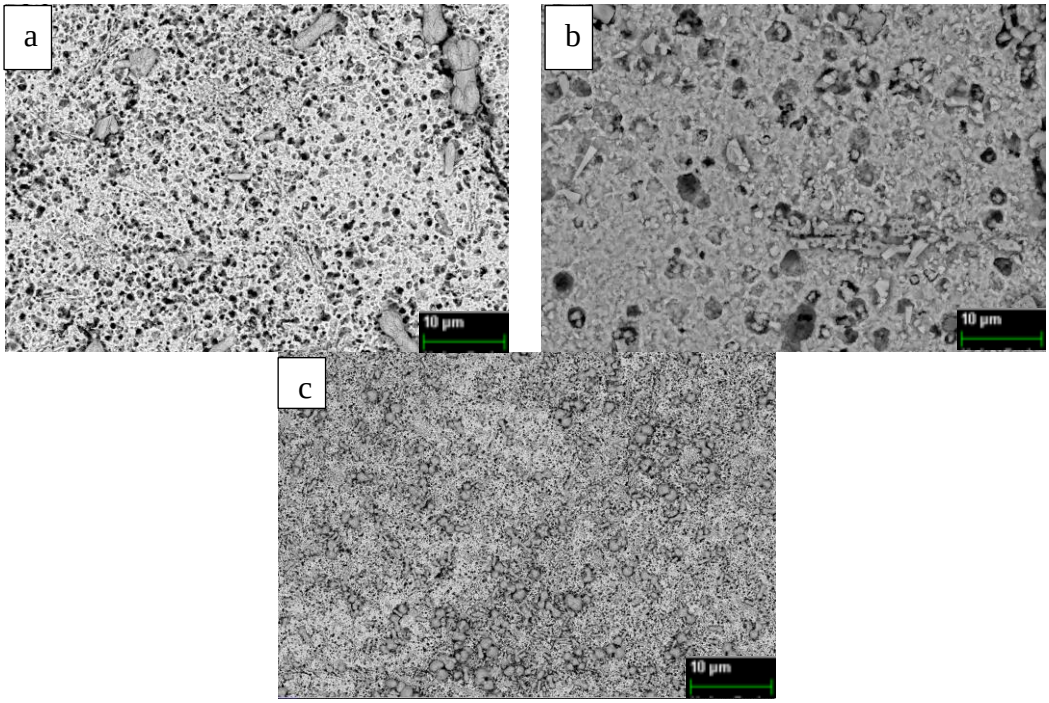

Figure 58. SEM images of sintered microstructures of Nb3Co1 ceramics at 1270 °C. for (a) 30 min, (b) 60 min, (c) 120 min.

4.7.2 Density Measurements

The density data of Nb3Co1 ceramics sintered at 1270 °C for different sintering durations are shown in Table 15. 30 min sintered ceramics have the lowest relative density with the average of 91%. 120 min sintered ceramics have the highest relative density with the average of 95.2%. The difference in relative densities shows that the longer sintering time provides higher relative density. But, the densification slows down gradually after 1270 °C.

Table 15. Density data of Nb3Co1 ceramics sintered at 1270 °C for different sintering durations.

	Experimental Density (g/cm^3)	**Theoretical Density (g/cm^3)**	**Relative Sintered Density (%)**
Nb3Co1-30 min-1	5.45	6.00	90.83
Nb3Co1-30 min-2	5.48	6.00	91.33
Nb3Co1-30 min-3	5.46	6.00	91.00
Nb3Co1-30 min-Av	5.46	6.00	91.05
Nb3Co1-60 min-1	5.66	6.00	94.30
Nb3Co1-60 min-2	5.68	6.00	94.61
Nb3Co1-60 min-3	5.66	6.00	94.27
Nb3Co1-60 min-Av	5.67	6.00	94.39
Nb3Co1-120 min-1	5.70	6.00	95.00
Nb3Co1-120 min-2	5.71	6.00	95.17
Nb3Co1-120 min-3	5.72	6.00	95.33
Nb3Co1-120 min-Av	5.71	6.00	95.17

4.7.3 Dielectric Measurements

The variation of ε_r throughout -30 to +125 °C temperature range is shown in Figure 59. The ε_r value at room temperature is lowest for 30 min sintered ceramic amongst the three ceramics. The main reason for this result is that densification is not completed enough to provide sufficient ε_r. On the other hand, ε_r of 60 min and 120 min sintered ceramics are quite close. Also, the shape of the graph through the temperature range looks similar for both ceramics. This could mean densification process slows down after 60 min.

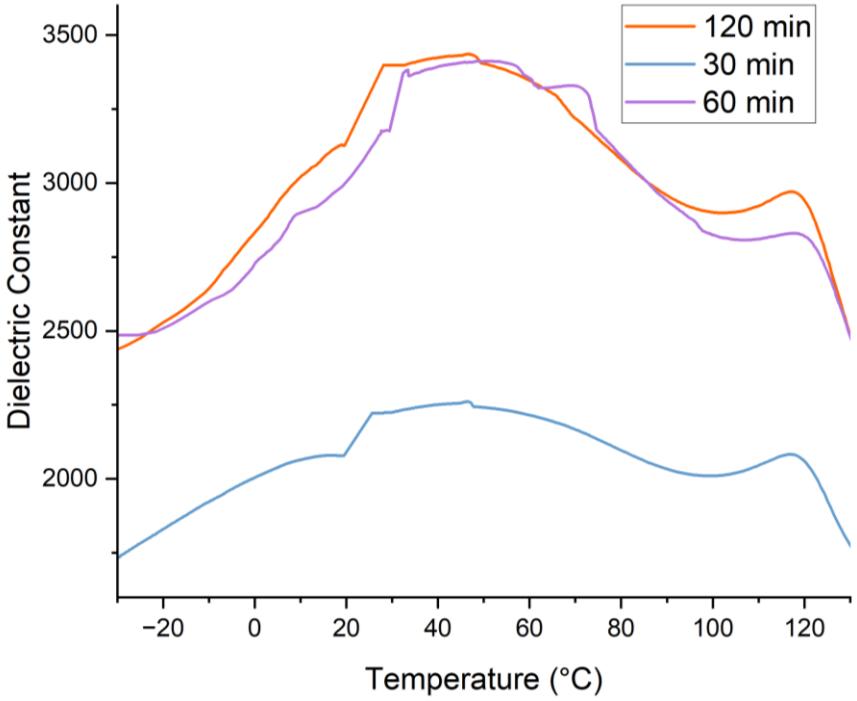

Figure 59. ε_r vs temperature graph of Nb3Co1ceramics sintered at 1270 °C for different sintering times.

The ε_r change of different sintering time ceramics is seen in Table 16. Although the highest ε_r ceramic is 120 min sintered ceramic, negative ε_r change of this ceramic is 33% higher than 60 min sintered ceramic. Also, the tanδ value of 120 min ceramic is again higher than the 60 min ceramic. Higher tanδ value implies that 120 min sintered ceramic is less efficient than 60 min sintered ceramic.

Table 16. ε_r change of Nb3Co1 ceramic within the -30 to +125 °C temperature range, which is sintered at 1270 °C for different sintering times

Property	**Sintering Time (min)**		
	30	**60**	**120**
max ε_r	2261	3355	3435
min ε_r	1699	2486	2477
ε_r at Room Temperature	2090	2950	3126
+% ε_r change	8.21	13.73	9.89
-% ε_r change	-18.66	-15.73	-20.74
tanδ (1 kHz) (%)	2.1	2.7	3.1

CHAPTER 5

CONCLUSIONS

Experimental reasults proved that it is possible to produce Nb-Co co-doped $BaTiO_3$ ceramics with mixed-oxide method. Nb and Co co-doping plays an important role on the development of porosity that is mostly related to sintering temperature in $BaTiO_3$ ceramics. Higher sintering temperatures lead to higher relative density. Results show that controlling Nb/Co ratio could increase the ε_r stability over the temperature range of -30 to +125 °C. ε_r values at room temperature increase by increasing sintering temperature, but the tanδ and temperature dependency of ε_r also increases. Relative density of 94.5%, ε_r variation of ~±15% throughout the temperature range of -30 to +125 °C (which is a boundary for commercially used Y7R type capacitors) and tanδ of 2.7% are obtained for Nb-Co co-doped $BaTiO_3$ ceramics at Nb/Co atomic ratio of 3 when sintered at 1270 °C for 60 min. DSC measurements show that the doping of $BaTiO_3$ suppresses the structural changes in the temperature range from -50 to +125 °C.

The DSC measurements coincide with the ε_r - temperature relation but when the ε_r change is decreased by doping the structure, effectiveness of DSC measurements decreases. The ε_r - temperature relation can still be inferred from the DSC thermogram, but the sensitive change ratio could not be decided.

As a future work detection of core-shell structure by TEM analysis and producing tape casted and stacked MLCC's are planned.

REFERENCES

[1] V. Buscaglia, M. T. Buscaglia, and G. Canu, ‘$BaTiO_3$-Based Ceramics: Fundamentals, Properties and Applications’, 2020.

[2] M. Klee, ‘Concise encyclopedia of advances in materials science and engineering’, *Advanced Materials*, vol. 4, no. 12, pp. 826–827, 1992.

[3] C. A. Randall, R. E. Newnham, and L. E. Cross, ‘History of the First Ferroelectric Oxide, $BaTiO_3$’.

[4] A. Das and P. Kumar, ‘Characterizations of lead free BNT-BT-KNN ceramic synthesized by microwave technique’.

[5] H. Kishi, Y. Mizuno, and H. Chazono, ‘Base-Metal Electrode-Multilayer Ceramic Capacitors: Past, Present and Future Perspectives’, *Jpn J Appl Phys*, vol. 42, no. Part 1, No. 1, pp. 1–15, Jan. 2003, doi: 10.1143/jjap.42.1.

[6] S. Sato, Y. Nakano, A. Sato, and T. Nomura, ‘Mechanism of improvement of resistance degradation in Y-doped $BaTiO_3$ based MLCCs with Ni electrodes under highly accelerated life testing’, *J Eur Ceram Soc*, vol. 19, no. 6, pp. 1061–1065, 1999, doi: https://doi.org/10.1016/S0955-2219(98)00374-4.

[7] I. Burn, ‘Temperature-Stable Barium Titanate Ceramics Containing Niobium Pentoxide’, *ElectroComponent Science and Technology*, vol. 2, no. 4, pp. 241–247, 1976, doi: 10.1155/APEC.2.241.

[8] H. Chazono and H. Kishi, ‘Sintering Characteristics in $BaTiO_3$–Nb_2O_5–Co_3O_4 Ternary System: I, Electrical Properties and Microstructure’, *Journal of the American Ceramic Society*, vol. 82, no. 10, pp. 2689–2697, Oct. 1999, doi: 10.1111/J.1151-2916.1999.TB02143.X.

[9] R. Chen, X. Wang, L. Li, and Z. Gui, ‘Effects of Nb/Co ratio on the dielectric properties of $BaTiO_3$-based X7R ceramics’, *Mater Sci Eng B Solid State Mater Adv Technol*, vol. 99, no. 1–3, pp. 298–301, May 2003, doi: 10.1016/S0921-5107(02)00554-8.

[10] H. Chazono and H. Kishi, ‘Sintering characteristics in the $BaTiO_3$-Nb_2O_5-Co_3O_4 ternary system: II, stability of so-called “core-shell” structure’, *Journal*

of the American Ceramic Society, vol. 83, no. 1, pp. 101–106, 2000, doi: 10.1111/J.1151-2916.2000.TB01155.X.

[11] H. T. Langhammer, R. Böttcher, T. Müller, T. Walther, and S. G. Ebbinghaus, 'Defect properties of cobalt-doped hexagonal barium titanate ceramics', *Journal of Physics Condensed Matter*, vol. 27, no. 29, Jul. 2015, doi: 10.1088/0953-8984/27/29/295901.

[12] L. Padilla-Campos, D. E. Diaz-Droguett, R. Lavín, and S. Fuentes, 'Synthesis and structural analysis of Co-doped $BaTiO_3$', *J Mol Struct*, vol. 1099, pp. 502–509, Nov. 2015, doi: 10.1016/J.MOLSTRUC.2015.07.012.

[13] B. Cui, P. Yu, J. Tian, H. Guo, and Z. Chang, 'Preparation and characterization of niobium-doped barium titanate nanocrystalline powders and ceramics', *Materials Science and Engineering A*, vol. 454–455, pp. 667–672, Apr. 2007, doi: 10.1016/J.MSEA.2006.11.115.

[14] R. Piticescu, P. Vilarinho, L. Madalina, and R. Piticescu, 'Hydrothermal synthesis of perovskite based materials for microelectronic applications', *Journal of Optoelectronics and Advanced Materials*, vol. 8, Jul. 2006.

[15] M. N. Rahaman, 'Sintering of Ceramic: Fundamentals', *Ceramic Processing and Sintering, Second Edition*, pp. 425–468, 2017, Accessed: Jul. 20, 2022. [Online]. Available: https://www.taylorfrancis.com/books/9781482275995

[16] S. O. Nelson, 'Dielectric properties measurement techniques and applications', *Transactions of the American Society of Agricultural Engineers*, vol. 42, no. 2, pp. 523–529, 1999, doi: 10.13031/2013.13385.

[17] D. G. Watters and M. E. Brodwin, 'Automatic Material Characterization at Microwave Frequencies', *IEEE Trans Instrum Meas*, vol. 37, no. 2, pp. 280–284, 1988, doi: 10.1109/19.6067.

[18] K. C. Lawrence, S. O. Nelson, and A. W. Kraszewski, 'Automatic System for Dielectric Properties Measurements from 100 kHz to 1 GHz', *Transactions of the ASAE*, vol. 32, no. 1, pp. 304–0308, Jan. 1989, doi: 10.13031/2013.31001.

[19] D. F. K. Hennings and B. S. Schreinemacher, ‘Temperature-stable dielectric materials in the system $BaTiO_3$-Nb_2O_5-Co_3O_4’, *J Eur Ceram Soc*, vol. 14, no. 5, pp. 463–471, Jan. 1994, doi: 10.1016/0955-2219(94)90085-X.

[20] A. A. Guzhova *et al.*, ‘Improvement of polylactic acid electret properties by addition of fine barium titanate’, *J Electrostat*, vol. 79, pp. 1–6, Feb. 2016, doi: 10.1016/J.ELSTAT.2015.11.002.

[21] F. Baeten, B. Derks, W. Coppens, and E. van Kleef, ‘Barium titanate characterization by differential scanning calorimetry’, *J Eur Ceram Soc*, vol. 26, no. 4–5, pp. 589–592, Jan. 2006, doi: 10.1016/J.Jeurceramsoc.2005.06.029.

[22] A. Behera, ‘Advanced Materials’, 2022, doi: 10.1007/978-3-030-80359-9.

[23] L. McKeen, ‘Film Properties of Plastics and Elastomers’, *Film Properties of Plastics and Elastomers*, 2012, doi: 10.1016/C2011-0-05606-5.

[24] J. William D. Callister and D. G. Rethiwsch, ‘Applications and Processing of Ceramics’, *Materials science and engineering: An introduction*, pp. 460–488, 2010.

[25] R. A. Dorey, ‘Ceramic thick films for MEMS and microdevices’, 2011.

[26] K. Uchino, ‘Relaxor ferroelectric-based ceramics’, *Advanced Piezoelectric Materials: Science and Technology*, pp. 111–129, Jan. 2010, doi: 10.1533/9781845699758.1.111.

[27] S. Musikant, ‘Glass’, *Encyclopedia of Physical Science and Technology*, pp. 781–806, Jan. 2003, doi: 10.1016/B0-12-227410-5/00292-1.

[28] M.-J. Pan and C. A. Randall, ‘A Brief Introduction to Ceramic Capacitors’.

[29] Z. Yao *et al.*, ‘Homogeneous/Inhomogeneous-Structured Dielectrics and their Energy-Storage Performances’, *Advanced Materials*, vol. 29, no. 20, p. 1601727, May 2017, doi: 10.1002/ADMA.201601727.

[30] G. S. Gudavalli and T. P. Dhakal, ‘Simple parallel-plate capacitors to high-energy density future supercapacitors: A materials review’, in *Emerging Materials for Energy Conversion and Storage*, Elsevier, 2018, pp. 247–301. doi: 10.1016/B978-0-12-813794-9.00008-9.

[31] I. Robertson. Sinclair, ‘Passive components for circuit design’, p. 295, 2001.

[32] S. Ono, ‘Passive films for electrolytic capacitors’, *Encyclopedia of Interfacial Chemistry: Surface Science and Electrochemistry*, pp. 376–395, Jan. 2018, doi: 10.1016/B978-0-12-409547-2.13412-2.

[33] ‘Ceramic Capacitors Selection Guide: Types, Features, Applications | Engineering360’. https://www.globalspec.com/learnmore/electrical_electronic_components/electronic_components/ceramic_capacitors (accessed Jul. 20, 2022).

[34] B. Jaffe, W. R. Cook, and H. Jaffe, *Piezoelectric ceramics*. London ; New York: Academic Press, 1971. Accessed: Jul. 19, 2022. [Online]. Available: http://www.sciencedirect.com/science/article/pii/B9780123795502500090

[35] Prateek, V. K. Thakur, and R. K. Gupta, ‘Recent Progress on Ferroelectric Polymer-Based Nanocomposites for High Energy Density Capacitors: Synthesis, Dielectric Properties, and Future Aspects’, *Chem Rev*, vol. 116, no. 7, pp. 4260–4317, Apr. 2016, doi: 10.1021/acs.chemrev.5b00495/asset/ımages/medıum/cr-2015-004954_0053.gıf.

[36] H. P. Rooksby, ‘Compounds of the Structural Type of Calcium Titanate’, *Nature*, vol. 155, no. 3938, p. 484, 1945, doi: 10.1038/155484a0.

[37] H. D. Megaw, ‘Crystal Structure of Barium Titanate’, *Nature 1945 155:3938*, vol. 155, no. 3938, pp. 484–485, 1945, doi: 10.1038/155484b0.

[38] H. F. Kay and P. Vousden, ‘XCV. Symmetry changes in barium titanate at low temperatures and their relation to its ferroelectric properties’, *http://dx.doi.org/10.1080/14786444908561371*, vol. 40, no. 309, pp. 1019–1040, Oct. 2010, doi: 10.1080/14786444908561371.

[39] S. Lee, C. A. Randall, and Z. K. Liu, ‘Modified Phase Diagram for the Barium Oxide–Titanium Dioxide System for the Ferroelectric Barium Titanate’, *Journal of the American Ceramic Society*, vol. 90, no. 8, pp. 2589–2594, Aug. 2007, doi: 10.1111/J.1551-2916.2007.01794.X.

[40] Y. Tan *et al.*, 'Unfolding grain size effects in barium titanate ferroelectric ceramics', *Scientific Reports 2015 5:1*, vol. 5, no. 1, pp. 1–9, May 2015, doi: 10.1038/srep09953.

[41] C. Zhao, Y. Huang, and J. Wu, 'Multifunctional barium titanate ceramics via chemical modification tuning phase structure', *InfoMat*, vol. 2, no. 6, pp. 1163–1190, Nov. 2020, doi: 10.1002/INF2.12147.

[42] Y. Mizuno, Y. Okino, N. Kohzu, H. Chazono, and H. Kishi, 'Influence of the microstructure evolution on electrical properties of multilayer capacitor with Ni electrode', *Japanese Journal of Applied Physics, Part 1: Regular Papers and Short Notes and Review Papers*, vol. 37, no. 9 PART B, pp. 5227–5231, Sep. 1998, doi: 10.1143/JJAP.37.5227/XML.

[43] T. R. Armstrong and R. C. Buchanan, 'Influence of Core-Shell Grains on the Internal Stress State and Permittivity Response of Zirconia-Modified Barium Titanate', *Journal of the American Ceramic Society*, vol. 73, no. 5, pp. 1268–1273, May 1990, doi: 10.1111/J.1151-2916.1990.TB05190.X.

[44] S. C. Jeon, C. S. Lee, and S. J. L. Kang, 'The Mechanism of Core/Shell Structure Formation During Sintering of $BaTiO_3$-Based Ceramics', *Journal of the American Ceramic Society*, vol. 95, no. 8, pp. 2435–2438, Aug. 2012, doi: 10.1111/J.1551-2916.2012.05111.X.

[45] T. R. Armstrong, L. E. Morgens, A. K. Maurice, and R. C. Buchanan, 'Effects of Zirconia on Microstructure and Dielectric Properties of Barium Titanate Ceramics', *Journal of the American Ceramic Society*, vol. 72, no. 4, pp. 605–611, Apr. 1989, doi: 10.1111/J.1151-2916.1989.TB06182.X.

[46] J. S. Kim and S. J. L. Kang, 'Formation of Core-Shell Structure in the $BaTiO_3$-$SrTiO_3$ System', *Journal of the American Ceramic Society*, vol. 82, no. 4, pp. 1085–1088, Apr. 1999, doi: 10.1111/J.1151-2916.1999.TB01882.X.

[47] B. Bradlyn *et al.*, 'Topological quantum chemistry', *Nature 2017 547:7663*, vol. 547, no. 7663, pp. 298–305, Jul. 2017, doi: 10.1038/nature23268.

[48] D. Chaira, ‘Powder Metallurgy Routes for Composite Materials Production’, in *Encyclopedia of Materials: Composites*, Elsevier, 2021, pp. 588–604. doi: 10.1016/b978-0-12-803581-8.11703-5.

[49] H. Goel, K. Saini, K. Razdan, R. K. Khurana, A. A. Elkordy, and K. K. Singh, ‘In vitro physicochemical characterization of nanocarriers: a road to optimization’, *Nanoparticle Therapeutics*, pp. 133–179, Jan. 2022, doi: 10.1016/B978-0-12-820757-4.00018-1.

[50] M. K. Singh and A. Singh, ‘Thermal characterization of materials using differential scanning calorimeter’, *Characterization of Polymers and Fibres*, pp. 201–222, Jan. 2022, doi: 10.1016/B978-0-12-823986-5.00006-3.

[51] P. Gill, T. T. Moghadam, and B. Ranjbar, ‘Differential Scanning Calorimetry Techniques: Applications in Biology and Nanoscience’, *J Biomol Tech*, vol. 21, no. 4, p. 167, Dec. 2010, Accessed: Jul. 20, 2022. [Online]. Available: /pmc/articles/PMC2977967/

[52] J. Abraham, A. P. Mohammed, M. P. A. Kumar, S. C. George, and S. Thomas, ‘Thermoanalytical Techniques of Nanomaterials’, *Characterization of Nanomaterials: Advances and Key Technologies*, pp. 213–236, Jan. 2018, doi: 10.1016/B978-0-08-101973-3.00008-0.

[53] S. Tanaka, ‘Theory of power-compensated DSC’, *Thermochim Acta*, vol. 210, no. C, pp. 67–76, Nov. 1992, doi: 10.1016/0040-6031(92)80277-4.

[54] M. Chiu and E. Prenner, ‘Differential scanning calorimetry: An invaluable tool for a detailed thermodynamic characterization of macromolecules and their interactions’, *J Pharm Bioallied Sci*, vol. 3, no. 1, p. 39, Jan. 2011, doi: 10.4103/0975-7406.76463.

[55] M. T. Jilani, ‘A Brief Review of Measuring Techniques for Characterization of Dielectric Materials’, *International Journal of Information Technology and Electrical Engineering*, Jul. 2012.

[56] M. Biglar, M. Gromada, F. Stachowicz, and T. Trzepieciński, ‘Synthesis of barium titanate piezoelectric ceramics for multilayer actuators (MLAs)’, *Acta*

Mechanica et Automatica, vol. 11, no. 4, pp. 275–279, 2017, doi: 10.1515/AMA-2017-0042.

[57] Z. Lendzion-Bielun, U. Narkiewicz, and W. Arabczyk, 'Cobalt-based catalysts for ammonia decomposition', *Materials*, vol. 6, no. 6, pp. 2400–2409, 2013, doi: 10.3390/MA6062400.

[58] M. Luisa Marin *et al.*, 'Synthesis, acid properties and catalysis by niobium oxide nanostructured materials', *Catal Sci Technol*, vol. 4, no. 9, pp. 3044–3052, Aug. 2014, doi: 10.1039/C4CY00238E.

[59] J. Liu, D. Xue, and K. Li, 'Single-crystalline nanoporous Nb_2O_5 nanotubes', *Nanoscale Res Lett*, vol. 6, no. 1, 2011, doi: 10.1186/1556-276X-6-138.

[60] J. F. Fernández, A. C. Caballero, P. Durán, and C. Moure, 'Improving sintering behaviour of $BaTiO_3$ by small doping additions', *J Mater Sci*, vol. 31, no. 4, pp. 975–981, 1996, doi: 10.1007/BF00352898.

[61] B. R. Li, W. Shang, Z. L. Hu, and N. Q. Zhang, 'Template-free fabrication of pure single-crystalline $BaTiO_3$ nano-wires by molten salt synthesis technique', *Ceram Int*, vol. 40, no. 1 PART A, pp. 73–80, 2014, doi: 10.1016/j.ceramınt.2013.05.105.

[62] B. Cui, P. Yu, J. Tian, H. Guo, and Z. Chang, 'Preparation and characterization of niobium-doped barium titanate nanocrystalline powders and ceramics', *Materials Science and Engineering A*, vol. 454–455, pp. 667–672, Apr. 2007, doi: 10.1016/J.MSEA.2006.11.115.

[63] T. Hoshina, K. Takizawa, J. Li, T. Kasama, H. Kakemoto, and T. Tsurumi, 'Domain size effect on dielectric properties of barium titanate ceramics', *Jpn J Appl Phys*, vol. 47, no. 9 PART 2, pp. 7607–7611, Sep. 2008, doi: 10.1143/JJAP.47.7607/XML.

[64] E. Brzozowski, M. S. Castro, C. R. Foschini, and B. Stojanovic, 'Secondary phases in Nb-doped $BaTiO_3$ ceramics', *Ceram Int*, vol. 28, no. 7, pp. 773–777, 2002, doi: 10.1016/S0272-8842(02)00042-1.

[65] B. Cui, P. Yu, J. Tian, H. Guo, and Z. Chang, 'Preparation and characterization of niobium-doped barium titanate nanocrystalline powders

and ceramics', *Materials Science and Engineering A*, vol. 454–455, pp. 667–672, Apr. 2007, doi: 10.1016/J.MSEA.2006.11.115.

[66] K. G. Baiju *et al.*, 'Hydrothermal synthesis, dielectric properties of barium titanate, cobalt doped barium titanate, and their graphene nanoplatelet composites', *Asia-Pacific Journal of Chemical Engineering*, vol. 15, no. 5, p. e2550, Sep. 2020, doi: 10.1002/APJ.2550.

[67] G. M. Osoro, D. Bregiroux, M. P. Thi, and F. Levassort, 'Structural and piezoelectric properties evolution induced by cobalt doping and cobalt/niobium co-doping in $BaTiO_3$', *Mater Lett*, vol. 166, pp. 259–262, Mar. 2016, doi: 10.1016/j.matlet.2015.12.086.

[68] B. Ertug, B. N. Cetiner, G. Sadullahoglu, H. Gökce, Z. E. Erkmen, and M. L. Ovecoglu, 'The effect of mechanical alloying on the microhardness and fracture toughness of $BaTiO_3$', *Acta Phys Pol A*, vol. 123, no. 2, pp. 188–190, 2013, doi: 10.12693/APHYSPOLA.123.188.

[69] S. Panteny, C. R. Bowen, and R. Stevens, 'Characterisation of barium titanate-silver composites, part I: Microstructure and mechanical properties', *Journal of Materials Science 2006 41:12*, vol. 41, no. 12, pp. 3837–3843, Apr. 2006, doi: 10.1007/S10853-005-5163-X.

[70] K. H. Lee, J. Kao, S. S. Parizi, G. Caruntu, and T. Xu, 'Dielectric properties of barium titanate supramolecular nanocomposites', *Nanoscale*, vol. 6, no. 7, pp. 3526–3531, Mar. 2014, doi: 10.1039/C3NR05535C.

[71] F. Baeten, B. Derks, W. Coppens, and E. van Kleef, 'Barium titanate characterization by differential scanning calorimetry', *J Eur Ceram Soc*, vol. 26, no. 4–5, pp. 589–592, 2006, doi: 10.1016/j.jeurceramsoc.2005.06.029.

[72] B. Garbarz-Glos, R. Bujakiewicz-Korońska, D. Majda, M. Antonova, A. Kalvane, and C. Kuś, 'Differential scanning calorimetry investigation of phase transition in $BaZr_xTi_{1-x}O_3$', *http://dx.doi.org/10.1080/10584580903324592*, vol. 108, no. 1 PART 1, pp. 106–115, 2010, doi: 10.1080/10584580903324592.

[73] V. Paunovic, V. v. Mitic, M. Djordjevic, and Z. Prijic, ‘Niobium doping effect on $BaTiO_3$ structure and dielectric properties’, *Ceram Int*, vol. 46, no. 6, pp. 8154–8164, Apr. 2020, doi: 10.1016/j.ceramınt.2019.12.043.

[74] T. Dechakupt, J. Tangsritrakul, P. Ketsuwan, and R. Yimnirun, ‘Microstructure and Electrical Properties of Niobium Doped Barium Titanate Ceramics’, *http://dx.doi.org/10.1080/00150193.2011.577386*, vol. 415, no. 1, pp. 141–148, 2011, doi: 10.1080/00150193.2011.577386.

[75] A. Mishra and N. Mishra, ‘Effect of doping on structural and dielectric properties of $BaTiO_3$’, *AIP Conf Proc*, vol. 1536, pp. 557–558, 2013, doi: 10.1063/1.4810348.

[76] J. F. Fernandez, P. Duran, and C. Moure, ‘Microstructure and dielectric properties of $BaTiO_3$ doped with niobium and cobalt’, *Ferroelectrics*, vol. 127, no. 1, pp. 53–58, 1992, doi: 10.1080/00150199208223346.

[77] G. H. Jonker, ‘Halogen treatment of barium titanate semiconductors’, *Mater Res Bull*, vol. 2, no. 4, pp. 401–407, Apr. 1967, doi: 10.1016/0025-5408(67)90079-7.

[78] K. Kowalski *et al.*, ‘Electrical properties of Nb-doped $BaTiO_3$’, *Journal of Physics and Chemistry of Solids*, vol. 62, no. 3, pp. 543–551, 2001, doi: 10.1016/S0022-3697(00)00213-4.

[79] H. Chazono and M. Fujimoto, ‘Sintering characteristics and formation mechanisms of core-shell structure in $BaTiO_3$-Nb_2O_5-Co_3O_5 ternary system’, *Jpn J Appl Phys*, vol. 34, no. 9, pp. 5354–5359, 1995, doi: 10.1143/JJAP.34.5354.

[80] D. Hennings and G. Rosenstein, ‘Temperature-Stable Dielectrics Based on Chemically Inhomogeneous $BaTiO_3$’, *Journal of the American Ceramic Society*, vol. 67, no. 4, pp. 249–254, Apr. 1984, doi: 10.1111/J.1151-2916.1984.TB18841.X.